VON KARMAN INSTITUTE FOR FLUID DYNAMICS

LECTURE SERIES 1988-07

UNSTEADY AERODYNAMICS

APRIL 18 - 22, 1988

COMPUTATIONAL UNSTEADY AERODYNAMICS FOR LIFTING SURFACES

John W. Edwards
NASA Langley Research Center, USA

TABLE OF CONTENTS

PART I INTRODUCTION

In the past decade there has been much activity in the development of computational methods for the analysis of unsteady transonic aerodynamics about airfoils and wings. Advances have paralleled developments in steady computational fluid dynamics (CFD) with a lag of approximately five years[1] due to the additional requirement of time-accuracy. Also contributing to this time lag is the sheer number of calculations required to perform flutter analyses, a primary application of unsteady CFD. Figure 1, taken from the specification document for U.S. military aircraft,[2] illustrates significant features which must be addressed in the treatment of computational unsteady transonic aerodynamics. On the plot of equivalent airspeed versus Mach number, lines of constant altitude are straight lines through the origin with decreasing altitudes represented by lines with steeper slopes. An airplane's flight envelope is typically set by the maximum limit speed and a typical flutter boundary curve, characterized by the flutter airspeed gradually dropping to a minimum in the transonic speed range followed by a rapid upward rise. The ability to predict this minimum, termed the transonic flutter dip, is of great importance in design, since the flutter boundary must be shown by a combination of analysis and test to be outside the flight envelope by a margin of at least 15 percent in equivalent airspeed, i.e. the flutter boundary must be outside the dashed line boundary in fig. 1. Subsonic linear unsteady aerodynamic theories have been quite successful in predicting this flutter boundary for Mach numbers up to 0.6-0.7 but linear theory does not account for the effect of aerodynamic shape or maneuvering conditions upon unsteady airloads at transonic speeds. At these Mach numbers linear analysis has been used with more or less success depending upon the severity of local transonic effects. The occurrence of flutter within the flight envelope usually leads to structural failure and loss of the vehicle, highlighting the necessity of careful validation of computational methods intended for use in this area. This is a key difference in the utilization of steady and unsteady computational methods which should be clearly understood.

Transonic Flow Phenomena

It will be helpful to distinguish the main features of steady transonic flow in order to organize the discussion of unsteady aerodynamics. Figure 2, from ref. 3, indicates various regions of transonic flow development for the NLR 7301 airfoil, a 16-percent thick cambered supercritical-type section. With increasing Mach number and moderate angle-of-attack, the upper surface becomes critical between M = 0.4-0.7 with the first shock forming at an

increase of approximately 0.1 in Mach number. Pearcy et al.[4] have classified several types of flow separation which may occur. For conventional airfoils the typical pattern, termed type A, involves the growth of a local separation bubble induced by boundary layer separation at the shock foot, spreading rapidly to the trailing edge as Mach number increases. This condition is often accompanied by unsteady phenomena such as buffet and aileron buzz[3]. The steep aft pressure gradients of modern airfoils, such as the NLR 7301, can lead to an alternate pattern, termed type B, in which separation progresses from the trailing edge towards the shock. Figure 2 illustrates this type B separation, with fully separated flow aft of the shock occuring along the line of maximum lift. Note the small "shock free" design condition occuring over a small isolated range of lift coefficient and Mach number just prior to the onset of trailing edge separation. Tijdeman[3] notes the flow conditons in the region between the onset of trailing edge separation and fully separated flow are very sensitive to Reynolds number and the location of transition from laminar to turbulent flow.

Figure 3 shows a similar diagram, derived from ref. 5, of attached, mixed, and separated flow regions for a complete aircraft at free stream Mach numbers between 0 and 2.0. In region I, the flow is predominantly attached. To obtain optimum performance and to avoid the diag penalty associated with flow separation, design cruise conditions for aircraft typically are located in region I, near the boundary of region II (mixed flow).

As speed and/or angle of attack increase, a transition region of mixed flow (region II of fig. 3) is encountered. For rigid structures, this region is typified by the onset of localized regions of flow separation which may exhibit significant aerodynamic unsteadiness. For realistic flexible structures, the aeroelastic response of the structure interacts with the airflow to induce much more complicated situations. For instance, structural vibrations can cause the flow to alternately separate and reattach at flow conditions where a rigid structure would support attached flow. The associated highly unsteady aerodynamic loading can interact with the structure to cause unusual aeroelastic phenomena which may restrict the vehicle flight envelope.

With further speed and/or angle of attack increases which may be encountered under maneuvering conditions, stable separated flow conditions emerge (region III of fig. 3). Leading-edge vortex flows and shock-induced vortex flows are of this nature. At still higher angles, vortex bursting in the vicinity of the aircraft can cause severe buffeting. Within such regions the flow is highly unsteady and accurate computations will require careful attention to turbulence modeling. -

While predictive methods for attached flows are reasonably well developed, the picket fence in fig. 3 emphasizes the difficulty in predicting aeroelastic phenomena in the mixed and separated flow regions. It also symoblizes novel features that are being encountered in transonic flutter testing. Modern high performance aircraft are capable of maneuvering at transonic speeds, leading to a much enlarged parameter space that must be considered in flutter analysis and testing. Wing/store loading, fuselage interference, angle-of-attack, wing shape and wing sweep all must be considered, and the traditional flutter boundary parameterization of dynamic pressure at flutter versus Mach number may need to be augmented to adequately describe aeroelastic stability boundaries. For instance, flutter tests give some indication that these additional parameters affect the detailed aeroelastic stability condition near the flutter boundary. Thus, the pickets of the fence in fig. 3 represent possible regions of low damping or instability that might be encountered.

Farmer et al.[6] provided early test results documenting the effect of airfoil shape upon flutter boundaries. Figure 4 shows their comparison of flutter boundaries for two structurally and geometrically similar wings of the same planform. The supercritical wing was a reduced stiffness model of the modified TF-8A wing while the conventional wing had a symmetrical section. The two wings had leading-edge sweep angles of 44.5 degrees. Design cruise Mach number was 0.90 for the conventional wing and 0.99 for the supercritical wing. The supercritical wing was shown to have a 25 percent lower minimum flutter dynamic pressure near Mach 1.0 where type II mixed flow would be expected. Current transonic computational methods are beginning to address this important area which will be a key topic for computational aeroelasticity in the future. Other reports of aeroelastic model tests relevant to this area are; single mode flutter of a low aspect ratio wing studied by Erickson[7], supercritical wing flutter tests performed at the NLR[8,9] and torsional buzz of aeroelastic wings tested at the RAE[10].

Figures 5-8 illustrate four types of aeroelastic response which have been encountered and which offer challenges for computational methods. The four cases illustrate problem areas encountered near the boundaries of aircraft flight envelopes, as operating conditions change from high speed, low angle conditions to lower speed, higher angle conditions. The nonclassical aeroelastic response observed on the DAST ARW-2 wing model[11], fig. 5, is a region of high dynamic response at nearly constant Mach number which was encountered at dynamic pressures well below those for which flutter was predicted. The motion is of the limit-amplitude type and the response is believed to be associated with flow separation and reattachment over the

supercritical wing (type II flow).

Figure 6 illustrates wing/store limited amplitude oscillations experienced by modern, high performance aircraft under various loading and maneuvering conditions at transonic Mach numbers. Such oscillations can result in limitations on vehicle performance. The conditions for which this response occurs appear to be near the onset of type II mixed flow. The response typically increases for maneuvering flight conditions.

Dynamic vortex-structure interactions causing wing oscillations have been observed on a bomber type aircraft[12] for high wing sweep conditions during wind-up turn maneuvers, fig. 7. The flow involves the interaction of the wing vortex system with the first wing bending mode and occurs over a wide Mach number range (0.6-0.95) at angles of attack of 7-9 degrees.

At higher angles, interaction of forebody and wing vortex systems with aft vehicle componets results in vortex-induced buffet loads, illustrated in fig. 8. The figure shows the operating conditions for which tail buffet may occur on a high performance fighter. Buffet of horizontal tails can occur at intermediate angles of attack and is a result of the vortex system encountering the horizontal tail lifting surface. As angle of attack increases, the location of vortex bursting moves upstream in the wake. Loss of lift is associated with the burst location reaching the vicinity of the aircraft, and vertical tail surfaces located in such regions can experience severe dynamic loads.

Historical Perspective

This field received an initial impetus in the mid-1970's from three sources: Tijdeman's[3] pioneering experimental work on transonic unsteady pressure measurements, Magnus and Yoshihara's demonstration of key transonic flow features for an airfoil with an oscillating flap[13] and the introduction of an economical transonic finite-difference solution algorithm by Ballhaus and Goorjian[14]. Ballhaus[15] gives a survey of the field from this period. The AGARD Structures and Materials Panel Subcommittee on Aeroelasticity has selected experimental unsteady pressure data sets and defined two- and three-dimensional Standard Aeroelastic Configurations[16,17] to provide reference computational test cases for the development and validation of improved computational methods. The data sets were obtained from rigid models undergoing pitch and control surface oscillations and includes both conventional and supercritical airfoil geometries[18,19,20]. In addition to these data sets, Sandford et al.[21] summarizes a series of unsteady pressure tests made at NASA Langley and Tijdeman[22] presents a much used data set for a fighter wing configuration.

Computational methods have been pursued at a number of differing levels of physical approximation to the flow equations. Magnus and Yoshihara[13,23,24] used an explicit algorithm to solve the Euler (EE) equations. Steger and Bailey[25] reported a significant early application to the problem of aileron buzz using an implicit approximate factorization solution algorithm for the navier-Stokes (NS) equations. Chyu and his coauthors[26,27] have pursued further applications of derivatives of this code. Most of the nonlinear unsteady computations to date have been made by solving the potential equations, both with and without interacted viscous effects. For example, the alternating-direction implicit (ADI) algorithm embodied in the LTRAN2 code of Ballhaus and Goorjian[14] enabled efficient solutions of the two-dimensional flow frequency transonic small disturbance (TSD) potential equation through the use of large time steps. Extensions of this ADI algorithm have been widely used by many researchers. A semi-implicit form of the ADI algorithm is used in the 3-D XTRAN3S code[28,29] developed for the aeroelastic analysis of wings. Other TSD and Full Potential (FP) equation codes are described in refs. 30-35. There is a growing trend, especially for steady flows, towards use of the Euler equations rather than the potential equations. Euler equation codes treating 2-D oscillating airfoils are reported in refs. 36-40 while Salmond[41] and Belk[42] show results from 3-D Euler codes.

Over this same time period, several experimental investigations of periodic aerodynamic flows about rigid airfoils have been reported. McDevitt[43,44] documented such conditons for a very narrow range of Mach number of an 18 percent thick circular arc airfoil and Levy[45] reproduced the effect with calculations from a NS code. Subsequently, Mabey[46] studied these oscillations for circular arc airfoils with thicknesses of 10-20 percent. References 47 and 48 give details for a 14 percent circular arc airfoil. Related information regarding the interaction of unsteady airloads caused by transitional boundary layers with structural oscillations is given by Mabey et al.[49]. Another class of separation-induced periodic flow problems, vortex shedding about rigid cylinders and airfoils at high angle-of-attack, has been studied using NS codes for a variety of Reynolds numbers in refs. 50-52.

Unsteady aerodynamics has been the theme of four recent AGARD conferences[53-56] whose proceedings contain a wealth of information. Survey papers focusing upon computational requirements and resources are given by Peterson[57] and McCroskey et al.[58]. Summary papers of the 1984 and 1985 AGARD conferences are given by Mykytow[59] and by Mabey and

Chambers[60]. The latter reference makes recommendations regarding computational and experimental methods for unsteady flow phenomena and draws particular attention to the need to pay careful attention to the nature of shock motions. The periodic oscillations about circular arc airfoils are recommended as benchmark computational cases for all time-dependent transonic viscous flow theories. Zwaan[61] surveys aeroelastic problems in transonic flow while Deiwert[62] reviews the numerical simulation of unsteady interactive flows. Finally, Mabey[63] gives a review of pertinent experimental research on time-dependent aerodynamics.

Experimental Data Sets

In this section, the airfoil geometries and wing planforms which have been most frequently studied are summarized. In addition to the AGARD standard configurations, several other model tests have been popular for comparison with computational results. Figures 9 and 10 show the profiles and planforms of the 2-D[16] and 3-D[17] AGARD configurations, respectively. Data sets for all of these configurations except the 6 percent parabolic arc, D0 A1 and MBB-A3 airfoils are given in refs. 18, 19, and 64. Tables 1 and 2, from ref. 1, tabulate selected references for these and other configurations in which comparisons of experimental and calculated unsteady pressures are given. The entries are grouped by the equation level of the physical modeling used for the calculations. The references are not exhaustive but are an attempt to indicate publication of significant experimental/computational comparisons or new capability.

The first three airfoils in Table 1 are conventional airfoils with 6, 10, and 12 percent thickness ratios. Tijdeman[3] tested the NACA 64A006 airfoil with an oscillating quarter-chord trailing-edge control surface. Interpretations of these tests[3] have provided insights into the underlying mechanisms of unsteady transonic flows. Tijdeman indentified three types of shock motion, denoted type A, B, and C. In type A shock motion, the shock wave remains distinct during the oscillation cycle, with a periodic variation of shock location and shock strength. In type B shock motion, the shock wave weakens and disappears during a portion of the cycle, generally during the forward propagation of the shock along the surface. For type C motion, the shock wave on the airfoil remains distinct and propagates forward along the airfoil chord and off the airfoil leading-edge.

Davis and Malcolm[65] tested the NACA 64A010A airfoil for pitching oscillations. Two cases from this test have been widely studied: a case with a moderate shock wave at $M = 0.8$ and $\alpha = 0$ degrees and a case with steady shock-induced separation at $M = 0.8$ and $\alpha = 4$ degrees. The NACA

0012 airfoil, tested by Landon[18], differs from the other entries in Table 1 in that it was tested for larger dynamic pitching amplitudes and for transient ramping motions making it suitable for dynamic stall computational studies. McDevitt and Okuno[66] have reported measurements of periodic shock-induced oscillations for this airfoil.

Data sets for the 16 percent thick supercritical NLR 7301 airfoil are given by both Tijdeman and Davis[18] and the shock-free condition for this supercritical airfoil has been a challenging computational case. The 8.9 percent thick MBB A-3 airfoil has been tested by Zimmerman[67] and represents a less severe supercritical airfoil computational case. Other supercritical airfoils tested for oscillatory motions or exhibiting unsteady behavior are: a 12 percent thick airfoil tested for pitching, heaving and flap rotation by den Boer and Houwink[68], the RA16SC1 airfoil tested by ONERA[69], and the cryogenic test of a supercritical SC(2)-0714 airfoil by Hess et al.[70]. Reference 68 reported large dynamic responses of airloads on the supercritical airfoil for both oscillating and static motions at type II flow conditions and introduced the concept of "aerodynamic resonance." Similar periodic shock-induced oscillations are reported for the RA16SC1 airfoil[69].

Tests of rigid circular arc airfoils have been reported by McDevitt et al.[43], McDevitt[44], Mabey[46] and Mabey et al.[47]. References 43 and 44 give details of tests of an 18 percent thick airfoil for Reynolds numbers of 1 million to 17 million, covering laminar to fully developed turbulent flows. The wind tunnel walls were contoured to approximate the inviscid streamlines over the airfoil at M = 0.775. Periodic unsteady airflows were observed over a narrow Mach range whose extent depended upon whether Mach number was increasing or decreasing. For increasing Mach numbers, oscillations occurred for $0.76 < M < 0.78$ while for decreasing Mach number the range was wider, $0.73 < M < 0.78$. The frequency of the oscillations was 188 ±3 Hz (reduced frequency k = 0.48 based upon semi-chord). Mabey[46] studied similar periodic flows for a series of circular arc airfoils ranging in thickness from 10 to 20 percent at Reynolds numbers of 0.4-0.6 million. In ref. 47, further investigations on a larger 14 percent thick biconvex wing at Reynolds numbers of 1-7 million is reported. Two necessary criteria evident from the experimental results for the existence of the periodic unsteady flow are given: thickness/chord ratio greater than 12 percent and local Mach number upstream of the terminal shock wave in the range

$$1.24 < M < 1.40$$

McDevitt[44] identifies the predominant shock motion for the 18 percent thick airfoil as type C

whereas Mabey et al.[47] argue that it is type B motion.

The smaller number of entries in Table 2 reflects the situation regarding 3-D testing in that there are fewer experimental data sets widely available and fewer comparisons of experimental and calculated results have been published. Tijdeman[22] tested a model of the F-5 fighter wing including external tanks and stores. This wing has an aspect ratio of 2.98, a taper ratio of 0.31 and a leading edge sweep of 32 degrees. The relatively thin wing section, a modified NACA 64A004.8, has made this a popular computational case since it is well within the capability of TSD codes. Transonic and low supersonic test conditions are available. Of the AGARD Standard Configuration models shown in fig. 6, the NORA model is the most extensively tested. It is a model of the Mirage F-1 horizontal tail which has been tested in four European wind tunnels[17,18].

The AGARD rectangular wing and the RAE Wing A model have symmetric airfoil sections[17,18,20] whereas the ZKP wing and LANN wing have supercritical airfoil sections[17,19]. Additional models tested for oscillatory pitching are the NASA Rectangular Supercritical Wing (RSW) model[71,72] and the RAE AGARD tailplane model[64]. The former had a 12 percent supercritical airfoil section while the latter had a NACA 64A010A section, the same as one of the AGARD 2-D configurations.

Also included in Table 2 are references to several other published comparisons with experimental data. These cases are of interest since the models were aeroelastic and some comparisons of experimental and computed transonic flutter boundaries (or aeroelastic response) are given. Isogai gives comparisons for a high aspect ratio supercritical transport wing in ref. 34 and for the supercritical wing flutter model of Farmer et al.[6] in ref. 74. Bennett et al.[75] give static aeroelastic comparisons for an aspect ratio 10.3 supercritical wing which was extensively instrumented for unsteady pressure measurements[76]. Finally, Guruswamy and Goorjian[77] present calculations for a rectangular parabolic arc flutter model.

Computational Methods

A variety of fluid dynamic flow models is available to address unsteady aerodynamic computations. The choice of an appropriate method calls for assessment of the difficulty of the aerodynamic problem being addressed. Type I flows, fig. 3, include one of the most important aeroelastic analysis conditions, cruise at high dynamic pressure. Classical linear aeroelastic analysis has been primarily focused upon this condition. The transition from type I to type II

conditions can occur due to aircraft maneuvering with little decrease in dynamic pressure. Thus, aeroelastic response and stability of aircraft operating in type II flows can be quite important although they have only recently been brought within the range of computational methods.

Computational methods available for unsteady aerodynamic computation include; the classical (linear) small disturbance potential equation (CSD), nonlinear potential equation (both Transonic Small Disturbance, TSD, and Full Potential, FP, Euler equations (EE) and Navier-Stokes equations (NS).

Issues which have been central to unsteady CFD have been the choice of implicit versus explicit algorithms, the stability of alternative solution algorithms and the treatment of computational grids. Explicit schemes are simple to code and easily vectorizable but are limited in allowable time step by the stability limit imposed by the signal propagation time over the smallest grid cell. Faced with the requirement of maintaining time-accuracy throughout the entire field for aeroelastic computations, this easily leads to excessive computation times, especially for viscous flow calculations where a very fine mesh near the surface is required to resolve the boundary layer. The alternative implicit solution algorithms thus are favored and attention must be given to their relative stability and accuracy characteristics. Grid generation for unsteady problems in which the body boundary moves, such as for an oscillating control surface or an aeroelastic deformation, raises new issues over those involved in steady flows. To maintain accuracy, the body-conforming grid must be realigned with the body at each time step. Schemes for accomplishing this have been studied as well as the necessity of moving the grid at all. When body motions are small with perturbations mainly normal to the surface, imposing boundary conditions on the mean surface location may be an acceptable approximation. Finally, the nature of unsteady calculations means that the solution is not allowed to achieve a steady-state and thus the dynamic response of numerical calculations on the computational grid is more important. For example, grid cell stretching in the near and far field will affect the computational impedance of the grid for unsteady calculations.

In the following sections the physical flow models will be described in order of decreasing complexity, to be followed by discussions of typical results illustrating progress for the various flow modeling levels. Since the historical trend is for computational methods to mature most rapidly for the simpler flow models, this will lead us naturally from classical linear results back to the Navier-Stokes equations. Along the way, capabilities such as the ability to treat geometric complexity will be discussed.

PART II FLUID DYNAMIC FLOW MODELS

Navier-Stokes Equations

Rumsey and Anderson[78] give the thin-layer approximation to the Reynolds averaged Navier-Stokes equations for two-dimensional flow. In the thin-layer approximation viscous terms are resolved in a layer near the body where viscous terms in ξ, the direction along the body, are neglected and only terms in η, normal to the body are retained. The equations are written in generalized coordinates and conservation form;

$$\frac{\partial}{\partial t}(\hat{Q}) + \frac{\partial}{\partial \xi}(\hat{G}) + \frac{\partial}{\partial \eta}(\hat{H} - \hat{H}_v) = 0 \qquad (1)$$

$$\hat{Q} = \frac{Q}{J} = \frac{1}{J}\begin{bmatrix} \rho \\ \rho u \\ \rho v \\ e \end{bmatrix} \quad ; \quad \hat{G} = \frac{1}{J}\begin{bmatrix} \rho U \\ \rho U u + \xi_x p \\ \rho U v + \xi_y p \\ (e+p)U - \xi_t t \end{bmatrix} \qquad (2)$$

$$\hat{H} = \frac{1}{J}\begin{bmatrix} \rho V \\ \rho V u + \eta_x p \\ \rho V v + \eta_y p \\ (e+p)V - \eta_t p \end{bmatrix} \quad ; \quad \hat{H}_v = \frac{1}{J}\begin{bmatrix} 0 \\ \eta_x \tau_{xx} + \eta_y \tau_{xy} \\ \eta_x \tau_{xy} + \eta_y \tau_{yy} \\ \eta_x b_x + \eta_y b_y \end{bmatrix} \qquad (3)$$

The curvilinear generalized coordinates (ξ, η) correspond to the coordinates parallel and normal to the body surface, respectively and are related to Cartesian coordinates (x, y) via the transformation

$$\xi = (x, y, t), \quad \eta = (x, y, t), \quad \tau = t \tag{4}$$

Note that the transformation is time-dependent, allowing the grid to move to follow body motion and giving rise to grid metric terms such as $\eta_t p$ in eq. (3). The contravariant velocities along the η and ξ coordinate directions are

$$\begin{aligned} U &= \xi_x u + \xi_y v + \xi_t \\ V &= \eta_x u + \eta_y v + \eta_t \end{aligned} \tag{5}$$

while the pressure is

$$p = (\gamma - 1)\left[e - \frac{1}{2}\rho\,(u^2 + v^2)\right] \tag{6}$$

The state vector Q represents the density, momentum and total energy per unit volume. The Jacobean of the transformation is J, defined as;

$$J = \frac{\partial(\xi, \eta)}{\partial(x, y)} \tag{7}$$

The equations are nondimensionalized by the freestream density $\tilde{\rho}_\infty$ and soundspeed $\tilde{a}_\infty$. The shear stress and heat flux terms are defined in tensor notation as;

$$\tau_{x_i x_j} = \frac{M_\infty}{Re_L}\left[\mu\left(\frac{\partial u_i}{\partial x_j} + \frac{\partial u_j}{\partial x_i}\right) + \lambda \frac{\partial u_k}{\partial x_k}\delta_{ij}\right] \tag{8}$$

$$q_{x_i} = -\left[\frac{M_\infty}{Re_L\, Pr\,(\gamma - 1)}\right]\frac{\partial (a^2)}{\partial x_i} \tag{9}$$

$$Re_L = \frac{\tilde{\rho}_\infty \tilde{q}_\infty \tilde{L}}{\tilde{\mu}_\infty} \qquad M_\infty = \frac{\tilde{q}_\infty}{\tilde{a}_\infty} \tag{10}$$

In (3), b_{x_i} is defined as

$$b_{x_i} = u_j \tau_{x_i x_j} - \dot{q}_{x_i} \qquad (11)$$

Stokes hypothesis for bulk viscosity, $\lambda + 2\mu/3 = 0$, and Sutherland's law for molecular viscosity,

$$\mu = \tilde{\mu}/\tilde{\mu}_\infty = (\tilde{T}/\tilde{T}_\infty)^{3/2} [(\tilde{T}_\infty + \tilde{c}) / (\tilde{T} + \tilde{c})] \qquad (12)$$

are used, with $\tilde{T}_\infty$ = freestream temperature = 460° R, and $\tilde{c}$ = Sutherland's constant = 198.6° R.

Boundary conditions are applied explicitly. No slip, adiabatic wall conditions, as well as zero normal pressure gradient conditions are applied on the body

$$u = v = 0 \qquad (13a)$$

$$\frac{\partial p}{\partial \eta} = \frac{\partial (a^2)}{\partial \eta} = 0 \qquad (13b)$$

In the farfield, a quasi-one-dimensional characteristic analysis is used to determine boundary data. For turbulent calculations, turbulence modeling such as the algebraic eddy viscosity model of Baldwin and Lomax[79] is required.

Euler Equations

For sufficiently large Reynolds numbers the major effect of viscosity is confined to a thin viscous boundary layer near the surface of a solid body. As a consequence, the inviscid portion of the flowfield may be solved independently of the boundary layer. The reduced set of equations, termed the Euler equations, are obtained by dropping both the viscous terms and the heat transfer terms from the Navier-Stokes equations. Reference 80 contains details and discusses consequences of these assumptions. Anderson et al.[81] present the three-dimensional Euler equations in generalized coordinates for a moving grid mesh in a form analogous to eqs. (1-7). With the generalized coordinates ξ and ζ prescribed parallel and η normal to the body surface

the equations are

$$\frac{\partial \hat{Q}}{\partial t} + \frac{\partial \hat{F}}{\partial \xi} + \frac{\partial \hat{G}}{\partial \eta} + \frac{\partial \hat{H}}{\partial \zeta} = 0 \qquad (14)$$

where

$$\hat{Q} = \frac{Q}{J} = \frac{1}{J} \begin{bmatrix} \rho \\ \rho u \\ \rho v \\ \rho w \\ e \end{bmatrix}, \quad \hat{F} = \frac{1}{J} \begin{bmatrix} \rho U \\ \rho U u + \xi_x p \\ \rho U v + \xi_y p \\ \rho U w + \xi_z p \\ (e + p)U - \xi_t p \end{bmatrix} \qquad (15)$$

$$\hat{G} = \frac{1}{J} \begin{bmatrix} \rho V \\ \rho V u + \eta_x p \\ \rho V v + \eta_y p \\ \rho V w + \eta_z p \\ (e + p)V - \eta_t p \end{bmatrix}, \quad \hat{H} = \frac{1}{J} \begin{bmatrix} \rho W \\ \rho W u + \zeta_x p \\ \rho W v + \zeta_y p \\ \rho W w + \zeta_z p \\ (e + p)W - \zeta_t p \end{bmatrix} \qquad (16)$$

The pressure p and the contravariant velocities U, V, and W are given by straightforward extensions of eqs. (5) and (6). The grid transformation metric variables are given by;

$$\xi_x = J(y_\eta z_\zeta - z_\eta y_\zeta),\ \eta_x = J(z_\xi y_\zeta - y_\xi z_\zeta),\ \zeta_x = J(y_\xi z_\eta - z_\xi y_\eta)$$

$$\xi_y = J(z_\eta x_\zeta - x_\eta z_\zeta),\ \eta_y = J(x_\xi z_\zeta - z_\xi x_\zeta),\ \zeta_y = J(z_\xi x_\eta - x_\xi z_\eta)$$

$$\xi_z = J(x_\eta y_\zeta - y_\eta x_\zeta),\ \eta_z = J(x_\zeta y_\xi - y_\zeta x_\xi),\ \zeta_z = J(x_\xi y_\eta - y_\xi x_\eta) \qquad (17)$$

$$\xi_t = -x_\tau \xi_x - y_\tau \xi_y - z_\tau \xi_z,\ \eta_t = x_\tau \eta_x - y_\tau \eta_y - z_\tau \eta_z,\ \zeta_t = -x_\tau \zeta_x - y_\tau \zeta_y - z_\tau \zeta_z$$

In ref. 81 the boundary conditions are applied explicitly. On the body, the contravariant

velocity normal to the body is set to zero

$$\bar{V} = V/|\text{grad}\,\eta| = 0 \qquad (18)$$

and pressure, tangenial velocities and density are determined by extrapolation from the interior. In the farfield, a quasi-one-dimensional characteristic analysis is used to determine boundary data.

While the Euler equations do not treat viscous and heat transfer effects, entropy and vorticity effects allow treatment of flows with strong shock waves (which generate entropy) and moderate-to-high angle vortex dominated flows. Even though viscosity is eliminated, no explicit Kutta condition enforcing smooth flow from the trailing edges of lifting surfaces is required since "numerical" viscosity generated by finite difference solutions provides this effect.

Potential Equation

If it is assumed that the flow is irrotational then the velocity field, V, can be shown to be the gradient of a scalar field variable, the velocity potential Φ (see ref. 80 for details)

$$V = \nabla\Phi \qquad (19)$$

The conservation form of the continuity equation for two-dimensional flow becomes (ref. 82)

$$\rho_t + (\rho\Phi_x)_x + (\rho\Phi_z)_z = 0 \qquad (20)$$

For barotropic, isentropic flow the momentum and energy equations yield the compressible Bernoulli equation from which the density ρ is determined.

$$\rho = [1 + \frac{\gamma - 1}{2}(M_\infty^2 - 2\Phi_t - \Phi_x^2 - \Phi_z^2]^{\frac{1}{\gamma-1}} \qquad (21)$$

The spatial coordinates, x and z, are normalized by airfoil chord c, and time t is normalized by a_∞/c. Density and Φ are normalized by ρ_∞ and $a_\infty c$.

Again, solutions are obtained for body fitted generalized coordinates which allow for body and

grid motion. Note that here and in the following small disturbance potential equation, the coordinates x and z are the freestream direction and the direction normal to the lifting surface respectively. The transformation to a body-fitted coordinate system is given by

$$\xi = \xi(x, z, t), \quad \zeta = \zeta(x, z, t), \quad \tau = t \tag{22}$$

The strong conservation form of eq. (20) is maintained by writing the continuity equation as

$$\left(\frac{\rho}{J}\right)_\tau + \left(\frac{\rho U}{J}\right)_\xi + \left(\frac{\rho W}{J}\right)_\zeta = 0 \tag{23}$$

Equation (21) transforms to

$$\rho = \{1 + \frac{\gamma - 1}{2}[M_\infty^2 - 2\Phi_\tau - (U + \xi_t)\Phi_\xi - (W + \zeta_t)\phi_\zeta]\}^{\frac{1}{\gamma-1}} \tag{24}$$

Where the contravariant velocities are

$$\begin{aligned} U &= \xi_t + (\xi_x^2 + \xi_z^2)\Phi_\xi + (\xi_x\zeta_x + \xi_z\zeta_z)\Phi_\zeta \\ W &= \zeta_t + (\xi_x\zeta_x + \xi_z\zeta_z)\Phi_\xi + (\zeta_x^2 + \zeta_z^2)\Phi_z \end{aligned} \tag{25}$$

and $J = \xi_x\zeta_z - \xi_z\zeta_x$. The isentropic pressure coefficient is derived from the compressible Bernoulli equation as

$$C_p = \frac{2}{\gamma M_\infty^2}(\rho^\gamma - 1) \tag{26}$$

The airfoil boundary condition that the flow be tangent to the airfoil is satisfied by requiring W = 0 on the airfoil. For lifting flows, the shed vorticity is represented by a jump in potential across the wake line. For isentropic flows the condition is

$$\Gamma_\tau + \langle W \rangle \Gamma_\zeta = 0 \tag{27}$$

where Γ is the jump in potential across the wake, $\Phi^u - \Phi^l$, and $\langle W \rangle$ is the average of W above and below the wake. In the farfield, the flow is set to freestream conditions

$$\Phi = M_\infty x, \quad \rho = 1 \tag{28}$$

Transonic Small Disturbance Potential Equation

The Transonic Small Disturbance (TSD) Potential equation is derived from the inviscid Euler equations assuming that the flow is a small perturbation of a steady uniform flow, U_∞, in the x direction (see, for instance, ref. 83). The TSD velocity potential function, ϕ, describes the perturbed velocity components u, v, w.

$$u = \frac{\partial \phi}{\partial x}, \qquad v = \frac{\partial \phi}{\partial y}, \qquad w = \frac{\partial \phi}{\partial z} \tag{29}$$

where the total velocity in the x direction is $U_\infty + u$. References 84 and 85 give the modified TSD potential equation in conservation form as

$$\frac{\partial f_o}{\partial t} + \frac{\partial f_1}{\partial x} + \frac{\partial f_2}{\partial y} + \frac{\partial f_3}{\partial z} = 0 \tag{30}$$

where

$$\begin{aligned} f_o &= -A\phi_t - B\phi_x \\ f_1 &= E\phi_x + F\phi_x^2 + G\phi_y^2 \\ f_2 &= \phi_y + H\phi_x \phi_y \\ f_3 &= \phi_z \end{aligned} \tag{31}$$

Time, t, and the Cartesian coordinates x, y, and z are nondimensionalized by the freestream velocity and wing reference chord.

The coefficients A, B and E are defined as

$$A = M^2, \quad B = 2M^2, \quad E = 1 - M^2 \tag{32}$$

Several choices are available for the coefficients F, G and H depending upon the assumptions used in deriving the TSD equation[29]. Briefly, the coefficients are referred to as "NASA Ames" coefficients when defined as

$$F = -\frac{1}{2}(\gamma + 1)M^2, \quad G = \frac{1}{2}(\gamma - 3)M^2, \quad H = -(\gamma - 1)M^2 \tag{33}$$

and are referred to as the "NLR" coefficients when defined as

$$F = -\frac{1}{2}[3 - (2 - \gamma)M^2]M^2, \quad G = -\frac{1}{2}M^2, \quad H = -M^2 \tag{34}$$

The "classical" TSD coefficients are given by

$$F = -\frac{1}{2}(\gamma + 1)M^2, \quad G = 0, \quad H = 0 \tag{35}$$

and finally the coefficients for the linear potential equation, valid for subsonic and supersonic small perturbation flows, are

$$F = G = H = 0 \tag{36}$$

The TSD equation (29) is distinguished from the higher equation level flow models in that, within the small disturbance assumption, the computational grid is not required to move with the body since boundary conditions are imposed at the mean plane, usually $z = 0^{\pm}$. The wing flow tangency condition boundary condition is

$$\phi_z^{\pm} = f_x^{\pm} + f_t \tag{37}$$

where $f^{\pm}(x,y,t) = 0$ describes the upper and lower body surfaces. The trailing wake boundary conditions are

$$[\phi_x + \phi_t] = 0 \tag{38}$$

$$[\phi_z] = 0 \tag{39}$$

where [-] indicates the jump in the indicated quantity across the wake. Equation (37) enforces the convection of vorticity downstream from the trailing edge and eq. (38) requires continuity of the z component of velocity, w, across the wake. The pressure coefficient may be computed using either linear or nonlinear forms of the Bernoulli equation. The exact nonlinear equation is given by eq. (30) where the appropriate density equation for eq. (30) is

$$\rho = [1 - \frac{\gamma - 1}{2} M_\infty^2 (2\phi_x + \phi_x^2 + \phi_y^2 + \phi_z^2 + 2\phi_t)]^{\frac{1}{\gamma - 1}} \qquad (40)$$

Alternatively, the linearized Bernoulli relation gives

$$C_p = -2(\phi_x + \phi_t) \qquad (41)$$

While eq. (41) is the proper choice based upon formal order of magnitude reasoning, the higher order terms in eq. (40) are sometimes not negligible for cases of interest.

Farfield Boundary Conditions: Two forms of farfield conditions have been used for the unsteady TSD equation. Table 3 lists these as "reflecting" and "nonreflecting" boundary conditions. These terms are descriptive only and indicate the relative effects of the two sets of conditions upon unsteady calculations. The nonreflecting conditions are derived[87] from a characteristic variable analysis of solutions to eq. (30) in the farfield. They are implemented as first order plane wave conditions and are intended to prevent the reflection of a major portion of signals incident upon the boundaries back towards the vicinity of lifting surfaces. Note that in the steady state, the time derivatives in eqs. (40 b-g) vanish resulting in simple Neumann "reflecting" boundary conditions. Proper grid design is very important for unsteady calculations and involves consideration of grid extent, grid stretching and boundary conditions. If any one of these factors is not properly treated, spurious unsteady results may be observed.

It is noted that an alternative farfield boundary condition has been shown to be superior for two-dimensional steady calculations. Imposing conditions appropriate to a point vortex of the appropriate strength to match lift[87] has yielded solutions of the Euler equations which were insensitive to computational grid extent, leading to efficient solutions for small grid extents. No

corresponding development for unsteady flows is available.

Table 3. Farfield boundary conditions for the Unsteady TSD potential equation

	Reflecting	Nonreflecting	
Upstream	$\phi = 0$	$\phi = 0$	(40a)
Downstream	$\phi_x + \phi_t = 0$	$\frac{1}{2}(\frac{-B}{C} + \frac{D}{\sqrt{C}})\phi_t + \phi_x = 0$	(40b)
Above	$\phi_z = 0$	$\frac{D}{2}\phi_t + \phi_z = 0$	(40c)
Below	$\phi_z = 0$	$\frac{D}{2}\phi_t - \phi_z = 0$	(40d)
Right spanwise	$\phi_y = 0$	$\frac{D}{2}\phi_t + \phi_y = 0$	(40e)
Left spanwise (for full-span modeling)	$\phi_y = 0$	$\frac{D}{2}\phi_t - \phi_y = 0$	(40f)
Symmetry plane (for half-span modeling)	$\phi_y = 0$	$\phi_y = 0$	(40g)

$$C = E + 2\phi_x \quad , \quad D = \sqrt{4A + B^2/c}$$

Linear Small Disturbance Potential Equation

When the coefficients of eq. (36) are used in eq. (30) the classical linear potential equation results. In dimensional form as given in ref. 88 it is

$$\nabla^2\phi - \frac{1}{a_\infty^2}\phi_{tt} - \frac{2M}{a_\infty}\phi_{xt} - M^2\phi_{xx} = 0 \qquad (43)$$

Equation (43) holds for small disturbances from freestream conditions for subsonic and supersonic flight.

Special cases of eq. (43) have been extensively studied and closed form solutions are available for some cases. In other cases, asymptotic methods provide insight into the form required of numerical solutions. Since these linear solution methods are well calibrated with regard to important issues, such as wing flutter, for speeds up to high subsonic Mach numbers, it behooves practitioners of unsteady CFD to verify their methods, wherever appropriate, against these linear methods.

The important case of steady state, simple harmonic motion has been most extensively studied. With body motion and potential assumed given by

$$f^{\pm}(x, y, t) = \bar{f}^{\pm}(x, y)\, e^{i\omega t} \tag{44a}$$

$$\phi(x, y, z, t) = \bar{\phi}(x, y, z)\, e^{i\omega t} \tag{44b}$$

eq. (40) becomes

$$(1 - M^2)\,\bar{\phi}_{xx} + \bar{\phi}_{yy} + \bar{\phi}_{zz} - \frac{2Mi\omega}{a_\infty}\bar{\phi}_x + \frac{\omega^2}{a_\infty^2}\bar{\phi} = 0 \tag{45}$$

Equivalently, eq. (45) results from applying a Fourier transformation to the time variable in eq. (43). Equations (43) and (45) present the governing equations for unsteady linear aerodynamics in the time domain and the frequency domain. The time domain approach has been valuable in giving insight into the nature of solutions for small values of nondimensional time. On the other hand, the frequency domain approach has provided the majority of the working methods used in aeroelastic design and analysis.

The time domain form of eq. (43) is the basis of the "acoustic planform" analogy used in ref. 97 to calculate the initial transient pressures and loads on airfoils and wings undergoing sinking and pitching motions. Figure 11 shows pressures on an impulisvely started sinking and pitching airfoil for several times during the first four chordlengths of motion. The Mach number is 0.8. The discontinuity in slope of the pressure indicates the progress of the upstream traveling pressure pulse generated at the trailing edge by the impulsive motion. This pulse travels at a speed of (a_∞ - U). The faster downstream traveling pulse (with velocity a_∞ +

U) can be seen in fig. 11(a). The resulting lift and moment transients for several Mach numbers are shown for the first 10 chordlengths of travel between 0 and 2 in fig. 12. Reference 88 discusses the use of piston theory in determining the starting value of pressure and integrated loads. At t = 0 the pressure is a function only of the local normal velocity of the surface, u_o

$$p - p_\infty = \rho_\infty a_\infty u_o \tag{46}$$

This leads to equations such as the following for the initial lift coefficient per unit angle of attack for any plane wing at any Mach number

$$\frac{dc_l(o)}{d\alpha} = \frac{4}{M} \tag{47}$$

Reference 97 also contains time-accurate solutions of eq. (43) for 3-D wings in supersonic flow.

In the alternative frequency-domain approach, extensive use has been made of fundamental solutions (Green's functions) of the governing equation such as the source and vortex potential functions for incompressible flow and the acoustic source pulse and doublet for compressible flow. Due to the linearity of eq. (43), superimposed distributions of these fundamental solutions are made to satisfy the boundary conditions. The assumption of simple harmonic motion, eqs. (44), enables the manipulation of the resulting expressions into functions which may be used to computed the strength of the singularity distribution.

For incompressible flow eq. (43) reduces to Laplace's equation

$$\nabla^2 \phi = 0 \tag{48}$$

For two-dimensional flow and assumed harmonic airfoil motion, Theodorsen[89] derived an analytical solution of (48). Garrick and Rubinow[90] give a closed form solution of (43) for this same problem for supersonic flow while Possio's integral equation (see ref. 88) results from operating upon eq. (43) to produce a singular integral equation relating known downwash velocities, $\bar{w}_a(x)$, on the airfoil to the unknown pressure difference, $\bar{\Delta p}_a$ (eq. 6-111, ref. 88)

$$\bar{w}_a(x) = -\frac{\omega}{\rho_\infty U^2}\int_{-b}^{b} \Delta\bar{p}_a(\xi)\, K\left(M, \frac{k(x-\xi)}{b}\right)d\xi; \qquad -b \le x \le b \tag{49}$$

The kernel function, K, is composed of Hankel or Bessel functions and is a function of the Mach number and the assumed reduced frequency of oscillation, k.

The corresponding singular integral equation for three-dimensional flow has been studied extensively (see, for instance, refs. 88, 91, 92)

$$\bar{w}_a(x, y) = \frac{1}{4\pi}\iint_S \Delta\bar{p}_a(\xi, \eta)\, K[M, k, (x-\xi), (y-\eta)]d\xi d\eta \tag{50}$$

Inversion of eq. (50) via substitution of assumed series expansions for the unknown pressure and numerical quadrature or collocation solution procedures have been used extensively for aeroelasticians. Knowledge of the functional behavior of the pressure loading near surface edges and slope discontinuities has been of great help in constructing suitable loading functions. Tables 4 and 5, from Ashley's[93] survey, illustrate the singular behavior of ΔC_p near wing edges and control surface boundaries. Note particularly the singular behavior for subsonic flow for the cases of control surface edges. (logarithmic, ~ ln $|x - x_c|$) and for wing leading edges (~ $(x - x_l)^{-1/2}$) and side/trailing edges (~ $(y - y_t)^{1/2}$, $(x_t - x)^{1/2}$). Aeroelastic forcing functions are calculated as weighted surface integrals of these pressure loading functions. Attempts to perform these integrations numerically without acknowledging the possibility of such singular behavior can lead to significant errors and influence solution convergence. Rowe and his coauthors[94] have approached this issue by modeling the singular behavior explicitly in their RHOIV "kernel function" computer code. With the singular portion evaluated analytically, the remaining integral equation is regular and straightforward numerical solution possible. An alternative method which is widely used is the doublet-lattice method of Albano and Rodden[95]. Here the lifting surface is divided into small trapezoidal panels (fig. 13). Within each panel line segments of acceleration potential doublets are placed on the panel quarter-chord line. The unknown doublet line strength for each panel is determined by satisfying the known downwash velocity boundary condition at the mid-point on each panel's three-quarter chord line. Thus the problem is reduced to a linear set of algebraic equations for the doublet line strengths. The choice of the 3/4 chord location for downwash evaluation is selected empirically upon noting that this results in the Kutta condition being satisfied. This paneling method can be easily

extended to multiple lifting surfaces as well as to body interference problems.

Comparisons[96] of a convergence study comparing the RHOIV kernel function method and the doublet-lattice method are shown in figs. 14 and 15. Figure 14 shows the real and imaginary parts of unsteady lift and moment for an aspect ratio 4 wing pitching about its trailing edge at k = 0.3, M = 0.9. For this case 6 terms were required for the assumed pressure loading function in RHOIV in order to obtain convergence. The doublet-lattice results indicate that as usual the lift converges faster than the moment and that, for this case, the generalized force magnitudes converge quickly while the phase angles require more terms for convergence. Figure 15 shows a similar comparison for hinge moment due to control surface oscillations of a rectangular wing control surface configuration. The conditions are k = 0.6, M = 0.9 and 10 pressure terms were required for convergence in RHOIV. For up to 18 panels per chord (and up to 6 panels on the control surface) the doublet-lattice result is converging slowly to the RHOIV result. For this case, the kernel function is more efficient in terms of computer resource units (CRUs).

The behavior of solutions of (43) for Mach numbers near unity and/or for high reduced frequencies is of interest for the insight which may be gained of the transition between subsonic and transonic flows. Figure 16, from ref. 98, shows the pressure distribution on an airfoil oscillating in plunge for three values of k. The oscillations, which are most apparent for k = 5, are termed Kutta waves since, for this subsonic condition, they are generated at the trailing edge. For 2-D flow, isolated source solutions of eq. (43) can be viewed as cylindrical pressure waves radiating outwards from the source point at the acoustic speed, a_∞. Viewed from the translating airfoil, two wave fronts traveling at relative speeds of $a_\infty \pm U$ are seen on the z = 0 plane. For high subsonic speeds and low supersonic speeds, the upstream propagating wave, $a_\infty - U$, generates the surface pressure waves seen in fig. 16. The oscillations are in quadrature, with the real part having a cos [R (x - 1)] dependence and the imaginary part having a sin [R (x - 1)] dependence indicating an upstream propagating signal with wave number

$$R = Mk/(1 - M) \qquad (51)$$

radians per semichord. For M = 0.7 and k = 5 the wave number is 11.6 radians per semichord, agreeing with the oscillations shown in fig. 16.

These pressure oscillations are also observed in solutions of (43) for low supersonic Mach

numbers. The pressure difference for oscillatory plunging[98] is

$$\Delta C_p(x, k) = -\left[\frac{8k^2 x}{\beta} f_o(M, x\bar{\omega}) + i\frac{4k}{\beta} e^{-i\bar{\omega}x} J_o\left(\frac{\bar{\omega}x}{M}\right)\right] \frac{h_o}{b} e^{i\omega t} \qquad (52)$$

Figure 17, from ref. 98, gives results for M = 1.02 and k = 0.4. In this case the oscillations are due to the overtaking of upstream traveling waves generated near the leading edge, leading to the supersonic wave number R = Mk/(M - 1) of 20.4 radians per semichord seen in the imaginary part over the forward part of the airfoil. Note the transition near midchord to an oscillation of one-half this wavelength caused by the interaction of the two terms of eq. (52).

These pressure oscillations influence the integrated airfoil loads for Mach numbers near unity as shown in fig. 18[98]. The influence appears to be largest for low supersonic speeds. Also noted the reversal of trend of Re(cl) for M ≈ 0.7 - 0.8, a feature important for aeroelastic analysis.

In concluding this section, the equivalence of the time-domain approach of eq. (40) and the frequency-domain approach of eq. (45) is noted. Edwards[98,99] discusses several misconceptions regarding solutions of eq. (45) for diverging and converging oscillatory motions. Valid solutions of eq. (4) for arbitrary motions are obtained via Laplace transformation of eq. (43). Solutions are functions of the Mach number and the generalized reduced frequency $\bar{s} = b/U(\sigma + i\omega)$. Generalized unsteady aerodynamic methods are becoming widely used for aeroelastic analysis and in the design of active aeroelastic control systems. Figure 19[98] shows a typical result, with the unsteady lift coefficient of a wing given for rigid plunging motions at M = 0.5. Results are given as a function of amplitude, $\bar{r}$, of motion for three phase angles, θ, where $\bar{s} = \bar{r}e^{i\theta}$. Harmonic oscillation results are given by $\theta = 90°$ while converging and diverging motion results are given by 120° and 60° respectively.

Accuracy and Resource Requirements

The previous section briefly surveyed solution methods which are available for the linear potential equation. These methods are well developed and, for the most part, do not tax available computational resources. This is definitely not the case for solution methods of the nonlinear fluid dynamic models to be considered in the remainder of these lectures. There are, in general, no closed form solutions available for these equation sets and iterative numerical methods are the rule. Computational unsteady aerodynamics requires careful selection of equation level

based upon considerations of the flow physics involved, required accuracy and the number of cases required to perform aeroelastic analysis. The discussion of figures 1-8 has summarized the range of flow physics involved in current aeroelastic problem areas. Accuracy requirements are dependent upon the type of flow as delineated in fig. 3. Table 6 summarizes the current accuracy of predictions of key aeroelastic response mechanisms and suggests accuracy requirements for computational aeroelastic analysis. Note that the current accuracy level for high subsonic speed attached flow, the most relevant gage of current capability, is on the order of 10 percent. Novel computational methods will have to do significantly better than this to be competitive.

The resources required are a function of the number of computer operations required per case and the number of cases to be calculated. Tables 5 and 6, from ref. 100, summarize the resources required for typical aeroelastic analyses.

Table 7 indicates the computer resources required to perform a flutter analysis of a complete aircraft configuration at one Mach number. Time-marching transient aeroelastic response calculations are used to determine the flutter condition. This involves, on average, four response calculations: two to calculate steady flow field conditions and two transient responses bracketing the flutter speed. Modal frequency and damping estimates from the responses are determined and the flutter speed interpolated from the damping estimates. Calculations have been performed for a complete aircraft configuration with a transonic small disturbance (TSD) potential code using 750,000 grid points. The calculation of one flutter point for this case on the CDC VPS-32 computer would require 2.3 CPU hours. Estimates of similar calculations using the full Navier-Stokes equations would require 77.8 CPU hours. Conditions for this estimate are; a Reynolds number of 10 million, 7 million grid points and an assumed computational speed of 100 million floating point operations per second (MFLOPS).

Table 8 summarizes computational requirements for flutter calculation of a complete flutter boundary for wing/body/canard configuration on the CDC VPS-32 computer operating at 100 MFLOPS and on the NAS CRAY II computer operating at 250 MFLOPS. Again, four response calculations per flutter point are assumed. It is assumed that ten flutter points will be calculated to define the flutter boundary versus Mach number. The left hand column indicates the difficulty of the flowfield calculation as defined in figure 1; type I for attached flows, type II for mixed (alternately separated and attached) flows and type III for fully separated flows. The second column indicates the fluid dynamic equation level needed to accurately model the flow physics of the problem. Note that two-dimensional strip boundary layer models are assumed for interactive viscous-inviscid calculations for the potential and Euler equation methods. It is

anticipated that potential equation models will be adequate for flutter calculations of type I attached flow conditions and may also be quite useful for some type II mixed flow cases. Full potential equation codes will require about 50 percent more computer resources than TSD methods due to the necessity of conforming, moving grids, among other considerations. Euler equation methods should also be adequate for these conditions and, in addition, be able to treat more difficult type III fully separated flows. Euler equation methods are estimated to require approximately twice the resources of TSD methods. The full Navier-Stokes equations, which should only be required for type II and III flows, require approximately 30 times the resources of the Euler equations (at a Reynolds number of 100 million).

PART III COMPUTATIONAL SOLUTION METHODS

In this lecture, methods which have been developed for the solution of the fluid dynamic flow models described in Part II will be discussed. The presentation will be partly historical, leading from the simpler TSD potential equation to the higher equation level models. Although not always the case, this sequence broadly reflects the progression of research in this area. Solution algorithms will be discussed and results both of historical interest and indicative of the current state will be presented. It is helpful to regard the evolution of progress in this area as following four broad stages:

i.) Early computational demonstrations

ii.) Maturation of computational methods

iii.) Application to realistic configurations

iv.) Type II mixed flow computation

The first three stages are those typically encountered in the development of any novel technology within a given problem area. In the current context, they relate to development of capability of type I attached flow (fig. 3 and Table 4) which has been a dominant focal point of applications. The fourth stage listed serves as a caution to too rigid a categroization as parallel efforts for type II mixed flow calculations have proceeded along side, and sometimes ahead of those for attached flows.

A thread which may be discerned in reviewing this field is the continued evolution of computational methods, with applications and evaluations by comparison with experiment, to successively more difficult cases. Thus, for instance, an algorithm introduced to treat type I attached flow cases is upgraded in capability to enable treatment of more difficult type I and type II cases and possibly even some type III cases.

In the following, results of calculations for a number of the "Computational Test" (CT) cases drawn from the AGARD Standard Aeroelastic 2-D[16] and 3-D[17] configurations will be presented. These experimental cases are mostly for harmonic oscillations of a wind tunnel model in a rigid (i.e. the models have been made as stiff as is practical in order to minimize aeroelastic deformations) degree-of-freedom about a steady mean condition which, for pitching oscillations, is described as

$$\alpha(t) = \alpha_m + \alpha_o \sin kt \qquad (53)$$

The reduced frequency is based upon reference semichord unless otherwise specified.

Response quantities, such as lift coefficient, are measured or calculated for a sufficient number of cycles such that a stable average for the time history of the response is available. The response will, in most cases be cyclical at the frequency of the forced motion, k, but it will in general not be purely harmonic. That is Fourier analysis of the averaged response of, for example, the lift coefficient will give

$$C_l(t) = C_{l_o} + \sum_{n=1}^{\infty} [Re_n(C_l) \sin nkt + Im_n(C_l) \cos nkt]; \; 0 \leq kt \leq 2\pi \qquad (54)$$

with both Re_n (C_l) and Im_n (C_l) having nonzero values for n > 1. Nevertheless, the fundamental response at the forcing frequency, given by Re_1 (C_l) and Im_1 (C_l) is most important since it is most easily measured and almost always accounts for the largest part of the response. The higher harmonics in the response given by the Fourier coefficients with n > 1 indicate the degree of nonlinearity in the aerodynamic response.

The Fourier coefficients in eq. (54) may be obtained by several different approaches. If a number of the harmonic coefficients are desired in order to study nonlinear behavior, then Fast Fourier Transform (FFT) methods are most efficient. On the other hand, if only a few coefficients are of interest, the traditional evaluation via numerical integration is efficient. Finally, the following simple estimate of the fundamental response is useful

$$Re_1(C_l) \approx \frac{1}{2}\left[C_l(t)_{kt=\frac{\pi}{2}} - C_l(t)_{kt=\frac{3}{2}\pi}\right] - C_{l_o} \qquad (55a)$$

$$Im_1(C_l) \approx \frac{1}{2}\left[C_l(o) - C_l(t)_{kt=\pi}\right] - C_{l_o} \qquad (55b)$$

TSD Potential Equation, 2-D

The two-dimensional TSD potential equation has been extensively studied at several levels of approximation. Reference 101 gives details of an alternating direction implicit (ADI) solution algorithm for the equation

$$C\,\phi_{tt} + A\,\phi_{xt} = B\,\phi_{xx} + \phi_{zz} \qquad (56)$$

The potential is normalized by $cU\delta^{2/3}$ where c is the airfoil chord, and δ is the airfoil thickness ratio. The coordinates x, z and time, t, are normalized by c, $c/\delta^{1/3}$ and ω^{-1} where ω is the frequency of unsteady motion. The coefficient $A = 2\,k_c\,M_\infty^2/\delta^{2/3}$ where $k_c = \omega c/U$. In their LTRAN2 code, Ballhaus and Goorjian[14] implemented a solution of the low frequency version of (50) by setting C = 0 and eliminating the time derivative terms the boundary conditions, eqs. (37, 38). In ref. 14 $B = (1 - M_\infty^2)/\delta^{2/3} - M_\infty^m\,(\gamma + 1)\,\phi_x$ where the choice of the exponent is arbitrary. Reference 14 made m a function of M_∞ such that the critical pressure coefficient, C_p^*, predicted by eq. (56) matched the exact isentropic C_p^*. Houwink and van der Vooren[102] extended the range of applicability of LTRAN2 by adding the time dependent boundary condition terms, and solving a modified TSD equation wherein $B = (1 - M_\infty^2)/\delta^{2/3} - M_\infty^2\,(\gamma^* + 1)\,\phi_x$ where $\gamma^* = 2 - (2 - \gamma)M_\infty^2$. The resulting code was termed LTRAN2-NLR. Whitlow[101] extended the LTRAN2-NLR code by implementing Rizzetta and Chin's[103] solution of the complete TSD eq. (50) where $C = k_c^2\,M_\infty^2/\delta^{2/3}$. The resulting code was termed XTRAN2L[104].

The ADI method advances solutions from time step n to time step n + 1 using successive sweeps in the x and z directions

x-sweep:
$$\frac{A}{\Delta t}\,\delta_x\,(\tilde{\phi}_{i,j} - \phi^n_{i,j}) = D_x\,f_{i,j} + \delta_{zz}\,\phi^n_{i,j} \tag{57a}$$

z-sweep:
$$\frac{c}{\Delta t^2}\,(\phi^{n+1}_{i,j} - 2\phi^n_{i,j} + \phi^{n-1}_{i,j}) + \frac{A}{\Delta t}\,\delta_x\,(\phi^{n+1}_{i,j} - \tilde{\phi}_{i,j}) = \frac{1}{2}\,\delta_{zz}\,(\phi^{n+1}_{i,j} - \phi^n_{i,j}) \tag{57b}$$

where $\tilde{\phi}$ is an intermediate level potential and

$$\delta_x\phi = \frac{2}{x_{i+1} - x_{i-1}}\,(\phi_{i,j} - \phi_{i-1,j})$$

$$\delta_{zz}\phi = \frac{2}{z_{j+1} - z_{j-1}}\left[\frac{\phi_{i,j+1} - \phi_{i,j}}{z_{i+1} - z_i} - \frac{\phi_{i,j} - \phi_{i,j-1}}{z_j - z_{j-1}}\right]$$

$$f_{i,j} = \frac{1}{2}\left[\frac{1 - M_\infty^2}{\delta^{2/3}}\,\phi^n_{i,j} + B^n_{i,j}\,\tilde{\phi}_{x_{i,j}}\right]$$

$$B^n_{i,j} = \frac{1 - M_\infty^2}{\delta^{2/3}} - M_\infty^2\,(\gamma^* + 1)\,\phi^n_{x_{i,j}}$$

The mixed difference operator, D_x, is constructed to maintain conservation form. Murman-Cole spatial differencing results in the following form for $D_x f_{i,j}$

$$D_x f_{i,j} = \frac{2}{x_{i+1} - x_{i-1}}\left[(1 - \varepsilon_i)\,(f_{i+1/2,j} - f_{i-1/2,j}) + \varepsilon_{i-1}\,(f_{i-1/2,j} - f_{i-3/2,j})\right] \qquad (58)$$

$$\varepsilon_i = \begin{cases} 0 & C^n_{i+1/2,j} + C^n_{i-1/2,j} > 0 \\ 1 & C^n_{i+1/2,j} + C^n_{i-1/2,j} < 0 \end{cases}$$

With the LTRAN2 code, Ballhaus and Goorjian[14] were able to reproduce Tijdeman's[3] type A, B and C shock motions for the NACA 64A006 airfoil with an oscillating flap. The motions were also demonstrated computationally by Magnus and Yoshihara[13] and Magnus[7] using an explicit Euler equation code. Figure 20, from ref. 14, gives these three calculations. The computational conditions for these cases are

Type	Mach	k	flap amplitude
A	0.875	0.234	1.0 deg.
B	0.854	0.179	1.0 deg.
C	0.822	0.248	1.5 deg.

These conditions are 0.15 - 0.28 Mach lower than Tijdeman's test conditions, very likely due to wind tunnel wall interference. The Euler code used a Lax-Wendroff explicit differencing

solution algorithm and a Cartesian grid with an embedded fine mesh around the moving shocks was used. The boundary conditions were applied at the mean airfoil position. The Euler code used 5484 grid points and required 1500 seconds per cycle whereas the LTRAN2 code required 8 seconds (CDC 7600 computer)[14]. This significant reduction brought the expense of 2-D unsteady transonic CFD calculations within the reach of many researchers.

Monotone Differencing. It has been shown that Murman-Cole differencing allows stable entropy-violating expansion shocks to be computed as part of the numerical solution[104]. Reference 104 showed that it can also trigger numerical instabilities. Figure 21[101] shows such a case for the MBB A-3 airfoil oscillating in pitch about its leading edge at M = 0.8 and k = 0.2. At $k\Delta t = 254°$ an instability is developing on the lower surface at the leading edge that causes program failure within several iterations. When the monotone differencing scheme of Engquist and Osher[106] is used, expansion shocks are not admitted and significant increases in allowable time steps over those allowed by the Murman-Cole scheme are achieved. The Engquist Osher (E-O) scheme was first used in implicit algorithms by Goorjian et al.[105] and a similar implementation is described by Whitlow[101]. The E-O method is incorporated into the ADI procedure by modifying the mixed difference operator D_x in eq. (58) to:

$$\bar{D}_x f_{i-1/2,j} = \vec{\Delta}_x \tilde{f}_{i-1/2,j} + \overleftarrow{\Delta}_x \hat{f}_{i-1/2,j} = \frac{2}{x_{i+1} - x_{i-1}} (\tilde{f}_{i+1/2,j} - \tilde{f}_{i-1/2,j} + \hat{f}_{i-1/2,j} - \hat{f}_{i-3/2,j}) \qquad (59)$$

The $\tilde{f}$ and $\hat{f}$ operators are given in ref. 101.

In the following, examples of results from the XTRAN2L code will be discussed and additional modifications to the ADI algorithm will be described. The nonlinear term, $\phi_x \phi_{xx}$, leads to the formation of shock waves for transonic speeds which the numerical differencing solution schemes are designed to capture. Pressures in the vicinity of a shock can vary in a quite nonlinear fashion with respect to surface motion and the importance of this nonlinearity in aeroelastic applications is of great interest. Typically, applications of unsteady aerodynamics involve not the local unsteady pressures but their integrated value, weighted by shape functions describing surface motion. In 2-D the lift and moment coefficients resulting

from airfoil pitching and plunging motions are the relevant airloads. It has been observed that these airloads behave in a sufficiently "locally linear" manner that linear harmonic analysis methods are quite useful.

Pulse Transient Unsteady Airload Calculations. If the airload response to surface motion is sensibly locally linear then airload frequency response functions may be determined from Fourier transform analysis of transient responses. References 104 and 107 describe the pulse transient method which is based upon this assumption. Starting from a converged steady state solution the airfoil boundary condition eq. (37) is prescribed to simulate an exponentially shaped pulse motion (e.g. pitch).

$$\alpha(t) = \alpha_o + \alpha_1 e^{-w(t - t_c)^2} \qquad (60)$$

Fast Fourier transforms (FFTs) of the lift and moment coefficients and the angle of attack time histories are calculated. The lift and moment FFTs are divided by the angle of attack FFT to obtain the $c_{l\alpha}$ and $c_{m\alpha}$ frequency response functions. Figure 22[108] shows a typical pulse transient result for the NACA 0010 airfoil at M = 0.78 and α_o = 0.0°. The figure shows only the early portion of the transient to illustrate the fluid dynamics resulting from the pulse. Calculations are typically continued for ~ 1000 time steps to allow the loads to return to steady state. Figure 23 shows the resulting airload transfer functions for this case and for similar thickness NACA 64A010 and parabolic arc airfoils. This figure indicates the degree of difference in unsteady airloads which results from the nonlinear transonic steady flow condition. Figure 24 indicates the correlation between airloads obtained using this method and the harmonic oscillation method for a six percent parabolic arc airfoil at M = 0.85. The pulse shape is chosen to give reasonable results for reduced frequencies up to k ~ 2.0. Its use gives considerable detail in the frequency domain from a single transient calculation resulting in a considerable reduction in cost over the harmonic oscillation method.

In order to obtain accurate results with the pulse method careful attention to numerical details is required. In order to avoid spurious low frequency results, the starting value of $\alpha(t)$ in eq. (54) should be equal to α_o. For realistic pulse amplitudes, α_1, w and t_c should be chosen so that $\alpha(o) - \alpha_o = \alpha_1 e^{-wt_c**2} < 10^{-6}$. Also, the method is quite sensitive to lack of convergence in the starting steady-state solution. Drift in the unforced (α_1 = 0) lift coefficient

of 10^{-3} - 10^{-4} can again cause significant low frequency errors.

Computational Grid Dynamic Effects

The pulse trnasient method has been an effective tool in studying the effect of the computational grid upon unsteady calculations. Reference 107 uses this pulse transform technique to demonstrate key features of the relation between computational grids, boundary conditions, and dynamic calculations. The importance of controlling reflections of disturbances from the outer grid boundaries and from internal grid points is shown in fig. 25. In order to compare with linear theory, the case of a flat plate airfoil at M = 0.85 is shown. Three lift coefficient responses resulting from quickly pitching the airfoil from 0 to 1 degree and back to 0 are given. In figs. 25(a) and 25(c) the default XTRAN2L grid given above was used while in figure 25(b) an exponentially stretched grid extending ±200c in x and ±2327c in z was used. The latter grid contained 113 x 97 points in the x and z directions. The default XTRAN2L grid[107] is 80 x 61 points in x, z and covers a fixed physical domain extent of ±20c in x and ±25c in z. An algebraic grid stretching is used to distribute grid points between the airfoil and the outer boundaries. This grid point distribution was selected to alleviate disturbances which can be generated in regions of large grid stretching. On the airfoil the x-grid has 51 grid points having a uniform spacing of 0.02c with an additional point near the leading edge. Figure 25(c) was obtained using the non-reflecting boundary conditions given by Table 3 while figs. 25(a) and 25(b) utilized reflecting boundary conditions. Of particular importance are the outer z-boundaries. The disturbance at $\tau \approx 40$ in fig. 25(a) correlates with the acoustic propagation time for travel to and return from these boundaries. The option of moving these boundaries to large distances, as in fig. 25(b), introduces the complication of severe grid-stretching in the near-field. In this case, reflections from the outer boundaries do not occur, but disturbances seen from $\tau \approx 20$ to 50 correlate with propagation times for travel to and return from regions of the z-grid where grid spacing first becomes more than two chordlengths. Neither of these anomalies is seen in fig. 25(c).

Figure 26 gives the $c_{l\alpha}$ frequency responses calculated from these transient responses. Reflections from the outer z-boundary, fig. 26(a), contaminate the unsteady airloads at low reduced frequencies, $k < 0.15$, whereas the distrubances originating from the near-field grid stretching, fig. 26(b), contaminate the airloads in the frequency range $0.2 < k < 1.0$. Figure 26(c) shows that excellent agreement with linear theory can be achieved for moderate frequencies. Other calculations verify that these features, which are most easily studied for

linearized examples, carry over to nonlinear transonic calculations. Reference 109 gives further examples of computational grid effects for unsteady 3-D calculations.

Viscous-Inviscid Interaction. The inviscid TSD equation (56) does not incorporate viscous effects which can be important for high speed flows. It is possible to account for unsteady viscous effects by coupling a viscous boundary-layer model with an otherwise inviscid analysis. As commonly implemented, the inviscid outer flow solution provides the surface pressure distribution needed to solve the boundary layer equations. This yields the boundary-layer displacement thickness distribution which is used to modify the airfoil surface tangency boundary condition for the next iteration of the outer inviscid flow solution.

Howlett[10] describes such a method implemented in the XTRAN2L code. The effect of a viscous boundary layer for attached turbulent flow is modeled in a quasi-steady manner by means of Green's lag-entrainment equations[111] as implemented by Rizzetta[112]. In this integral method the displacement thickness δ^* is computed as a function of the boundary-layer momentum thickness θ and the shape factor H:

$$\delta^* = \theta \bullet H \tag{61}$$

The functions θ and H are determined together with the entrainment coefficient C_E from Green's lag-entrainment equations. In the nondimensional variables consistent with eq. (56) these equations are

$$\frac{d}{dx}\left(\frac{\theta}{c}\right) = f_1 + f_2\phi_{xx} = \frac{C_f}{2} - (H + 2 - M_e^2)\varepsilon^{2/3}\frac{\theta}{c}\phi_{xx} \tag{62}$$

$$\frac{\theta}{c}\frac{d\overline{H}}{dx} = f_3 + f_4\phi_{xx} = \left(C_E - \frac{H_1}{2}C_f\right)\frac{d\overline{H}}{dH_1} + H_1(H+1)\frac{d\overline{H}}{dH_1}\varepsilon^{2/3}\frac{\theta}{c}\phi_{xx} \tag{63}$$

$$\frac{\theta}{c}\frac{dC_E}{dx} = f_5 + f_6\phi_{xx} = F\left\{\frac{2.8}{H + H_1}\left[(C_\tau)_{EQO}^{1/2} - \lambda C_\tau^{1/2}\right]\right.$$

$$+ \left(\frac{\theta}{U_e}\frac{dUe}{d\xi}\right)_{EQ}\} - F\,[1 + 0.075M_e^2\,\frac{1+\frac{\gamma-1}{2}rM_e^2}{1+0.1M_e^2}]\varepsilon^{2/3}\,\frac{\theta}{c}\,\phi_{xx} \qquad (64)$$

The subscript e in these equations refers to the quantities evaluated at the boundary-layer edge, the subscript EQ denotes the equilibrium conditions, and the subscript EQO denotes the equilibrium conditions in the absence of secondary influences on the turbulence structure. Expressions for the functions contained in eqs. (62) - (64) are listed in Appendix A of ref. 100.

Downstream of the trailing-edge the same equations are applied to each side of the wake surface independently with the skin friction set to zero and the dissipation scale length doubled to account for the observed far field behavior of wakes.

Coupling between the boundary-layer and inviscid analysis is through the boundary conditions on the airfoil and wake, eqs. (37) and (39), which are modified to

$$\phi_z^{\pm} = f_x^{\pm} + f_t^{\pm} + (\delta^*/\delta c)_x^{\pm} \qquad (65)$$

$$[\phi_z] = [\delta^*/\delta c)_x] \qquad (66)$$

Coupling between the inviscid analysis and the boundary-layer is through the quasi-steady pressure gradient, ϕ_{xx}, in eqs. (62) - (64). Explicit coupling between the boundary layer and the inviscid solution is used for the airfoil boundary condition, eq. (65), since this allows a substantial increase in the allowable time step. That is, the last term in eq. (65) is evaluated as

$$(\delta^{*n+1}/\delta c)_x = \frac{1}{\delta c}\,\frac{\delta^{*n}_{i+1} - \delta^{*n}_{i-1}}{x_{i+1} - x_{i-1}} \qquad (67)$$

In the next section results calculated with the XTRAN2L TSD code are compared with experimental results. Results from the interactive viscous-inviscid model will be designated as IV-TSD

Two-Dimensional Transonic Calculations

In this section, comparisons of calculated and experimental unsteady pressures are given for the NACA 64A006 airfoil, the NACA 64A010A airfoil and the NACA 0012 airfoil. The cases are chosen from the AGARD Standard Configuration Computational Test (CT) cases[18] presented in refs. 100 and 113.

NACA 64A006. Tests of this airfoil[3] all involve oscillation about zero mean angle of a flap with hinge axis located at three-quarter chord. The steady flow pressure distributions for Mach numbers from 0.80 to 0.875 are shown in fig. 27. At M = 0.85 the IV-TSD model results agree well with the data while at M = 0.875 the viscous results correct roughly one-half of the discrepancy in the inviscid shock location. Post-shock pressure levels are well predicted by the IV-TSD model. Figure 28 shows the displacement thickness, δ^* for these cases. The thickening of the boundary layer by the shock is apparent for M = 0.85 and 0.875. Figure 29 shows unsteady upper surface pressures at a low reduced frequency, k = 0.06 and at a moderate reduced frequency, k = 0.24. Figures 30 and 31 show the corresponding airloads for these cases. In general, the agreement between experiment and calculations improves with decreasing Mach numbers and increasing frequency. As for the steady pressures, the unsteady results in fig. 29 indicate that the IV-TSD model accounts for a portion of the discrepancy in the shock pulse. The airloads show reasonable agreement with the data for the lower Mach numbers with trends also reasonably predicted. However, with the onset of significant transonic effects at M = 0.85 it is obvious that further computational improvements are called for. Note, in particular, that linear theory continues to perform well for these cases.

NACA 64A010A. These cases are for the model tested at the NASA Ames Research Center[62] in which the model had a small amount of camber and was 10.6 percent thick. These cases are for the model pitching about the quarter-chord at nominally zero degrees pitch angle. Figure 32 gives the calculated and measured steady pressures for M = 0.5 and 0.796 and the displacement thickness for these cases is given in fig. 33. At the lower Mach number, agreement is very good with almost no viscous effect evident. At the higher Mach number, the viscous results move the shock forward several percent chord and slightly weaken the shock strength. The data sets encompass Reynolds numbers variations ranging from 2.5×10^6 to 12.5×10^6 based upon chord and fig. 33 shows the resulting predicted variation in displacement thickness. Figure 34 shows the upper surface unsteady pressure for M = 0.5 and k = 0.10. There is excellent

agreement for this case which is typical of other results for this Mach number. Figure 35 shows upper and lower surface unsteady pressures at M = 0.796 for reduced frequencies from 0.025 to 0.3. Pressure levels ahead of the shock are generally well predicted. The inviscid shock pulse is too strong and too far aft, with both effects being improved by the IV-TSD model. The viscous model also improves the post-shock pressure comparisons. Still, there is again an evident need for further increases in accuracy in the region of the shock which is also apparent in the unsteady airloads shown in fig. 36. Note the characteristic overprediction of ($c_{m\alpha}$) at low values of k only a portion of which is corrected by the viscous model. Similarly, the values of Re ($c_{m\alpha}$) at low values of k appear to have an anomalous trend. Trends due to amplitude of oscillation are well accounted for as is shown in fig. 37. For amplitudes of 0.5, 1.0 and 2.0 degrees, the IV-TSD model very nicely corrects the inviscid shock pulse signature as well as the post-shock pressures.

NACA 0012. This case involves a 12 percent thick symmetrical airfoil tested with free transition for sizable mean angles and oscillation amplitudes as well as cases with constant pitch rate ramping motions to high angles, ref. 18. Results for the latter cases are shown in ref. 113 and demonstrate that the TSD code yields surprisingly good lift coefficient estimates for these transient ramping motions up to angles near stall, $\alpha \sim$ 8-10°. Figure 38 presents results for the former cases, with total lift and pitching moment coefficients plotted versus pitch angle. The first three cases are for oscillations of 2.5 and 5 degrees about non-zero mean angles while the last case is for oscillations of 2.5 degrees about a zero mean angle. Agreement for the lift coefficients varies from good to very good whereas the moment coefficients for the first three cases show a systematic difference with experiments due to underprediction of pressures near the leading edge suction peak in pressure. The characteristic shape of the c_m - α curves for the first three cases is due to a large second harmonic contribution. In contrast, the shape in the fourth case is due to an increased third harmonic component. Viscous results from the IV-TSD model are shown for the first and fourth cases. In the first case, viscous effects produce what appears to be a decreased agreement with experiment. The second and third cases were not amenable to the "direct" IV-TSD model described above since they involve incipient separation. Such cases require an "inverse" boundary layer method to handle mildly separated flows.

Parametric Studies. A number of parametric studies of transonic 2-D unsteady aerodynamics have been published. Bland and Edwards[114] investigated the effects of airfoil

shape for the 10.6 percent thick NACA 64A006 airfoil and the 8.9 percent thick MBB A-3 airfoil. The latter is a supercritical airfoil with significant aft loading. Figure 39 shows the steady pressure distributions on these airfoils for a range of Mach numbers and fig. 40 shows the unsteady pressure magnitude and phase angle due to pitching for the same Mach numbers for k = 0.15. It was observed that the frequency response functions of these two airfoils were very smilar when a Mach number shift of 0.01 was used to account for the thickness difference. Figure 41 shows this comparison for airfoil pitching. Using this Mach number shift, it was shown that the two airfoils exhibited similar transonic flutter characteristics for structural dynamic parameters representative of a swept-back wing section.

The effect of amplitude upon transonic unsteady aerodynamics was also studied[114]. Figure 42 shows pressure distributions due to pitching for the NACA 64A010A airfoil at M = 0.7 and k = 0.15. For oscillation amplitudes from 0.25 to 2.0° normalized pressures ahead of and behind the shock are little affected by varying amplitude while the shock pulse is smeared out with increasing amplitude. Note, however, that the area under the shock pulse remains nearly constant, lending further credibility to the use of locally linear analysis methods. Howlett[110] also investigated amplitude effects with his interactive viscous boundary-layer method and found no significant nonlinear effect for a moderate transonic case. Figure 43 shows lift due to pitch for the NACA 64A010A airfoil at M = 0.796 for 0.1 and 4.0 deg. pitching amplitude.

Batina[108] investigated the effects of airfoil shape, thickness and angle-of-attack using the XTRAN2L code. As a reference, fig. 44 gives the linear $c_{m\alpha}$ frequency response function at M = 0.80 (linearized aerodynamics and flat plate airfoil). Shape effects were investigated using three 10 percent thick airfoils; the NACA 0010, the NACA 64A010 and a parabolic arc airfoil. Figure 45 shows steady pressures for M = 0.76, 0.78 and 0.80. Note the formation of shocks near the locations of maximum thicknesses at 30, 40 and 50 percent chord. Figure 46 gives the $c_{m\alpha}$ frequency responses for these cases. Comparing figs. 44 and 46 two transonic features are apparent. First, the development of nonzero values for Re ($c_{m\alpha}$) at k = 0 with increasing Mach number reflects the aft shift of the steady center of pressure for the NACA 64A010 and parabolic arc airfoils. Secondly, the "wave" feature, seen most prominently in both the real and imaginary responses near k = 0.6 for M = 0.78, is novel. It is apparently independent of airfoil shape and occurs at lower reduced frequency for higher Mach number.

Reference 108 also studied airfoil thickness effects. In steady flow, we have a transonic similarly rule[83] whereby similar airfoils with equal similarity parameters

$$\chi = \frac{1 - M^2}{[\delta\,(\gamma^* + 1)M^2]^{2/3}} \qquad (68)$$

have equal scaled pressure coefficients

$$\frac{C_p\,[(\gamma^* + 1)M^2]^{2/3}}{\delta^{2/3}} = \text{const.} \qquad (69)$$

Figure 47 shows such scaled steady pressures at three similarity scaled Mach numbers for the NACA 0008, NACA 0010 and NACA 0012 airfoils. The similarily parameter values χ_i = 1.4749, 1.3270 and 1.1851 lead to, for example, M_i = 0.76, 0.78 and 0.80 for the NACA 0010 airfoil. The corresponding $c_{m\alpha}$ frequency responses are given in fig. 48. Although no similarity rule is available for the unsteady case, it is interesting to note that, for low and high frequencies, these scaled airfoils behave quite similarly. In contrast, the wave feature which will be identified with "aerodynamic resonance" below does not scale according to eq. (68). Reference 1 points out that such resonances are related to the shock motion types identified by Tijdeman. Figure 49 shows $c_{m\delta}$ frequency responses for the NACA 64A006 airfoil for the two Mach numbers at which type B and C shock motions have been calculated (fig. 19) for the frequencies denoted by the symbols. The type B motion corresponds to the resonance frequency of the aerodynamic resonance feature (the maximum amplitude of Im ($c_{m\delta}$) for this case) at M = 0.854 whereas the type C shock motion frequency is below the M = 0.822 resonance frequency.

Finally, Edwards et al.[115] present parameter studies of 2-D transonic flutter characteristics. The effects of airfoil shape and angle-of-attack are noted and detailed results for a variety of structural dynamic integration methods are shown. Effects of motion amplitude and time step size are also noted.

Shock Generated Entropy

Thus far, transonic unsteady aerodynamic calculations have been presented which

demonstrate the capability of the TSD potential equation to capture nonlinear shock waves and to predict trends for transonic unsteady airloads. An evaluation of figures 29 - 38 indicates that such computations are not accurate enough to displace linear theory. Augmentations to the basic TSD equation and/or resorting to higher equation levels are called for. In this section a significant augmentation to the TSD equation is described.

The conservative full potential and transonic small disturbance potential equations are derived with the assumptions that the flow is irrotational and isentropic. While it is recognized that entropy is generated within shock-waves, the use of potential theories to study transonic flows with weak shocks has progressed assuming that this entropy generation was a higher order effect. It is now understood that disregarding this effect can lead to serious disagreement with more exact solutions for physically interesting situations.

A common approximation in formulating the full potential equations is to impose conservation of mass and energy while satisfying the isentropic and irrotationality conditions[116]. Reference 116 shows that the shock jump conditions for such a "conservative potential" equation deviate from the Rankine-Hugoniot shock conditions as the Mach number ahead of the shock increases. In ref. 116, the implications of this effect were studied by calculating c_l versus α for a range of Mach numbers. It was known[117] that the symmetric NACA 0012 airfoil at $\alpha = 0°$ exhibited multiple solutions for $0.82 < M < 0.85$. Figure 50 shows that such ranges of multiple slutions can be found for all Mach numbers for sufficiently large angles of-attack. More importantly for transonic aeroelasticity, it is concluded that well before α reaches values at which multiple solutions occur, the lift-curve slope, $c_{l\alpha}$, can become unphysically large.

Williams et al.[118] have investigated the effect of nonunique solutions of the unsteady TSD equation. Figure 51[118] gives three different calculations of lift coefficient versus α for the NACA 0012 airfoil at $M = 0.85$. Figure 51(a) gives the upper surface pressure distributions for the three multiple solutions indicated by A, B, and C in fig. 51(b). Solution B is a symmetric nonlifting solution while the other two are lifting solutions. Figure 51(b) gives the lift coefficient versus angle-of-attack for 1.) Quasi-steady conditons, $k = 0$, and pitching oscillations for 2.) $k = 0.01$ and 3.) $k = 0.05$. Solution B is not a stable solution and diverges with an extremely large time constant to either A or C depending upon initial conditions. At $k = 0.05$ the solution oscillates about the positive lifting solution. While the average lift curve slope is not unreasonable the solution must be regarded as anomalous. In contrast, the solution for $k = 0.01$ exhibits a hysteresis loop, jumping between the two stable steady solutions. The

large phase lage implied by this slution is unphysical and caution must be exercised against such calculations.

Fuglsang and Williams[119] implemented a nonisentropic formulation for the 2-D TSD equation. In the 2-D form of eq. (30) the streamwise flux may be written as

$$f = (1 - M^2)u - \frac{1}{2}Bu^2 \tag{70}$$

where $u = \phi_x$. The coefficient B may be chosen in a variety of ways but should be asymptotic to $(\gamma + 1)$ as M approaches unity. Reference 119 replaced eq. (70) with

$$f = (\gamma + 1)M^2R\,(VV^* - \frac{V^2}{2}) \tag{71}$$

where

$$V = \frac{u}{1 + u/(1 + R)}$$

$$R = a^*/U_\infty = \sqrt{1 + \frac{2(1 - M^2)}{(\gamma + 1)M^2}}$$

$$V^* = V(u^*) = \frac{R^2 - 1}{2R}$$

and asterisked quantities refer to sonic conditions. This new flux is identical to that of eq. (70) to $O(u^2)$ when u is small. The new form is derived from a formal asymptotic expansion of the Euler equations, including the effect of shock-generated entropy. A modified pressure coefficient to account for this entropy and a modified wake boundary condition to account for entropy convection complete the nonisentropic modeling. The pressure coefficient is modeled as

$$C_p = C_{p_l} + C_{p_s} \tag{72}$$

where

$$C_{p_l} = -2\,(\phi_x - \phi_t) \tag{73}$$

is the linear isentropic term and c_{ps} is the correction due to the entropy jump

$$C_{p_s} = \frac{2(s - s_\infty)/c_v}{\gamma(\gamma+1)M^2} \tag{74}$$

The entropy jump is evaluated using the computed velocity upstream of the shock and the Rankine-Hugoniot normal shock jump condition

$$\frac{\Delta s}{c_v} = \ln\left[r^\gamma\left(\frac{\varepsilon - r}{\varepsilon r - 1}\right)\right] \tag{75}$$

where

$$\varepsilon = (\gamma+1)/(\gamma-1)$$

$$r = \bar{u}_2/\bar{u}_1 = R^2/\bar{u}_1^2$$

$$\bar{u} = 1 + \phi_x - u_s$$

The wake boundary condition, eq. (38), is modified to account for the entropy as

$$[\phi_x + \phi_t] = \frac{1}{2}[C_{p_s}] \tag{76}$$

The entropy is assumed to be convected down the wake at the freestream speed leading to

$$\frac{\partial}{\partial t}[C_{p_s}] + \frac{\partial}{\partial x}[C_{p_s}] = 0 \qquad (77)$$

Figure 52 shows isentropic and nonisentropic results compared to Euler and full potential results for M = 0.84 and α = 0.25. The nonisentropic results are very similar to the Euler results. No mulitple solution conditions have been observed with the nonisentropic model and values of lift-curve slope are reasonable. Also, low frequency unsteady calculations do not exhibit the hysteresis effect shown in fig. 51(b)[119].

TSD Potential Equation, 3-D

The success of the ADI solution algorithm in enabling efficient 2-D calculations led to its extension to 3-D in the XTRAN3S[28,29] code. In this code, the physical grid lines in the x, y plane conform to the wing planform and the grid is extended in regions off of the wing planform using a shearing transformation to map onto a rectangular computational domain:

$$\xi = \xi(x, y), \quad \eta = y, \quad \zeta = z, \quad \tau = t \qquad (78)$$

In computational space eq. (30) becomes[120]

$$M^2 \frac{\partial}{\partial \tau}\left[\frac{1}{\xi_x}\phi_\tau + 2\phi_\xi\right] = \frac{\partial}{\partial \xi}\left[(1 - M^2)\xi_x\phi_\xi + F\xi_x^2\phi_\xi^2 + G\xi_y^2\phi_\xi^2 + 2G\xi_y\phi_\xi\phi_\eta + G\phi_\eta^2\right.$$

$$\left. + \frac{\xi_y}{\xi_x}(\xi_y\phi_\xi + \phi_\eta) + H\xi_y\phi_\xi(\xi_y\phi_\xi + \phi_\eta)\right] + \frac{\partial}{\partial \eta}\left[\frac{1}{\xi_x}(\xi_y\phi_\xi + \phi_\eta) + H\phi_\xi(\xi_y\phi_\xi + \phi_\eta)\right]$$

$$+ \frac{\partial}{\partial \zeta}\left[\frac{1}{\xi_x}\phi_\zeta\right] \qquad (79)$$

The time-accurate solution of eq. (79) via the ADI algorithm is summarized by Borland and Rizzetta[29]:

ξ - sweep:

$$B\overleftarrow{\delta}_\xi \left(\frac{\tilde{\phi} - \phi^n}{\Delta t}\right) = D_\xi \left[a^n \left(\frac{\tilde{\phi}_\xi + \phi^n_\xi}{2}\right) + b\phi^n_\xi \tilde{\phi}_\xi\right]$$

$$+ 2G_S (\delta_\eta \phi^n) D_\eta (\overleftarrow{\delta}_\xi \phi^n) + \delta_\eta (c\delta_\eta \phi^n) + c\delta_{\zeta\zeta}\phi^n + \delta_\xi X^n + \delta_\eta Y^n \qquad (80a)$$

η - sweep:

$$B\overleftarrow{\delta}_\xi \left(\frac{\tilde{\tilde{\phi}} - \tilde{\phi}}{\Delta t}\right) = \frac{1}{2}\delta_\eta (c\delta_\eta \tilde{\tilde{\phi}} - c\delta_\eta \phi^n) + G_S (\delta_\eta \phi^n) D_\eta (\overleftarrow{\delta}_\xi \tilde{\tilde{\phi}} - \overleftarrow{\delta}_\xi \phi^n) \qquad (80b)$$

ζ - sweep:

$$cA \left(\frac{\phi^{n+1} - 2\phi^n + \phi^{n-1}}{\Delta t^2}\right) + B\overleftarrow{\delta}_\xi \left(\frac{\phi^{n+1} - \tilde{\tilde{\phi}}}{\Delta t}\right) = \frac{c}{2}\delta_{\zeta\zeta} (\phi^{n+1} - \phi^n) \qquad (80c)$$

where $\delta\xi$, $\delta\eta$, $\delta\zeta\zeta$ are second-order accurate central difference operators, $\overleftarrow{\delta}\xi$ is a first-order backward difference operator, $D\xi$ is a mixed-difference operator based on the sign of $(a^n + 2b\,\phi^n_\xi)$ and $D\eta$ is a mixed-difference operator based on the sign of $2\,G_s\,(\delta_\eta\,\phi^n)$. Thus numerical stability is maintained using Murman-Cole differencing. Expressions for a, b, X and Y are given in ref. 29. This algorithm is used to advance the solution for ϕ from time t to time $t + \Delta t$ (i.e. ϕ^n to ϕ^{n+1}). All of the terms contributing to the streamwise portion of the equation are treated implicitly, as well as the second difference $\delta\eta\,(c\delta\eta\phi)$ and $c\delta\zeta\zeta\,\phi$. The remaining cross terms contained in the expressions for X and Y are handled in an explicit manner. Because of this there is an inherent time step limitation for stability of the 3-D method not present for fully implicit methods such as the 2-D ADI method of ref. 14.

A comparison of calculations from the XTRAN3S code with experimental data from a rectangular supercritical wing oscillated in pitch is given in ref. 109. Figure 53(a) shows steady pressures for two span stations at M = 0.7 and $\alpha = 2°$. For this low transonic condition,

the agreement with experiment is good except near the leading edge. The unsteady results in fig. 53(b) are in good agreement with experiment over most of the chord. Inboard, there is an improvement in the prediction of the leading edge suction peak over the linear RHOIV result. Outboard, there is evidence of viscous effects in the phase angle in the aft cove region.

Modified Grid Transformation. The semi-implicit ADI algorithm used in the XTRAN3S code required increasingly small time steps to maintain stability as wing sweep and/or taper were increased. Guruswamy and Goorjian[121] modified the original grid shearing transformation, eq. (20), which resulted in highly skewed outer grid boundaries for such cases. The modified transformation maps from a rectangular physical domain onto a rectangular computational domain while maintaining the alignment of the grid with the wing planform. Reference 120 describes the details of a similar transformation method. In regions upstream and downstream of the leading- and trailing-edges and their extensions, the grid spacing is given by a cubic shearing function, which for the upstream region is

$$x_{i_u} = x_{LE} + A_1\, i_u + A_3\, i_u^3, \quad i_u = 1, \ldots, i_{uP} \tag{81}$$

The coefficients A_1 and A_3 are selected[120] to enforce smooth grid metrics for the grid cells adjacent to the wing. Outboard of the wingtip the leading and trailing edges are extended using similar cubic functions that match the leading and trailing edge slopes at the tip and intersect the far spanwise boundary perpendicularly. Various combinations of spanwise grid point spacing have been studied. Both uniform and cosine-distributions on the lifting surface and uniform and stretched distributions outboard of the wingtip have been used. Figure 54 indicates the grid distribution for the case studied in ref. 120, the RAE tailplane model which was tested for pitching oscillations. It has a leading edge sweep angle of 50.2 deg., a taper ratio of 0.27 and a 10 percent thick NACA 64A010 section profile. Figure 55 shows comparisons of steady pressures for M = 0.80. The agreement is reasonable for the inboard stations. However, the agreement deteriorates at the outboard stations and the pressure expansion over the forward portion of the wing is generally underpredicted. The unsteady pressures for this case with k = 0.490, fig. 56, show good agreement between calculated and measured trends and again deteriorating agreement outboard.

The grids used for the calculations shown in figs. 53-56 contained 60 x 20 x 40 points in

the x, y and z directions for a total of 48,000 points. This is considered to be a medium-to-coarse grid and 5-6 times this number of grid points appear to be required to insure accurate calculations for a single lifting surface. In terms of computational efficiency, ref. 29 indicates a machine speed of 83 μs. per grid point per time step for a CDC 7600 computer.

Shock-Generated Entropy. Gibbons et al.[122] modified the XTRAN3S code to account for shock-generated entropy in a manner similar to ref. 119. The streamwise flux, eq. (31), is replaced by

$$f_1 = (\gamma + 1)M^2R\,(VV^* - V^2/2) + G\phi_y^2 \qquad (82)$$

and the pressure and wake condition modified as in eqs. 72-77. Reference 122 indicates that for a 3-D rectangular wing multiple solutions occur for aspect ratios greater than 24. For more reasonable aspect ratios, unacceptable solutions can be calculated if entropy generation is not taken into account. Figure 57 shows such a case wherein the unmodified code predicts a lift-curve slope twice as large as the modified code which is in agreement with an independent Euler equation calculation. Reference 122 also discusses implementation of Engquist-Osher monotone differencing in the XTRAN3S code. This resulted in improvement in calculated pressures near shocks. Figures 58 and 59 show original and modified XTRAN3S steady and unsteady pressures for the RAE tailplane model at M = 0.90 and k = 0.44. The entropy modifications result in 5-10 percent chord forward shifts of the shock and shock pulse in the outboard wing region.

Treatment of Realistic Configurations

All results presented thus far have dealt with unsteady aerodynamics for isolated lifting surfaces. In order to realize necessary improvements over existing aeroelastic analysis methods, computational methods are required to provide reliable predictions for complex configurations.

Multiple Lifting Surface Interference - Batina[123] extended the ADI algorithm of the XTRAN3S code to allow two lifting surfaces. Figure 60 illustrates a case of canard-wing interference in which unsteady loads are induced on the wing by the oscillating canard. This effect is obviously a function of the separation distance between the surfaces, the Mach number and the frequency.

Wing-Fuselage Interference - Batina[124,85] has also implemented modifications to the TSD equation to treat wing-fuselage interference. For a body at angle of attack α_b and at yaw angle β_b, the exact flow tangency boundary condition may be written as[124]

$$N_t + N_x (1 + \phi_x) + N_y (\phi_y + \beta_b) + N_z (\phi_z + \alpha_b) = 0 \qquad (83)$$

where N(x, y, z, t) = 0 defines the body surface. Computationally, bodies are modeled by applying simplified boundary conditons on a prismatic surface rather than on the true surface as shown in fig. 61. This method is consistent with the small-disturbance approximation and treats bodies with sufficient accuracy to obtain the correct global effect on the flow field without the use of special grids or complicated coordinate transformations. The appropriate boundary conditons imposed on the computational surface are

Upstream face: $$\phi_x = V_{inlet} - 1 \qquad (84a)$$

Downstream face: $$\phi_x = V_{exit} - 1 \qquad (84b)$$

Left/right faces: $$\phi_y = C_t \left[\frac{N_x}{N_y} + \frac{N_t}{N_y}\right] - C_a \beta_b \qquad (84c)$$

Top/bottom faces: $$\phi_z = - C_t \left[\frac{N_x}{N_z} + \frac{N_t}{N_z}\right] \qquad (84d)$$

where V_{inlet} and V_{exit} are inlet and exit flow velocities, respectively, specified in the case of a nacelle. The parameters C_t and C_a are thickness and angle-of-attack corrections derived from slender body theory to account for the differences between the true and computational body surfaces.

Figure 62[124] gives results from these modifications to the XTRAN3S code for the RAE wing-fuselage tested at M = 0.90 and α = 1°. Results for the wing-alone case, not shown, indicate that fuselage effects are similar to the results shown for M = 0.91. Figure 63 shows the

calculated interference effect for this configuration for an assumed wing bending mode. The interference effect on the integrated generalized force, important for aeroelastic analysis is approximately 5 percent of the total.

Approximate-Factorization of the TSD Equation

The numerical stability restrictions of the ADI solution method for the 3-D TSD equation (29) have limited its applications for transonic unsteady calculations. An alternative solution algorithm[84], termed an approximate-factorization (AF) method, has shown much improved stability characteristics. This AF method involves a local time linearization procedure coupled with a Newton iteration technique which is based upon the work of Shankar et al.[125] who applied the method to the full potential equation. It is formulated by first approximating the time derivative terms (ϕ_{tt} and ϕ_{xt}) in eq. (30) by second-order accurate formulae, followed by the substitution of $\phi = \phi^* + \Delta\phi$ and the neglect of squares of derivatives of $\Delta\phi$. In this method, ϕ^* is the current estimate of ϕ^{n+1} which will be converged to the true potential ϕ^{n+1} thus driving $\Delta\phi$ to zero. Performing these operations and summing terms results in

$$\frac{2A}{\Delta t^2}\Delta\phi + \frac{3B}{2\,\Delta t}\Delta\phi_x - \frac{\partial}{\partial x}(E\,\Delta\phi_x + 2F\,\phi_x^*\,\Delta\phi_x + 2G\phi_y^*\,\Delta\phi_y)$$

$$- \frac{\partial}{\partial y}(\Delta\phi_y + H\phi_x^*\,\Delta\phi_y + H\phi_y^*\,\Delta\phi_x) - \frac{\partial}{\partial z}(\Delta\phi_z) = - A\,\frac{2\phi^* - 5\phi^n + 4\phi^{n-1} - \phi^{n-2}}{\Delta t^2}$$

$$- B\,\frac{3\phi_x^* - 4\phi_x^n + \phi_x^{n-1}}{2\Delta t} + \frac{\partial}{\partial x}(E\,\phi_x^* + F\,\phi_x^{*2} + G\,\phi_y^{*2}) + \frac{\partial}{\partial y}(\phi_y^* + H\phi_x^*\phi_y^*) + \frac{\partial}{\partial z}(\phi_z^*) \qquad (85)$$

The right hand side is simply the TSD equation which may be evaluated using known potentials ϕ^*, ϕ^n, ϕ^{n-1}, and ϕ^{n-2}. Transforming to computational coordinates, rewriting eq. (85) in conservation form and approximately factoring the left hand side into a triple product of operators yields

$$L_\xi L_\eta L_\zeta \Delta\phi = -R(\phi^*, \phi^n, \phi^{n-1}, \phi^{n-2}) \tag{86}$$

where

$$L_\xi = 1 + \frac{3B}{4A}\xi_x \Delta t \frac{\partial}{\partial\xi} - \xi_x \frac{\Delta t^2}{2A}\frac{\partial}{\partial\xi} F_1 \frac{\partial}{\partial\xi} \tag{87a}$$

$$L_\eta = 1 - \xi_x \frac{\Delta t^2}{2A}\frac{\partial}{\partial\eta} F_2 \frac{\partial}{\partial\eta} \tag{87b}$$

$$L_\zeta = 1 - \xi_x \frac{\Delta t^2}{2A}\frac{\partial}{\partial\zeta} F_3 \frac{\partial}{\partial\zeta} \tag{87c}$$

$$F_1 = E\xi_x + 2F\xi_x^2\phi_\xi^* + 2G\xi_y(\xi_y\phi_\xi^* + \phi_\eta^*) + \frac{\xi_y^2}{\xi_x}(1 + H\xi_x\phi_\xi^*) + H\xi_y(\xi_y\phi_\xi^* + \phi_\eta^*) \tag{87d}$$

$$F_2 = \frac{1}{\xi_x}(1 + H\xi_x\phi_\xi^*) \tag{87e}$$

$$F_3 = \frac{1}{\xi_x} \tag{87f}$$

$$R = -\xi_x \frac{\Delta t^2}{2A}\left\{ -\frac{A}{\xi_x}\frac{2\phi^* - 5\phi^n + 4\phi^{n-1} - \phi^{n-2}}{\Delta t^2} - B\frac{3\phi_\xi^* - 4\phi_\xi^n + \phi_\xi^{n-1}}{2\Delta t}\right.$$

$$\left. + \frac{\partial}{\partial\xi}\left[E\xi_x\phi_\xi^* + F\xi_x^2\phi_\xi^{*2} + G(\xi_y\phi_\xi^* + \phi_\eta^*)^2 + \frac{\xi_y}{\xi_x}(\xi_y\phi_\xi^* + \phi_\eta^*) + H\xi_y\phi_\xi^*(\xi_y\phi_\xi^* + \phi_\eta^*)\right]\right.$$

$$+ \frac{\partial}{\partial \eta}\left[\frac{1}{\xi_x}(\xi_y \phi^*_\xi + \phi^*_\eta) + H\phi^*_\xi (\xi_y \phi^*_\xi + \phi^*_\eta)\right] + \frac{\partial}{\partial \zeta}\left[\frac{1}{\xi_x}\phi^*_\zeta\right]\} \qquad (87g)$$

Equation (86) is in the form of Newton's method for the solution of the nonlinear system of equations

$$R(\phi^{n+1}) = 0 \qquad (88)$$

which is given by

$$R(\phi^{n+1}) = R(\phi^*) + \left(\frac{\partial R}{\partial \phi}\right)_{\phi=\phi^*} (\phi^{n+1} - \phi^*) = 0 \qquad (89)$$

or

$$\phi^{n+1} = \phi^* - \left[\left(\frac{\partial R}{\partial \phi}\right)_{\phi=\phi^*}\right]^{-1} R(\phi^*) \qquad (90)$$

By iteratively solving (90), $\Delta\phi$ will approach zero so that $\phi^{n+1} = \phi^*$. In general, only one or two iterations are required to achieve acceptable accuracy since the Newton iteration process is quadratically convergent. Equation (86) is solved using three sweeps through the grid by sequentially applying the operators L_ξ, L_η, and L_ζ as

ξ - sweep: $\qquad L_\xi \bar{\Delta\phi} = -R \qquad (91a)$

η - sweep: $\qquad L_\eta \bar{\bar{\Delta\phi}} = \bar{\Delta\phi} \qquad (91b)$

ζ - sweep: $$L_\zeta \Delta\phi = \Delta\bar{\bar{\phi}} \qquad (91c)$$

Central difference formulas are employed for all of the derivatives on the left-hand side of eqs. (91) except for the second term in the L_ξ operator (from the ϕ_{xt} term) which is backward differenced to maintain stability and the third term in the L_ξ operator which is split into streamwise and spanwise components. The resulting terms are centrally differenced at subsonic points and the streamwise terms are upwind-biased at supersonic points using the Murman-Cole type dependent mixed difference operator. The terms on the right hand side of the ξ-sweep are also approximated using central-difference operators except for the ϕ_{xt} term which is backward differenced and for terms in the streamwise direction which are upwind biased at supersonic points. Since the L_ξ, L_η, and L_ζ operators only contain derivatives in their respective coordinate directions, all three sweeps may be vectorized. Finally, ref. 126 describes two additional improvements to the algorithm: second-order accurate supersonic differencing for improved accuracy and Engquist-Osher monotone differencing which again enhances stability.

Figures 64 and 65, from ref. 125, compare results from the XTRAN3S ADI code and the AF algorithm for the F-5 wing model. Figure 64 compares steady pressures at M = 0.9 and $\alpha = 0°$ while fig. 65 compares unsteady upper surface pressures for k = 0.137. Results from the two algorithms agree, as they should, and they also are in very good agreement with experiment. The AF algorithm is also capable of calculating supersonic freestream conditons. Figure 66 gives an example of unsteady lower surface pressures for the F-5 model at M = 1.1 showing good comparison with experiment for this relatively low supersonic case.

The AF algorithm is implemented in a computer code termed CAP-TSD (Computational Aeroelasticity Program - Transonic Small Disturbance) developed at NASA Langley Research Center[84]. The code permits the aeroelastic analysis of complete aircraft through the modeling of multiple lifting surfaces and bodies including canard, wing, tail, control surfaces, launchers, pylons, fuselage, stores and nacelles. Reference 84 presents results for five configurations illustrating this capability. Figure 67 indicates the modeling of a General Dynamics F-16C aircraft model using four lifting surface and two bodies. Figure 68 compares calculated and measured steady pressures for this model at M = 0.9 and $\alpha = 2.38°$. The agreement is considered very good. In fig. 69, calculated unsteady pressures for the complete aircraft and for

the wing-alone are compared for the case of rigid pitching oscillations for k = 0.1. There is a general lack of unsteady experimental data for complex configurations with which to validate such computations. The grid used for these calculations contained 324,000 points. The calculations required 0.88 CPU seconds per time step or 2.7 μs. per grid point per time step on the CDC VPS-32 computer. Thirteen million words of memory was required.

A primary application of unsteady aerodynamics for lifting surfaces is the calculation of aeroelastic response; that is, the response of elastic structures interacting with the aerodynamic loading. The integrity of the structure must be insured under all possible operating conditions and thus the prediction of instability, or flutter, boundaries is required. Reference 127 describes such calculations for a proposed AGARD standard aeroelastic flutter model configuration. This 45° sweptback wing with a taper ratio of 0.66 is shown in fig. 70. A finite element structural dynamic model provides normal vibration mode shapes, frequencies and generalized masses required for a flutter analysis. These uncoupled modal equations of motion are implemented in the CAP-TSD code and time-accurate transient response calculations obtained[127].

Figure 71 shows the mode shapes of the four lowest frequency modes used in the analysis. Transient responses for values of dynamic pressure below and above the flutter boundary are processed to obtain the frequency and damping of the aerodynamically coupled modal responses. Figure 72 compares experimental and computed flutter boundaries for Mach numbers from 0.338 to 1.141. Figure 72(a) shows the flutter speed index, $U/b\omega_\alpha \sqrt{\mu}$, and fig. 72(b) the frequency ratio, ω/ω_α, of the flutter mode, where ω_α is the first torsion mode wind-off frequency. For this 4 percent thick wing, transonic effects are delayed to high subsonic Mach numbers and linear theory results from both CAP-TSD and a kernel function program, are in very good agreement with experiment up to M = 0.98. The three nonlinear CAP-TSD subsonic flutter calculations better agree with experiment than the linear theory, particularly for the change in slope of the flutter boundary near M = 0.95. Note the excellent prediction of the supersonic "backside" of the flutter dip.

Unsteady Potential Equation

The length of the previous sections dealing with solution methods and modifications for the unsteady TSD potential equation reflects the large amount of effort which has been expended upon this equation level. Fewer results are available for the higher equation levels. However, as work on the TSD equation has obviously matured, an acceleration of work on the potential

equation, and the Euler and Navier-Stokes equations is evident. In this and the remaining sections, key algorithms and results for these fluid dynamic models will be summarized. The major issues to be addressed involve computational grids and increased problem size. All of the fluid dynamic flow models above the TSD equation require solutions to be obtained upon the actual body surface, which is usually accomplished with a body conforming grid. For problems involving body motion, such grids probably need to be moved along with the body.

The 2-D unsteady potential equation, eq. (23), is solved in ref. 82 using an approximate factorization algorithm. The time derivative of density is linearized about previous time levels such that conservation form is maintained and the resulting equation becomes

$$L_\xi L_\zeta \Delta\Phi = F \tag{92}$$

where

$$L_\xi = [I + hU^n\delta_\xi - \frac{h^2}{\beta^n}\delta_\xi (\bar{\rho} A_1)^n \delta_\xi]$$

$$L_\zeta = [I + hW^n\delta_\zeta - \frac{h^2}{\beta^n}\delta_\zeta (\bar{\rho} A_3)^n \delta_\zeta]$$

$$F = (\Phi^n - \Phi^{n-1}) + \frac{\beta^{n-1}}{\beta^n}(\Phi^n - 2\Phi^{n-1} + \Phi^{n-2}) + \frac{h}{\beta^n}(\bar{\rho}^n - \bar{\rho}^{n-1})$$

$$+ h\frac{\beta^{n-1}}{\beta^n}(U^{n-1}\delta_\xi + W^{n-1}\delta_\zeta)(\Phi^n - \Phi^{n-1}) + \frac{h^2}{\beta^n}[\delta_\xi(\frac{\tilde{\rho U}}{J})^n + \delta_\zeta(\bar{\rho}W)^n - F_\infty]$$

The terms A_1 and A_3 are metric terms, $\delta\xi$ and $\delta\zeta$ are central difference operators and

$$\Delta\Phi = \Phi^{n+1} - \Phi^n, \quad h = \Delta\tau, \quad \bar{\rho} = \rho/J, \quad \beta = \rho^{2-\gamma}/J$$

Reference 82 uses the concept of flux-biasing[128] to stabilize the numerical scheme. The

spatial terms on the right hand side of eq. (92) are centrally differenced about node (i, j) to give

$$\delta_\xi \left(\frac{\tilde{\rho}U}{J}\right)_{i,j} = \left(\frac{\tilde{\rho}U}{J}\right)_{i+1/2,j} - \left(\frac{\tilde{\rho}U}{J}\right)_{i-1/2,j} \tag{93a}$$

$$\delta_\zeta (\bar{\rho}W)_{i,j} = (\bar{\rho}W)_{i,j+1/2} - (\bar{\rho}W)_{i,j-1/2} \tag{93b}$$

The biased density in the ξ direction is defined as

$$\tilde{\rho}_{i+1/2,j} = \frac{1}{q_{i+1/2,j}} [\rho q - (\rho q)^-_{i+1/2,j} + (\rho q)^-_{i-1/2,j}]$$

where

$$(\rho q)^- = \rho q - \rho^* q^* \qquad q > q^*$$

$$0 \qquad q \le q^*$$

This flux biasing has the effect of introducing artificial viscosity in supersonic regions which is necessary to capture shocks. Although it is generally necessary to bias the density in both computational directions, ref. 82 found that biasing only the ξ direction was satisfactory. Reference 128 explores the connections between this flux biasing and the Murman-Cole and Engquist-Osher differencing schemes.

The flux-biasing solution method has the following desirable features: (a) it accurately tracks sonic conditons and requires no empirical constants to specify the amount of artificial viscosity, (b) it produces no velocity overshoots at shock waves, allowing for larger time steps for unsteady calculations, (c) it produces well-defined, monotone shock profiles with a maximum two point transition between upstream and downstream states, and (d) it dissipates expansion shock waves, ruling out solutions with such nonphysical characteristics. Shankar et al.[130] have also used flux-biased differencing in unsteady potential equation calculations.

Reference 82 also presents an entropy correction method to account for shock generated entropy. The correction consists of replacing the isentropic density by a nonisentropic density

$$\rho = \rho_i e^{-\Delta s/R} \tag{84}$$

where the entropy jump Δs is a function of the Mach number normal to the shock. The nonisentropic pressure coefficient is given by

$$C_p = \frac{2}{\gamma M_\infty^2}\left[(\rho_i e^{-\Delta s/R})^\gamma - 1\right] \tag{95}$$

and, as for the TSD equation nonisentropic modifications, the entropy jump is convected along the wake downstream of the trailing edge.

Treatment of moving, body conforming grids has been handled in several different manners. For 2-D airfoil sections and 3-D rigid wings, a single grid generated for a nominal body orientation may be calculated. Rotations and translations of the entire grid[81] can then be used to track the motion of such bodies. An alternative is to calculate two grids for the extremes of body motion and linearly interpolate grid point locations for intermediate body orientations[26]. Figure 73[82] illustrates this latter method showing calculated grids for 0° and 45° and interpolated grids for 15 deg. and 30 deg. The large amplitudes of this examples serve to demonstrate the method. The double wake grid line for these potential equation applicatons is shown opened for clarity. For the potential equation, the location of this wake cut is important since it defines the path taken by the convected vorticity. Reference 131 studies the effect of using linear, quadratic and cubic curves to define the wake cut and shows a singificant effect upon calculated lift results.

Figure 74, from ref. 82, shows isentropic and nonisentropic potential equation calculations for the NACA 0012 airfoil oscillating in pitch at M = 0.755 and for $\alpha(\tau) = 0.016° + 2.51°$ sin $(k\tau)$ where k = 0.814. The effects of the entropy corrections are to weaken the shock and move it forward, in bettter agreement with the experimental data. At points in the cycle where the shocks become strong, the measured pressures immediately behind the shocks show the effects of boundary layer thickening, which is not included in these inviscid calculations. Reference 129 gives further examples of potential equation calculations for the AGARD Standard

Configurations.

Euler and Navier-Stokes Equations

Since the Euler equations, (14), may be obtained from the Navier-Stokes equations by deleting viscous terms such as $\hat{H}_v$ in eq. (1), solution algorithms for both equations sets may be discussed together. Edwards and Thomas[1] survey methods which have been used.

The time-dependent Euler equations form a hyperbolic system of equations, and much of the recent progress in algorithm development[132-137] has hinged upon the incorporation of the signal propagation features of the differential equation into the numerical algorithm. There are several methods of incorporating this information into a difference scheme, for example flux-vector-splitting or flux- difference-splitting, and an excellent review of the current developments in the field is given by Roe in Ref. 138. The advantages of incorporating an upwind-biased discretization into a numerical algorithm are twofold: (1) the scheme becomes naturally dissipative so that no adjustable constants need to be fine-tuned to a particular application and (2) improved implicit schemes can be devised for more efficient solution to both steady and time-dependent problems. Both of these advantages offset the disadvantage that approximately twice as many operations per time step are required to implement an upwind scheme as opposed to a central difference scheme.

Most of the calculations made to date with upwind difference schemes, especially for airfoils/wings, have been steady-state applications, for which comparable accuracy can be obtained by central difference methods with added artificial viscosity. The advantages of upwind differencing should be more significant for time-dependent problems, however, where the ability to treat rapid movement of flows with shocks is required. Roe[138] gives several examples of shock-propagation computations in two-dimensions which demonstrate clearly the advantages of a characteristic-based scheme. Viscous effects can also be readily introduced into upwind difference schemes developed for the Euler equations by central differencing the shear stress/heat transfer terms[139,140].

The time-accurate computations made by Steger and Bailey[25] and Chyu et al.[26,27] used a spatially-split approximate-factorization (ADI) scheme, which is unconditionally stable in two dimensions but at most conditionally stable in three dimensions. Alternate factorizations are possible with the incorporation of an upwind difference discretization in one or more coordinate directions which can lead to unconditionally stable 3-D algorithms[132]. A two-factor eigenvalue split scheme for the Euler equations has an increased stability limit and fewer operations than

the spatially-split scheme, although the operations are not completely vectorizable. Belk[42] computed steady and time-dependent inviscid flows for the NASA RSW model with such an algorithm in combination with a blocked-grid strategy. Ying et al.[142] used upwind differences in a single coordinate direction and constructed a two-factor unconditionally stable algorithm for which thin-layer viscous effects are readily incorporated. Applications of the thin-layer Navier-Stokes equations to the high-angle-of-attack unsteady flow over a hemisphere-cylinder are made[142]. Several of these alternate factorizations are investigated in the context of efficient algorithms for three-dimensional steady-state problems by Anderson et al.[143,144].

The use of multigrid techniques to accelerate convergence to the steady-state is becoming widespread in the aerodynamic community. These techniques can also be used for time-dependent flows. For instance, multigrid techniques could be used to efficiently solve the large banded matrix equations arising from implicit time discretizations, the solution of which is generally approximated through relaxation and/or factorization methods. Jesperson[145] has demonstrated a time-accurate multiple grid procedure which was used to overcome the small timestep limitation of an explicit scheme. With the growing memory of today's computers (the Numerical Aerodynamic Simulator has 256 million words of memory) it becomes feasible to solve the banded matrices by direct Gaussian elimination, rather than by approximate techniques. The structure of future implicit algorithms for both steady and time-dependent problems will likely involve a multiple grid algorithm with direct elimination techniques used on the coarser grid levels.

Anderson et al.[81] implement the solution to Euler equations for a moving grid, eq. (14), using flux vector splitting with upwind differencing. An iterative Newton linearization is used to advance the solution in time similarly to eqs. (88) - (89). That is, eq. (1) is reformulated as

$$\hat{\hat{L}}(\hat{Q}^{n+1}) = 0 \tag{96}$$

where the form of the operator is

$$[(1 + \tfrac{\phi}{2})\hat{Q}^{n+1} - (1 + \phi)\hat{Q}^{n} + \tfrac{\phi}{2}\hat{Q}^{n-1}]\frac{1}{\Delta t}$$

$$[\delta_\xi^- \hat{F}^+ + \delta_\xi^+ \hat{F}^- + \delta_\eta^- \hat{G}^+ + \delta_\eta^+ \hat{G}^- + \delta_\zeta^- \hat{H}^+ + \delta_\zeta^+ \hat{H}^-]^{n+1} = 0 \qquad (97)$$

If $\phi = 0$, the scheme is first order accurate in time while if $\phi = 1$, the scheme is temporally second order accurate. Conditions required for the split flux terms in eq. (97) are given in ref. 81. Equation (96) is a nonlinear equation which can be solved iteratively by Newton linearization

$$\frac{\partial \hat{L}}{\partial \hat{Q}} (\hat{Q}^{l+1} - \hat{Q}^l) = - L(Q^l) \qquad (98)$$

where l is a sequence of iterates and at convergence, $\hat{Q}^{l+1} - \hat{Q}^{l=0}$, $\hat{Q}^l = \hat{Q}^{n+1}$. A spatially-split approximate factorization scheme is used to solve (90) in three sweeps in each coordinate direction

$$[(I + \frac{\phi}{2}) + \Delta t \delta_\xi^- \hat{A}^+ + \Delta t \delta_\xi^+ \hat{A}^-] \Delta \hat{Q}^* = - \Delta t \hat{L}(\hat{Q}^l)$$

$$[(I + \frac{\phi}{2}) + \Delta t \delta_\eta^- \hat{B}^+ + \Delta t \delta_\eta^+ \hat{B}^-] \Delta \hat{Q}^{**} = (I + \frac{\phi}{2}) \Delta \hat{Q}^*$$

$$[(I + \frac{\phi}{2}) + \Delta t \delta_\zeta^- \hat{C}^+ + \Delta t \delta_\zeta^+ \hat{C}] \Delta \hat{Q}^l = (I + \frac{\phi}{2}) \Delta \hat{Q}^{**}$$

$$\hat{Q}^{l+1} = \hat{Q}^l + \Delta \hat{Q}^l$$

where $\hat{A}^\pm$, $\hat{B}^\pm$, $\hat{C}^\pm$ correspond to Jacobean matrices of $\hat{F}^\pm$, $\hat{G}^\pm$, $\hat{H}^\pm$ respectively.

Figures 75 and 76 from ref. 81, show calculations for the pitching NACA0012 airfoil for the same conditions as in figures 37(d) and (73). The computations were obtained on a 193 x 33 C-grid using a time step of 0.10. Figure 75 compares results from two alternative splitting methods; flux vector splitting, FVS, and flux difference splitting, FDS. The comparison of both of the euler equation results with experiment is very good except near the base of strong shocks.

Reference 146 presents the Euler equations in a formulation wherein the fluid dynamic equations are developed for a coordinate system rigidly attached to the translating and rotating

body. Solutions for two-dimensional oscillating airfoil problems are obtained using an implicit approximate factorization method with artificial dissipation. Results for the oscillating NACA0012 airfoil are shown in figs. 77 and 78. A C-grid with 128 x 64 cells was used for these calculations. Comparing figs. 38(d), 76, and 77 indicates that the two Euler equation results appear to be converged while the TSD solution indicates the magnitude to be expected from viscous effects.

Reference 146 also presents results for unsteady locally conical flow about a sharp-edged delta wing in supersonic flow for rolling oscillation about zero angle of attack. Figure 79 shows the spanwise pressure distribution at four instants during a cycle of oscillation for M = 2 and k = $\omega c/U$ = 1.337. The formation of the leading edge vortex and its migration are clearly evident as is the phase lag of the pressure loading.

The final example of Euler equation calculations to be presented is from the flux-vector splitting scheme of ref. 81. Figures 80 and 81 show steady and unsteady pressures for the F-5 wing model oscillating in pitch. Figure 80 presents comparisons with experimental steady pressures for Mach numbers from 0.90 to 1.328. Agreement is very good to excellent except near the strong shock at M = 0.95. Unsteady pressure comparisons, fig. 81, for M = 0.95 and 1.32 show very good agreement in pressure levels. There are generally insufficient data to resolve the shock pulses near the leading and trailing edges at M = 0.95. These calculations were obtained on a 129 x 33 x 33 C-H mesh. A time step of 0.05 was used requiring approximately 240 time steps per cycle of oscillation.

The retention of viscous terms leads back to the Navier-Stokes equations represented by eqs. (1) - (13). The detailed viscous flow modeling of which this equation set is capable makes it appropriate for the study of viscous dominated unsteady flows characterized in fig. 3 as type II and type III. They may aso be used in the calibration of lower equation level flow models for appropriate classes of unsteady fows such as type I attached flow.

Steger and Bailey[25] provided an early computational demonstration of the use of CFD methods in aeroelasticity. They studied a case of aileron buzz for the P-80 aircraft which had been tested in a wind tunnel. Aileron buzz is a one-degree-of-freedom aeroelastic instability, usually of limited amplitude, which may be encountered for transonic flow conditions. They implemented the Beam-Warming implicit Approximate Factorization (AF) solution algorithm, using an algebraic eddy viscosity turbulence model. A novel treatment of the computational grid was used to follow the aileron motion with a conforming grid. A simple shearing transformation in the coordinate normal to the aileron was used.

Figure 982shows the limit amplitude "aileron buzz" oscillation which was calculated for M = 0.82, Re = 20 x 10^6 and α = -1. The calculation was initiated with a 4 degree aileron offset. This and other calculations successfully reproduced the experimental buzz boundary. The computed reduced frequency was k = 0.38. The shock motion observed in the calculations was type B, and type II intermittent fow separation is shown in ref. 25. The code was capable of being run in an inviscid mode (EE mode) and several such calculations were made. Below M = 0.84 the aileron exhibited damped oscillations of about k = 0.36 whereas divergent oscillations (k = 0.39) were calculated at M = 0.84. Hence the tendency to oscillate at a given frequency derives from the inviscid flow equations while the viscosity apparently plays the key role of limiting the amplitude of oscillation. These calculations were performed on a 76 x 42 grid and required approximately 1.5 sec of CDC 7600 computer time per time step or 460 μs. per grid point per iteration. Nondimensional time steps of 0.005 - 0.01 were used (based on chord).

Chyu and his coworkers[26,27] used this same method along with the grid interpolation method described above to study the moderate shock case[26] and the shock-induced separation case[27] for pitching oscillations of the NACA 64A010A airfoil shown in figs. 83 and 84. Comparison of the interactive viscous-TSD (IV-TSD) results of fig. 35 with the Navier-Stokes results of fig. 83 is instructive. The two sets of calculations are in very good agreement for this type I flow condition. As for the type II - III flow condition shown in fig. 84, note that the full and thin-layer Navier-Stokes results show no significant differences except near the shock where the difference is not large. Thus the thin-layer Navier-Stokes equation appear to be viable for this class of unsteady flow problem. These calculations were obtained on a 139 x 49 C-grid using 2620 steps per cycle of oscillation and the time per step on the CRAY X-MP computer was: full NS, 0.33 sec; TL-NS, 0.17 sec; EE, 0.17 sec, corresponding to 25 - 44 μsec. per grid point per time step.

Rumsey and Anderson[78] describe an extension of the flux-vector split, approximate factorization upwind scheme described in eqs. (96) - (98) to the 2-D thin-layer Navier-Stokes equations. This method is developed for body conforming moving grid systems and is given in eqs. (1) - (13). Figure 85 gives their solution for the oscillating NACA 0012 airfoil at M = 0.6 and k = 0.081. This case has already been presented for IV-TSD calculations in fig. 38(c) and for EE calculations in fig. 78. Figure 85 shows the effect of grid refinement indicating little change in going from a 129 x 29 grid to a 257 x 97 grid. The EE and TL-NS solutions appear to be quite similar while the TSD solution shows some differences for this high lift case. This computational algorithm is highly vectorized for use on either the CDC CYBER

205 or the CRAY 2 computers. Computational speed averages approximately 16 μsec per grid point per time step and the memory required in kilowords is about 0.200 x (meshsize).

Periodic Aerodynamic Oscillations

In the previous sections, algorithms and experimental results directed at moving or oscillating lifting surfaces have been presented. There is an important class of experimentally observed unsteady flows wherein periodic flow is observed over very narrow ranges of test conditions for perfectly rigid bodies. These flows tend to be found in transition regions between attached and separated flow conditons and are recognized as highly sensitive data which may be used for the validation of computational methods[1].

In order to provide experimental data for validation of viscous flow CFD computer codes, McDevitt et al.[43] conducted tests on a rigid 18 percent thick circular arc airfoil. Figure 86 illustrates the parameters of the experiment which was designed to encounter both trailing-edge and shock-induced separations at high Reynolds numbers within the wind tunnel operating limits. Over a narrow range of Mach number, $0.73 < M < 0.78$, oscillatory flow separation was observed, fig. 87[45]. McDevitt[44] states that the oscillations involve predominantly type C shock motion with small regions of type A motion near the onset of the periodic oscillations, fig. 88. The reduced frequency of the oscillations is $k \approx 0.48$ for $\alpha = 0°$ and varies little with angle-of-attack.

Levy[45] successfully computed such oscillations for this airfol using a Navier-Stokes flow solver. Levy's code was a modification of the code of ref. 148 and used MacCormack's explicit solution scheme with an algebraic eddy viscosity model. Levy modified the code to simulate the contoured wind tunnel walls. Figure 89 shows steady computed Mach contours for Mach numbers of 0.72 and 0.78, corresponding to trailing-edge and shock-induced separations, respectively, and unsteady flow with oscillatory trailing-edge/shock-induced separation for $M = 0.754$. The reduced frequency of the computed oscillations is 0.40, about 20 percent lower than the measured frequency. Note particularly the lower surface Mach contours of the third frame for $M = 0.754$. The few lines indicate the collapse of the supersonic region for this portion of the cycle. Also note the dimpled nature of these Mach lines under the airfoil surface. These features will be discussed in more detail below.

Subsequent tests on circular arc airfoils of thicknesses from 10 to 20 percent were performed by Mabey[46], obtaining similar periodic oscillations. The Mach number range of the oscillations increases with decreasing thickness as does the oscillation frequency, remaining in

the range of $0.4 < k < 0.55$ depending on thickness and wind tunnel wall condition. Mabey et al.[47] and Levy[48] give detailed comparisons of Navier-Stokes calculations with experiment for a 14 percent thick airfoil, reproducing qualitatively the details of the oscillatory flow.

These unsteady periodic flows encountered over limited ranges of Mach number and triggered by oscillating trailing-edge/shock-induced boundary layer separation are just recently coming within the range of computational methods. The weakest link for this capability is the uncertainty in the turbulence modeling of complex separated flows, since rapid progress continues to be made in the development of improved algorithms and faster computers.

It is well known that separated flows depart strongly from equilibrium - type behavior, so that at a minimum some account of the non-equilibrium "upstream history" effects should be included in the computations. Some encouraging results along this line have been obtained by LeBalleur[149] with an integral boundary layer model and Johnson[150] with an eddy-viscosity Reynolds-shear stress closure model. Simpson[151] recently reviewed calculation methods for turbulent separated flows and Coakley[152] compared several methods for airfoil applications.

On the other hand, Levy[45] was able to reproduce the unsteady periodic flow behavior of the 18 percent circular-arc airfoil using an equilibrium two-layer algebraic model. The steady flow at Mach numbers below the range of periodic flow, characterized by trailing-edge separation, was predicted accurately. Levy demonstrated that the influence of the channel walls had a substantial impact on the comparisons with experiment, especially at Mach numbers away from the design point. This effect was not considered in the earlier comparisons of Deiwert[148] with the experimental results. The steady flow at a Mach number above the range of periodic flow, characterized by shock-induced separation, was not accurately predicted, as the calculation demonstrated a normal shock pattern (fig. 89) with trailing-edge pressure recovery, whereas the experiment indicated an oblique shock pattern and a constant pressure region downstream of the shock.

In addition to Levy's calculations, the unsteady periodic behavior for the 18-percent biconvex airfoil has also been computed by Steger[153] and by LeBalleur[149]. Steger's calculation was for an airfoil in free-air with an implicit Navier-Stokes code using the Baldwin-Lomax algebraic model. The unsteady flow occurred at a higher Mach number ($M = 0.783$) than that of Levy ($M = 0.754$), which can partly be attributed to the free-air boundary conditions. The computed reduced frequency (0.41) was remarkably close to that of Levy (0.40) although both are low in comparison to experiment (0.48). LeBalleur's recent calculations were also made in free-air with a small disturbance potential method including an interacted two-equation

integral viscous model. Steady shock-induced separation was computed at M = 0.788 and unsteady periodic flow at M = 0.76. The reduced frequency (0.34) was lower than either of the two Navier-Stokes solutions.

Some calculations have been made using the implicit upwind-biased Navier-Stokes algorithm described in ref. 154 using an algebraic turbulence model. The tunnel walls were modeled and boundary conditons appropriate for internal flow were used, i.e., the downstream pressure and upstream enthalpy, entropy, and flow direction were specified. The results indicated unsteady flow at a higher Mach number than Levy; steady trailing-edge separation occurred at M = 0.754 and unsteady periodic flow at M = 0.78, although the Mach number for onset of the unsteadiness was sensitive to whether or not the divergence of the tunnel boundary to account for boundary layer growth was included. Figure 90 shows Mach contours through one half-cycle of oscillation (near maximum lift to minimum lift) indicating the forward movement, disappearance, and subsequent formation near the trailing edge of the lower surface shock. The reduced frequency of the type B unsteady motion was 0.406, in close agreement with the calculations of both Levy (compare fig. 89) and Steger. The implicit calculations were made with a time step of 0.01 and a computational time of 18 μs. per grid point per time step on the CYBER 205 computer.

The calculation of the unsteady periodic flow boundaries for airfoils is a fruitful area for the development and validation of computational methods. Experimental pressure data[43-47] over a wide range of Reynolds number is available, although detailed boundary-layer measurements are not. For the 18-percent biconvex experiments of McDevitt, a substantial hysteresis effect in the unsteady flow boundary was found. This aspect has not been demonstrated with computational methods as yet, but it would be expected, based on the above discussion, that computational modeling as close as possible to that of the experimental conditions will be a critical consideration. The most interesting behavior, and the most challenging from the computational viewpoint, occurs in the transitional region from laminar to turbulent flow. In the experiment of McDevitt[43], the Mach number range for the observed unsteady flow diminished near a Reynolds number of 3×10^6 (fig. 87) and in the experiments of Mabey[47], it disappeared completely in the range of Reynolds number from about 3×20^6 to 5×10^6. Scale effects in either experiment were not significant once turbulent flow is fully established ahead of the shock.

The frequency of these oscillations is of interest in that the flow mechanism causing the unsteadiness might be identified via the characteristic time constants of signal propagation

within the various flow regions. Tijdeman[3] noted an almost linear relation between the phase lag of the shock motion and the airfoil motion for type A shock motion with a well-developed shock (for pitch oscillations of the NLR 7301 airfoil). He related this to the signal propagation time from the trailing-edge to the shock. Mabey[47], commenting on characteristic time constants for the 14 percent circular arc airfoil periodic oscillations, notes that this reasoning leads to reduced frequency parameters of 1.15 to 1.8, much higher than the observed frequencies.

Three items mentioned above germane to this discussion are; Steger and Bailey's[25] inviscid EE calculations for the aileron buzz case, LeBalleur and Gerodrous-Lavigne's[149] interacted viscous-TSD code result for periodic oscillations, and Batina's[108] demonstration of the possibility of aerodynamic resonance with an inviscid TSD code. The occurrence of damped and undamped oscillations observed for inviscid flows at nearly the same frequency as the oscillations in viscous flow[25] ($k \approx 0.36$-0.39) implies that the flow mechanism determining the oscillation frequency derives from the dynamics of the inviscid flow region. Furthermore, the results of Refs. 108 and 149 give impetus to studying this effect with a TSD code. Accordingly, calculations were made with the XTRAN2L code of the aerodynamic response for the 18 percent thick circular arc airfoil due to trailing-edge 25 percent chord flap motions. The nonisentropic modifications described in eqs. (70) - (77) were used to obtain solutions for this strong-shock case. Figure 91 presents the resulting c_{m_δ} frequency response function for Mach numbers of 0.66-0.74. There is a very marked development of an aerodynaic resonance effect as Mach number increases. For $M = 0.74$ the airfoil resonance frequency is $k = 0.32$, very cose to the computational conditions of ref. 149 for periodic oscillations ($M = 0.76$ and $k = 0.36$).

CONCLUDING REMARKS

These lectures have summarized the status of computational unsteady aerodynamic for lifting surfaces. The fluid dynamic flow models appropriate to the several levels of physical models available have been presented along with details of solution algorithms. The subject has been differentiated with respect to the difficulty of flow modeling and computational requirements by distinguishing unsteady flow types as: I, attached flow; II, mixed attached and separated flow; and III, separated flow.

For type I flows, computational methods have matured with a steady progression of improved

techniques for flow simulation. Significant efforts have been devoted to understanding the effects of equational level, computational grid, boundary conditions, and interactive viscous modeling. Extensive comparisons with experimental data sets have been made with small disturbance potential (both linear and transonic), potential, Euler and Navier-Stokes equation solvers for two-dimensional airfoil cases and an understanding of the range of validity of the various methods can be made. Less extensive comparisons are available for wings and even fewer comparisons for complex configurations involving interference effects. Experimental unsteady data is needed for such configurations in order to validate computational methods which can now treat complete aircraft for transonic flow conditions.

Progress in solution algorithms for unsteady aerodynamic has been significant with large decreases in required computer resources due to larger time steps allowed by more stable solution algorithms. The treatment of body conforming grids for deforming aeroelastic vehicles needs further attention to fully utilize the computational methods available.

Computational aeroelastic analysis has demonstrated capability for prediction of complete transonic flutter boundaries for wings, including significant "transonic dip" features. Many more transonic flutter calculations will be needed to fully validate computational methods for transonic flutter predictions as critical features of these stability boundaries frequently involve difficult flow conditions, such as type II mixed flow.

REFERENCES

[1]Edwards, J. W.; and Thomas, J. L.: "Computational Methods for Unsteady Transonic Flows." AIAA Paper No. 87-0107, presented at the AIAA 25th Aerospace Sciences Meeting, Reno, Nevada, January 12-15, 1987.

[2]Anon: "Military Specification; Airplane Strength and Rigidity; Flutter, Divergence, and Other Aeroelastic Instabilities." MIL-A-008870A (USAF), March 1971.

[3]Tijdeman, H.: "Investigations of the Transonic Flow Around Oscillating Airfoils." National Aerospace Laboratory NLR, The Netherlands, NLR TR 77090U, 1978.

[4]Pearcy, H. H.; Haines, A. B.; and Osborne, J.: "The Interaction Between Local Effects at the Shock and Real Separation." In AGARD CP No. 35, Transonic Aerodynamics, 1968.

[5]Bradley, R. G.: "Prcatical Aerodynamic Problems - Military Aircraft." In Transonic Aerodynamics, ed by Nixon, D., Vol. 81, Progress in Astronautics and Aeronautics, AIAA, 1982.

[6]Farmer, M. G.; Hanson, P. W.; and Wynne, E. C.: "Comparison of Supercritical and Conventional Wing Flutter Characteristics." NASA TM X-72837, May 1976.

[7]Erickson, L. L.: "Transonic Single-Mode Flutter and Buffet of a Low Aspect Ratio Wing Having a Subsonic Airfoil Shape." NASA TN D-7346, January 1974.

[8]Houwink, R.; Kraan, A. N.; and Zwaan, R. J.: "A Wind-Tunnel Study of the Flutter Characteristics of a Supercritical Wing." Journal of Aircraft, Vol. 19, May 1982, pp. 400-405.

[9]Persoon, A. J.; Horsten, J. J.; and Meijer, J. J.: "On Measuring Transonic Dips in the Flutter Boundaries of a Supercritical Wing in the Wind Tunnel." AIAA Paper No. 83-1031-CP, May 1983. Also NLR MP 83008 U, January 1983.

[10]Moss, G. F.; and Pierce, D.: "The Dynamic Response of Wings in Torsion at High Subsonic Speeds." In AGARD CP-226, 1977.

[11]Seidel, D. A.; Eckstrom, C. V.; and Sandford, M. C.: "Investigation of Transonic Region of High Dynamic Response Encountered on an Elastic Supercritical Wing." AIAA Paper No. 87-0735-CP, Presented at the AIAA/ASME/ASCE/AHS 28th Structures, Structural Dynamics, and Materials Conference, Monterey, California, April 6-8, 1987. Also NASA TM 89121, March 1987.

[12]Dobbs, S. K.; Miller, G. D.; and Stevenson, J. R.: "Self Induced Oscillation Wind Tunnel Test of a Variable Sweep Wing." AIAA Paper No. 85-0739-CP, presented at the AIAA/ASME/ASCE/AHS 26th Structures, Structural Dynamics, and Materials Conference, Orlando, Florida, April 1985.

[13]Magnus, R.; and Yoshihara, H.: "The Transonic Oscillating Flap." AIAA Paper No. 76-327, presented at the AIAA 9th Fluid and Plasma Dynamics Conference, San Diego, California, July 14-16, 1976.

[14]Ballhaus, W. F.; and Goorjian, P. M.: "Implicit Finite-Difference Computations of Unsteady Transonic Flows about Airfoils." AIAA Journal, Vol. 15, No. 12, December 1977.

[15]Ballhaus, W. F.: "Some Recent Progress in Transonic Flow Computations." VKI Lecture Series: Computational Fluid Dynamics, von Karman Institute for Fluid Dynamics, Rhode-St-Genese, Belgium, March 1976.

[16]Bland, S. R.: "AGARD Two-Dimensional Aeroelastic Configurations." AGARD-AR-156, 1979.

[17]Bland, S. R.: "AGARD Three-Dimensional Aeroelastic Configurations." AGARD-AR-167, 1982.

[18]Lambourne, N. C.: "Compendium of Unsteady Aerodynamic Measurements." AGARD Report

No. 702, 1982.

[19]Dau, K.; Vogel, S.; and Zimmerman H.: "Compendium of Unsteady Aerodynamic Measurements Addendum No. 1." AGARD Report No. 702, 1985.

[20]Mabey, D. G.; Welsh, B. L.; and Pyne, C. R.: "Measurements of Steady and Oscillatory Pressure on a Rectangular Wing." RAE TR 86040, July 1986.

[21]Sandford, M. C.; Ricketts, R. H.; and Hess, R. W.: "Recent Transonic Unsteady Pressure Measurements at the NASA Langley Research Center." Paper No. 85-23, presented at the Second International Symposium on Aeroelasticity and Structural Dynamics, Aachen, Germany, April 1 3, 1985.

[22]Tijdeman, H. et al.: "Transonic Wind Tunnel Tests on an Oscillating Wing with External Stores." AFFDL-TR-78-194, Pts. 1-IV, December 1978.

[23]Magnus, R. J.: "Calculations of Some Unsteady Transonic Flows about the NACA 64A006 and 64A010 Airfoils." Technical Report AFFDL-TR-77-46, July 1977.

[24]Magnus, R. J.: "Some Numerical Solutions of Inviscid, Unsteady Transonic Flows Over the NLR 7301 Airfoil." CASD/LVP 78-013, Convair Division of General Dynamics, San Diego, California, January 1978.

[25]Steger, J. L.; and Bailey, H. E.: "Calculation of Transonic Aileron Buzz." AIAA Journal, Vol. 18, No. 3, March 1980.

[26]Chyu, W. J.; Davis, S. S.; and Chang, K. S.: "Calculation of Unsteady Transonic Flow Over an Airfoil." AIAA Journal, Vol. 19, No. 6, June 1981.

[27]Chyu, W. J.; and Davis, S. S.: "Numerical Studies of Unsteady Transonic Flow Over an Oscillating Airfoil." In AGARD CP-374, "Transonic Unsteady Aerodynamics and its Aeroelastic Application," January 1985.

[28]Borland, C. J.; and Rizzetta, D. P.; and Yoshihara, H.: "Numerical Solution of Three-Dimensional Unsteady Transonic Flow Over Swept Wings." AIAA Journal, Vol. 20, No. 3, March 1982.

[29]Borland, C. J.; and Rizzetta, D. P.: "Nonlinear Transonic Flutter Analysis." AIAA Journal, Vol. 20, No. 11, November 1982.

[30]Laurent, A.: "Calcul D'Ecoulement Transsonique Instationnaire Authour D'Aile A Forte Fleche." In AGARD CP-374, "Transonic Unsteady Aerodynamics and its Aeroelastic Application," January 1985.

[31]Batina, J. T.: "An Efficient Algorithm for Solution of the Unsteady Transonic Small-

Disturbance Equation." AIAA Paper No. 87-0109, Reno, Nevada, January 1987.

[32]Malone, J. B.; Sankar, L. N.; and Sotomayer, W. A.: "Unsteady Aerodynamic Modeling of a Fighter Wing in Transonic Flow." Journal of Aircraft, Vol. 23, No. 8, August 1986.

[33]Shankar, V.; and Ide, H.: "Treatment of Steady and Unsteady Flows Using a Fast, Time-Accurate Full Potential Scheme." AIAA Paper No. 85-4060, Colorado Springs, Colorado, October 1985.

[34]Isogai, K.: "The Development of Unsteady Transonic 3-D Full Potential Code and Its Aeroelastic Applications." In AGARD CP-374, "Transonic Unsteady Aerodynamics and its Aeroelastic Application," January 1985.

[35]Mulak, P.; and Angelini, J.: "Amelioration et Extension D'Une Methode De Calcul D'Ecoulements Transsoniques Tridimensionnels." In AGARD CP-374, "Transonic Unsteady Aerodynamics and its Aeroelastic Application," January 1985.

[36]Belk, D. M.; Janus, J. M.; and Whitfield, D. L.: "Three-Dimensional Unsteady Euler Equations Solutions on Dynamic Grids." AIAA Paper No. 85-1704, July 1985.

[37]Janus, J. M.; "The Development of a Three-Dimensional Split Flux Vector Euler Solver with Dynamic Grid Applications." M. S. Thesis, Mississippi State, Mississippi, August 1984.

[38]Sides, J.: "Computation of Unsteady Transonic Flows with an Implicit Numerical Method for Solving the Euler Equations." Rech. Aerosp. 1985-2.

[39]Jameson, A.; and Venkatakrishnan, V.: "Transonic Flows About Oscillating Airfoils Using the Euler Equations." AIAA Paper No. 85-1514, AIAA 7th Computational Fluid Dynamics Conference, 1985.

[40]Smith, G. E.; Whitlow, W., Jr.; and Hassan, H. A.: "Unsteady Transonic Flows Past Airfoils Using the Euler Equations." AIAA Paper No. 86-1764-CP, San Diego, California, June 9-11, 1986.

[41]Salmond, D. J.: "Calculation of Harmonic Aerodynamic Forces on Aerofoils and Wings from the Euler Equations." In AGARD CP-374, "Transonic Unsteady Aerodynamics and its Aeroelastic Application," January 1985.

[42]Belk, D. M.: "Unsteady Three-Dimensional Euler Equations Solutions on Dynamic Blocked Grids." Ph.D. dissertation, Mississippi State University, August 1986.

[43]McDevitt, J. B.; Levy, L., Jr.; and Deiwert, G. D.: "Transonic Flows about a Thick Circular-Arc Airfoil." AIAA Journal, Vol. 14, No. 5, May 1976.

[44]McDevitt, J. B.: "Supercritical Flow About a Thick Circular-Arc Airfoil." NASA TM

78549, January 1979.

[45]Levy, L. L., Jr.: "Experimental and Computational Steady and Unsteady Transonic Flows about a Thick Airfoil." AIAA Journal, Vol. 16, No. 6, June 1978.

[46]Mabey, D. G.: "Oscillatory Flows from Shock-Induced Separations on Biconvex Aerofoils of Varying Thickness in Ventilated Wind Tunnels." AGARD CP 296, 1980.

[47]Mabey, D. G.; Welsh, B. L.; and Cripps, B. E.: "Periodic Flows on a Rigid 14% Thick Biconvex Wing at Transonic Speeds." RAE Technical Report 81059, May 1981.

[48]Levy, L. L., Jr.: "Predicted and Experimental Steady and Unsteady Transonic Flows About a Biconvex Airfoil." NASA TM 81262, February 1981.

[49]Mabey, D. G.; Ashill, P. R.; and Welsh, B. L.: "Aeroelastic Oscillations Caused by Transitional Boundary Layers and Their Attenuation." AIAA Paper No. 86-0736, West Palm Beach, Florida, March 1986.

[50]Osswald, G. A.; Ghia, K. N.; and Ghia, U.: "An Implicit Time-Marching Method for Studying Unsteady Flow with Massive Separation." AIAA Paper No. 85-1489, AIAA 7th Computational Fluid Dynamics Conference, 1985.

[51]Leconite, Y.; and Piquet, J.: "Unsteady Viscous Flow Round Moving Circular Cylinders and Airfoils." AIAA Paper No. 85-1490, AIAA 7th Computational Fluid Dynamics Conference, 1985.

[52]Anderson, W. K.; Thomas, J. L.; and Rumsey, C. L.: "Application of Thin layer Navier-Stokes Equations Near Maximum Lift." AIAA Paper No. 84-0049, presented at the AIAA 22nd Aerospace Sciences Meeting, Reno, Nevada, January 1984.

[53]Anon: "Unsteady Aerodynamics." AGARD-CP-227, 1978.

[54]Anon: "Boundary Layer Effects on Unsteady Airloads." AGARD-CP-296, 1981.

[55]Anon: "Transonic Unsteady Aerodynamics and its Aeroelastic Applications." AGARD-CP-374, 1985.

[56]Anon: "Unsteady Aerodynamics-Fundamentals and Applications to Aircraft Dynamics." AGARD-CP-386, 1985.

[57]Peterson, V. L.: "Trends in Computational Capabilities for Fluid Dynamics." In AGARD CP-375, "Transonic Unsteady Aerodynamics and its Aeroelastic Application," January 1985.

[58]McCroskey, W. J.; Kutler, P.; and Bridgeman, J. O.: "Status and Prospects of Computational Fluid Dynamics for Unsteady Transonic Viscous Flows." In AGARD CP-374,

"Transonic Unsteady Aerodynamics and its Aeroelastic Application," January 1985.

[59]Mykytow, W. J.: "Transonic Unsteady Aerodynamics and its Aeroelastic Applications." In AGARD CP-386, "Unsteady Aerodynamics - Fundamentals and Applications to Aircraft Dynamics," November 1985.

[60]Mabey, D. G.; and Chambers, J. R.: "Unsteady Aerodynamics - Fundamentals and Applications to Aircraft Dynamics." AGARD-AR-222, May 1985.

[61]Zwaan, R. J.: "Aeroelastic Problems of Wings in Transonic Flow." Presented at VKI Lecture Series "Unsteady Airloads and Aeroelastic Problems in Separated and Transonic Flow," Rhode-Saint-Genese, Belgium, March 1981. (Also NLR MP 81005 U).

[62]Deiwert, G. S.: "Finite Difference Simulation of Unsteady Interactive Flows." In Computational Methods in Viscous Flow, ed. by Habashi, W. G.; Pineridge Press, 1984.

[63]Mabey, D. G.: "A review of Some Recent Research on Time-Dependent Aerodynamics." The Aeronautical Journal of The Royal Aeronautical Society, February 1984.

[64]Mabey, D. G.; Welsh, B. L.; and Cripps, B. E.: "Measurements of Steady and Oscillatory Pressures on a Low Aspect Ratio Model at Supersonic and Supersonic Speeds," RAE TR 84095, September 1984.

[65]Davis, S. D.; and Malcolm, G. N.: "Transonic Shock-Wave/Boundary-Layer.Interactions on an Oscillating Airfoil." AIAA Journal, Vol. 18, No. 11, November 1980.

[66]McDeivtt, J. B.; and Okuno, A. F.: "Static and Dynamic Pressure Measurements on a NACA 0012 Airfoil in the Ames High Reynolds Number Facility." NASA Technical Paper 2485, June 1985.

[67]Zimmerman, H.: "The Application of Transonic Unsteady Methods for Calculation of Flutter Airloads." In AGARD CP-374 "Transonic Unsteady Aerodynamics and its Aeroelastic Application," January 1985.

[68]den Boer, R. G.; and Houwink, R.: "Analysis of Transonic Aerodynamic Characteristics for a Supercritical Airfoil Oscillating in Heave, Pitch and With Oscillating Flap." In AGARD CP-374, "Transonic Unsteady Aerodynamics and its Aeroelastic Application," January 1985.

[69]Le Balleur, J. C.; and Girodroux-Lavigne, P.: "Prediction of Buffeting and Calculation of Unsteady Boundary Layer Separation Over Airfoils." Presented at IUTAM Symposium on "Boundary Layer Separation, London, University College, August 1986.

[70]Hess, R. W.; Seidel, D. A.; Igoe, W. B.; and Lawing, P. L.: "Highlights of Unsteady Pressure Tests on a 15 Percent Supercritical Airfoil at High Reynolds Number, Transonic Condition."

AIAA Paper No. 87-0035, Reno, Nevada, January 12-15, 1987.

[71]Sandford, M. C.; Ricketts, R. H.; and Hess, R. W.: "Recent Transonic Unsteady Pressure Measurements at the NASA Langley Research Center." Paper No. 85-23, Second INternational Symposium on Aeroelasticity and Structural Dynamics, Aachen, Germany, April 1-3, 1985.

[72]Ricketts, R. H.; Sandford, M. C.; Watson, J. J.; and Seidel, D. A.: "Subsonic and Transonic Unsteady- and Steady-Pressure Measurements on a Rectangular Supercritical Wing Oscillated in Pitch." NASA TM 85765, August 1984.

[74]Isogai, K.; and Suetsugu, K.: "Numerical Simulation of Transonic Flutter of a Supercritical Wing." NAL Report TR-726T, August 1982.

[75]Bennett, R. M.; Seidel, D. A.; and Sandford, M. C.: "Transonic Calculations for a Flexible Supercritical Wing and Comparison with Experiment." AIAA Paper No. 85-0665-CP, Orlando, Florida, Apri. 15-17, 1985.

[76]Seidel, D. A.; Sandford, M. C.; and Eckstrom, C. V.: "Measured Unsteady Transonic Aerodynamic Characteristics of an Elastic Supercritical Wing with an Oscillating Control Surface." AIAA Paper No. 85-0598-CP, Orlando, Florida, April 15-17, 1985.

[77]Guruswamy, P.; and Goorjian, P. M.; and Tu, E. L.: "Transonic Aeroelasticity of Wings With Tip Stores." AIAA Paper No. 86-1007-CP, San Antonio, Texas, May 19-21, 1986.

[78]Rumsey, C. L.; and Anderson, W. K.: "Some Numerical and Physical Aspects of Unsteady Navier-Stokes Computations Over Airfoils Using Dynamic Meshes." AIAA Paper No. 88-0329, presented at the AIAA 26th Aerospace Sciences Meeting, Reno, Nevada, January 1988.

[79]Baldwin, B.; and Lomax, H.: "Thin Layer Approximation and Algebraic Model for Separated Turbulent Flows." AIAA Paper 78-257, 1978.

[80]Anderson, D. A.; Tannehill, J. C.; and Pletcher, R. H.: "Computational Fluid Mechanics and Heat Transfer." Hemisphere Publishing Corporation, 1984.

[81]Anderson, W. K.; Thomas, J. L.; and Rumsey, C. L.: "Extension and Applications of Flux-Vector Splitting to Unsteady Calculations on Dynamic Meshes." AIAA Paper 87-1152-CP, presented at the AIAA 8th Computational Fluid Dynaics Conference, Honolulu, Hawaii, June 1987.

[82]Whitlow, Woodrow, Jr.; Hafez, M. M.; and Osher, S. J.: "An Entropy Correction Method for Unsteady Full Potential Flows with Strong Shocks." Journal of Fluid and Structures, November 1987.

[83]Liepmann, H. W.; and Roshko, A.: "Elements of Gasdynamics." John Wiley & Sons, Inc.,

1957.

[84]Batina, J. T.: "An Efficient Algorithm for Solution of the Unsteady Transonic Small-Disturbance Equation." AIAA Paper No. 87-0109, Presented at the AIAA 25th Aerospace Sciences Meeting, Reno, Nevada, January 12-15, 1987. Also NASA TM 89014, December 1986.

[85]Batina, J. T.; Seidel, D. A.; Bland, S. R.; and Bennett, R. M.: "Unsteady Transonic Flow Calculations for Realistic Aircraft Configurations." AIAA Paper No. 87-0850-CP, Presented at the AIAA/ASME/ASCE/AHS, 28th Structures, Structural Dynamics and Materials Conference, Monterey, California, Ajpril 6-8, 1987. Also NASA TM-89120, March 1987.

[86]Whitlow, Woodrow, Jr.: "XTRAN2L: A Program for Solving the General-Frequency Unsteady Transonic Small Disturbance Equation." NASA TM 85723, November 1983.

[87]Thomas, J. and Salas, M., "Far-Field Boundary Conditions for Transonic Lifting Solutions to the Euler Equations," AIAA Paper No. 85-0020, 1985.

[88]Bisplinghoff, Raymond L.; Ashley, Hlt; and Halfman, Robert L.: "Aeroelasticity." Addison-Wesley Publishing Co., 1955.

[89]Theodorsen, Theodore: General Theory of Aerodynamic Instability and the Mechanism of Flutter. NACA Rept. 496, 1935.

[90]Garrick, I. E.; and ?Rubinow, S. I.: Flutter and Oscillating Air-Force Calculations for an Airfoil in Two-Dimensional Supersonic Flow. NACA Rept. 846, 1949.

[91]Watkins, C. E.; Woolston, D. S.; and Cunningham, H. J.: "A Systematic Kernel Function Procedure for Determining Aerodynamic Forces on Oscillating or Steady Finite Wings at Subsonic Speeds." NASA TR R-48, 1959.

[92]Watkins, C. E.; Runyan, H. L.; and Woolston, D. S.: "On the Kernel Function of the Integral Equation Relating the Lift and Downwash Distributions of Oscillating Finite Wings in Subsonic Flows." NACA Report 1234, 1955.

[93]Ashley, Holt: "Some Considerations Relative to the Prediction of Unsteady Air Loads on Lifting Configurations." Journal of Aircraft, vol. 8, no. 10, October 1971.

[94]Rowe, W. S.; Redman, M. C.; Ehlers, F. E.; and Sebastian, J. D.: "Prediction of Unsteady Aerodynamic Loadings Caused by Leading Edge and Trailing Edge Control Surface Motions in Subsonic Compressible Flow Analysis and Results." NASA CR-2543, 1975.

[95]Albano, E.; and Rodden, W. P.: "A Doublet-Lattice Method for Calculating Llft Distributions on Oscillating Surfaces in Subsonic Flows." AIAA Journal, vol. 7, no. 2, February 1969.

[96]Rowe, W. S.; and Cunningham, H. J.: "On the Convergence of Unsteady Generalized Aerodynamic Forces." Journal of Aircraft, vol. 21, no. 6, June 1984, pp. 420-427.

[97]Lomax, H.; Heaslet, M. A.; Fuller, F. B.; and Sluder, L.: "Two- and Three-Dimensional Unsteady Lift Problems in High-Speed Flight." NACA Report 1077, 1952.

[98]Edwards 79

[99]Edwards, John William: "Unsteady Aerodynamic Modeling and Active Aeroelastic Control. SUDAAR 504, Stanford University, February 1977.

[100]Whitlow, Woodrow, Jr.: "Computational Unsteady Aerodynamics for Aeroelastic Analysis." NASA TM 100523, December 1987.

[101]Whitlow, W., Jr.: "XTRAN2L: A Program for Solving the General-Frequency Unsteady Transonic Small Disturbance Equation." NASA TM 85723, November 1983.

[102]Houwink, R.; and van der Vooren, J.: "Improved Version of LTRAN2 for Unsteady Transonic Flow Computations." AIAA Journal, Vol. 18, August 1980.

[103]Rizzetta, D. P.; and Chin, W. C.: "Effect of Frequency in Unsteady Transonic Flows." AIAA Journal, Vol. 12, No. 7, July 1979.

[104]Seidel, D. A.; and Batina, J. T.: "User's Manual for XTRAN2L (Version 1.2): A Program for Solving the General Frequency Unsteady Transonic Small-Disturbance Equation." NASA TM 87737, July 1986.

[105]Goorjian, P. M.; Meagher, M. E.; and Van Buskirk, R. V.: "Monotone Implicit Algorithms for the Small-Disturbance and Full Potential Equations Applied to Transonic Flows." AIAA Paper No. 83-0371, Presented at the AIAA 21st Aerospace Sciences Meeting, Reno, Nevada, January 10-13, 1983.

[106]Engquist, B. E.; and Osher, S. J.: "Stable and Entropy Satisfying Approximations for Transonic Flow Calculations." Journal of Aircraft, Vol. 34, No. 149, January 1980.

[107]Seidel, D. A.; Bennett, R. M.; and Whitlow, W., Jr.: "An Exploratory Study of Finite Difference Grids for Transonic Unsteady Aerodynamics. AIAA Paper No. 83-0503, Presented at the AIAA 21st Aerospace Sciences Meeting, Reno, Nevada, January 10-13, 1983. Also NASA TM 84583.

[108]Batina, J. T.: "Effects of Airfoil Shape, Thickness, Camber, and Angle of Attack on Calculated Transonic Unsteady Airloads. NASA TM-86320, February 1985.

[109]Seidel, D. A.; Bennett, R. M.; and Ricketts, R. H.: "Some Recent Applications of XTRAN3S."

AIAA Paper No. 83-1811, Danvers, Mass., July 1983.

[110]Howlett, J. T.; and Bland, S. R.: "Calculation of Viscous Effects on Transonic Flow for Oscillating Airfols and Comparisons with Experiment." NASA TP-2731, September 1987.

[111]Green, J. E.; Weeks, D. J.; and Brooman, J. W. F.: Prediction of Turbulent Boundary Layers and Wakes in Compressible Flow by a Lag-Entrainment Method. R & M No. 3791, British Aeronautical Research Council, 1977.

[112]Rizzetta, D. P.: "Procedures for the Computation of Unsteady Transonic Flows Including Viscous Effects." NASA CR 166249, January 1982.

[113]Edwards, J. W.; Bland, S. R.; and Seidel, D. A.: "Experience with Transonic Unsteady 0 Aerodynamic Calculations." In AGARD CP-374, "Transonic Unsteady Aerodynamics and its Aeroelastic Application," January 1985.

[114]Bland, S. R.; and Edwards, J. W.: "Airfoil Shape and Thickness Effects on Transonic Airloads and Flutter." Journal of Aircraft, Vol. 21, No. 3, March 1984.

[115]Edwards, J. W.; Bennett, R. M.; Whitlow, W., Jr.; and Seidel, D. A.: "Time-Marching Transonic Flutter Solutions Including Angle-of-Attack Effects." Journal of Aircraft, Vol. 20, No. 11, November 1983.

[116]Salas, M. D.; and Gumbert, C. R.: "Breakdown of the Conservative Potential Equation." AIAA Paper No. 85-0367, Presented at the AIAA 23rd Aerospace Sciences Meeting, Reno, Nevada, January 14-17, 1985.

[117]Steinhoff, J.; and Jameson, A.: "Multiple Solutions of the Transonic Potential Flow Equation." AIAA Journal, Vol. 20, No. 11, November 1982.

[118]Williams, M. H.; Bland, S. R.; and Edwards, J. W.: "Flow Instabilities in Transonic Small-Disturbance Theory." AIAA Journal, Vol. 23, No. 10, October 1985.

[119]Fuglsang, D. F.; and Williams, M. H.: "Non-Isentropic Unsteady Transonic Small Disturbance Theory." AIAA Paper No. 85-0600, Orlando, Florida, April 1985.

[120]Bennett, R. M.; Wynne, E. C.; and Mabey, D. G.: "Calculation of Transonic Steady and Oscillatory Pressures on a Low Aspect Ratio Model." Journal of Aircraft, Vol. 24, No. 6, June 1987, pp. 392-398.

[121]Guruswamy, G. P.; and Goorjian, P. M.: "Efficient Algorithm for Unsteady Transonic Aerodynaics of Low-Aspect-Ratio Wings." Journal of Aircraft, Vol. 22, No. 3, March 1985.

[122]Gibbons, M. D.; Whitlow, W., Jr.; and Williams, M. H.: "Nonisentropic Unsteady Three Dimensional Small Disturbance Potential Theory." AIAA Paper 86-0863, San Antonio, TX, May

1986.

[123]Batina, J. T.: "Unsteady Transonic Flow Calculations for Interfering Lifting Surface Configurations." Journal of Aircraft, Vol. 23, May 1986, pp. 422-430.

[124]Batina, J. T.: "Unsteady Transonic Flow Calculations for Wing-Fuselage Configurations." Journal of Aircraft, Vol. 23, December 1986, pp. 897-903.

[125]Shankar, V.; Ide, H.; Gorski, J.; and Osher, S.: A Fast Fime-Accurate Unsteady Full-Potential Scheme," AIAA Paper No. 85-1512, Presented at the AIAA 7th Computational Fluid Dynamics Conference, Cincinnati, Ohio, July 15-17, 1985.

[126]Batina, J. T.: "Unsteady Transonic Algorithm Improvements for Realistic Aircraft Applications." AIAA Paper No. 88-0105, Presented at the AIAA 26th Aerospace Sciences Meeting, Reno, Nevada, January 11-14, 1988.

[127]Cunningham, H. J.; Batina, J. T.; and Bennett, R. M.: "Modern Wing Flutter Analysis by Computational Fluid Dynamics Methods." ASME Paper No. 87-WA/Aero-9, Presented at the ASME Winter Annual Meeting, Boston Massachusetts, December 13-18, 1987.

[128]Osher, S.; Hafez, M.; and Whitlow, W., Jr.: "Entropy Condition Satisfying Approximations for the Full Potential Equation of Transonic Flow." Mathematics of Computations, Vol. 44, pp. 1 29, January 1985.

[129]Whitlow, W., Jr.: "Application of a Nonisentropic Full Potential Method to AGARD Standard Airfoils." AIAA Paper No. 88-0710, Presented at the AIAA 26th Aerospace Sciences Meeting, Reno, Nevada, January 11-14, 1988.

[131]Levine, M. S.: "Body-Conforming Grids for General Unsteady Airfoils Motion." Purdue University, Dep. of Aeronautics and Astronautics, M. S. Thesis, August 1987.

[132]Steger, J. L.; and Warming, R. F.: "Flux Vector Splitting of the Inviscid Gasdynamic Equations with Application to Finite-Difference Methods." Journal of Computational Physics, Vol. 40, 1981, pp. 263-293.

[133]Harten, A.; Lax, P. D.; and Van Leer, B.: "On Upstream Differencing and Godunov-Type Schemes for Hyperbolic Conservation Laws." SIAM Review, Vol. 25, 1983, pp. 35-61.

[134]Chakravarthy, S.; and Osher, S.: "A New Class of High Accuracy TVD Schemes for Hyperbolic Conservation Laws." AIAA Paper 85-0363, January 1985.

[135]Thomas; J. L.; Van Leer, B.; and Walters, R. W.: "Implicit Split-Flux Schemes for the Euler Equations." AIAA Paper No. 85-1680, July 1985.

[136]Yee, H. C.; and Harten, A.: "Implicit TVD Schemes for Hyperbolic Conservation Laws in

Curvilinear Coordinates." AIAA Paper No. 85-1513(CP), July 1985.

[137]Chakravarthy, S. R.: "Relaxation Methods for Unfactored Implicit Schemes." AIAA Paper No. 84-0165, January 1984.

[138]Roe, P. L.: "Characteristics Based Schemes for the Euler Equations." Annual Review of Fluid Mechanics, Vol. 18, pp. 337-65, 1986.

[139]Coakley, T. J.: "Implitic Upwind Methods for the Compressible Navier-Stokes Equations." AIAA Paper No. 83-1958, July 1983.

[140]Thomas, J. L.; and Walters, R. W.: "Upwind Relaxation Algorithms for the Navier-Stokes Equations." AIAA Paper No. 85-1501, July 1985.

[142]Ying, S. X.; Steger, J. L.; Schiff, L. B.; and Baganoff, D.: "Numerical Simulation of Unsteady, Viscous, High-Angle-of-Attack Flows Using a Partially Flux-Split Algorithm." AIAA Paper No. 86-2179, August 1986.

[143]Anderson, W. K.; Thomas, J. L.; and Whitfield, D. C.: "Multigrid Acceleration of the Flux-Split Euler Equations." AIAA Paper No. 86-0274, January 1986.

[144]Anderson, W. K.: "Implicit Multigrid Algorithms for the Three-Dimensional Flux-Split Euler Equations." Ph.D. Dissertation, Mississippi State University, Mississippi, August 1986.

[145]Jesperson, D. C.: "A Time-Accurate Multiple-Grid Algorithm." AIAA Paper No. 85-1493(CP), July 1985.

[146]Kandil, Osama A.; and Chuang, H. Andrew: "Unsteady Vortex-Dominated Flows Around Maneuvering Wings Over a Wide Range of Mach Numbers." AIAA Paper No. 88-0317, Presented at the AIAA 26th Aerospace Sciences Meeting, Reno, Nevada, January 11-14, 1988.

[147]Rumsey, C. L.; and Anderson, W. K.: "Some Numerical and Physical Aspects of Unsteady Navier-Stokes Computations Over Airfoils Using Dynamic Meshes." AIAA Paper No. 88-0329, presented at the AIAA 26th Aerospace Sciences Meeting, Reno, Nevada, January 1988.

[148]Deiwert, G. S.: "Computation of Separated Transonic Turbulent Flows." AIAA Paper No. 75 829, Hartford, Connecticut, June 1975.

[149]Le Balleur, J. C.; and Girodroux-Lavigne, P.: "A Viscous-Inviscid Interaction Method for Computing Unsteady Transonic Separation." Proc. 3rd Symposium on Numerical and Physical Aspects of Aerodynamic Flows, ed. T. Cebici, Springer-Verlag, 1986.

[150]Johnson, D. A.: "Predictions of Transonic Separated Flow with an Eddy-Viscosity/Reynolds Shear Stress Closure Model." AIAA Paper No. 85-1683, July 1985.

[151]Simpson, R.: "A Review of Two-Dimensional Turbulent Separated Flow Calculation Methods." IUTAM Symposium on Boundary Layer Separation, August 1986.

[152]Coakley, T. J.: "Impact of Turbulence Modeling on Numerical Accuracy and Efficiency of Compressible Flow Simulations." 10th International Conference on Numerical Methods in Fluid Mechanics, Bejing, China, June 1986.

[153]Steger, J. L.: "Implicit Finite-"Difference Simulation of Flow about Arbitrary Two-Dimensional Geometries." AIAA Journal, Vol. 16, No. 7, July 1978.

[154]Rumsey, C. L.; Thomas, J. L.; Warren, G. P.; and Liu, G. C.: "Upwind Navier-Stokes Solutions for Separated Periodic Flows." AIAA Paper No. 86-0247, Presented at the AIAA 24th Aerospace Sciences Meeting, Reno, Nevada, January 1986.

[155]Edwards, J. W.: "Applications of Potential Theory Computations to Transonic Aeroelasticity." Paper No. ICAS-86-2.9.1, Fifteenth Congress of the International Council of the Aeronautical Sciences, London, England, September 1986.

Table 1. References giving comparisons of experimental and calculated two-dimensional unsteady aerodynamics
(References from Edwards and Thomas[1])

	TSD	FP	EE	NS
NACA 64A006	6, 103*, 88, 89, 87*	102, 116	5, 15	
NACA 64A010A	80, 82, 138, 82, 89, 112*, 87*, 93, 97+, 114*, 105*-108*	117, 116, 79, 119	15, 30, 32	19, 18
NACA 0012	88, 90*, 109*, 97+, 96+, 93	119, 100+	29, 28, 31	152, 44, 149 43, 154
NLR 7301	89, 88, 107*, 114*, 97+	117	16, 30, 32	
MBB A-3	112*, 89, 82, 138, 114*, 63			
Supercritical Airfoils	154*, 109*, 65*, 66			
Circular arc Airfoils	106*, 107*, 108*			35, 37, 36, 40
Other			151	17, 42, 43, 148

* Interacted boundary layer model
+ Nonisentropic corrections

Table 2. References giving comparisons of experimental and calculated three-dimensional unsteady aerodynamics and aeroelasticity
(References from Edwards and Thomas[1])

	TSD	FP	EE
F-5 Model	115, 157, 137, 23	24, 136, 153, 102	
NORA	76, 22	64, 26	
LANN	100, 156	45, 40, 24, 76	
RAE Wing A		64, 43, 26, 136	
RSW	116, 75	40, 66, 76, 25	96, 34
RAE Tailplane	114, 85+, 155, 98+		75, 33
Other	118*, 113*, 71*, 73*	64*, 65*, 26*, 70*	

+ Nonisentropic corrections
* Aeroelastic and flutter comparisons

Table 4. Local singularity solutions for oscillating lifting surfaces. Note that in all cases the control surface angle is $\delta(y,t) = \delta(y)e^{-i\omega t}$ (Reference given in Ref. 93).

Problem	Sketch	Inner Solution for Subsonic Edge	Inner Solution for Supersonic Edge	References
Control Surface Leading Edge (No Gap or Aerodynamic Balance)	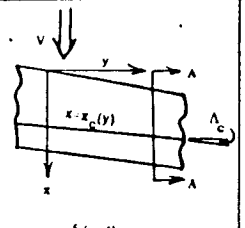	$\Delta\bar{C}_p(x,y)$ $= \frac{-4\bar{\delta}(y)\cos\Lambda_c}{\pi\sqrt{1-M^2\cos^2\Lambda_c}} \ln\lvert x-x_c\rvert$	No Singularity	1, 5*, 6*
Control Surface Side Edge	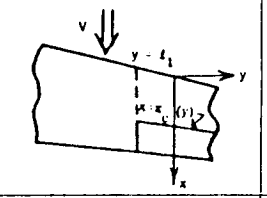	$\Delta\bar{C}_p(x,y) = \frac{4\bar{\delta}(\ell_1)}{\pi}\left\{2i\frac{\omega}{V} - \frac{\omega^2}{V^2}\lvert x-x_c(\ell_1)\rvert\right\}\lvert y-\ell_1\rvert \ln\lvert y-\ell_1\rvert$	Apparently the Same	1, 5*, 6*
Control Surface Corner	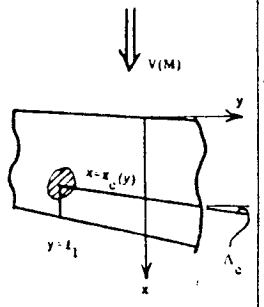	$\Delta\bar{C}_p(x,y) = \frac{-2\bar{\delta}(y)\cos\Lambda_c}{\pi\sqrt{1-M^2\cos^2\Lambda_c}} \cdot \left\{1 + 2i\frac{\omega}{V}\lvert x-x_c(y)\rvert\right\} \cdot \ln\left\{\sqrt{(x-x_c)^2+\beta^2(y-\ell_1)^2} - \beta(y-\ell_1)\right\} + \frac{2\bar{\delta}(\ell_1)}{\pi}\left\{2i\frac{\omega}{V} - \frac{\omega^2}{V^2}\lvert x-x_c(\ell_1)\rvert\right\} \cdot (y-\ell_1)\lvert\ln\left\{\sqrt{(x-x_c)^2+\beta^2(y-\ell_1)^2} - (x-x_c)\right\}\rvert$	Not Known to Author	1, 5*, 6*
Control Surface which Intersects Wingtip	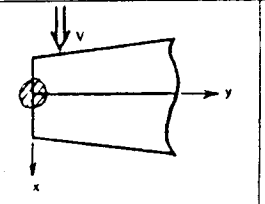	$\Delta\bar{C}_p(x,y)$ $= \frac{-2\bar{\delta}(y)}{\pi\beta}\ln\left[\frac{1-\sqrt{1-e^{-2Q_o}}}{1+\sqrt{1-e^{-2Q_o}}}\right]$, where $Q_o = \sinh^{-1}\left(\frac{\beta y}{\lvert x\rvert}\right)$ and $y \geq 0$ (Available for swept edge as an integral, Ref. 6)	No Singularity. Can be obtained as standard steady supersonic control surface solution (e.g., Ref. 7).	1, 6

Table 5. Global singularities and situations where the local flow may be irregular on interfering surfaces (References given in Ref. 93)

Problem	Sketch	Inner or Local Solution for Subsonic Edges	Supersonic Edges	References
Leading, side and Trailing Edges	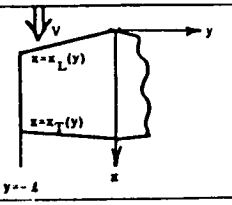	$\Delta\bar{C}_p(x,y)$ $= \begin{cases} C_1(y)\lvert x-x_L\rvert^{-1/2}, & \text{L. E.} \\ C_2(x)\lvert y+\ell\rvert^{1/2}, & \text{side edge} \\ C_3(y)\lvert x_T-x\rvert^{1/2}, & \text{T. E.} \end{cases}$	No Singularity	Well-Known (e.g., 1)
Swept-Wing Vertex	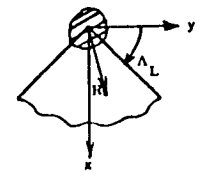	$\bar{\varphi} \sim R^n f(\frac{x}{R}, \frac{y}{R}, \frac{z}{R})$, where $n = n(\Lambda_L)$. $n = \lvert\frac{1}{2} + \frac{\sin\Lambda_L}{\pi}\rvert$, $\Lambda_L = 0$, $n = \lvert 1 - \frac{1}{4}(\frac{\pi}{2} - \Lambda_L)^2\rvert$, $\Lambda_L = \frac{\pi}{2}$ $\Delta\bar{C}_p(x,y)$, in all cases, has square-root singularity at L. E.	Nonsingular Conical Flow	10 and Refs. contained therein
Other Planform Discontinuities	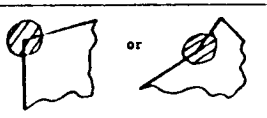	Not Know to Author	Not Known to Author	
Fold or Dihedral Change	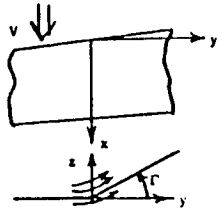	Upper surface: $\bar{\varphi}(x,y,z)$ $= C_{L_1}(x)\mathrm{Re}\left\{e^{\frac{-i[\Gamma/(1-\frac{\Gamma}{\pi})]}{(y+iz)^{\frac{\pi}{\pi-\Gamma}}}}\right\}$ Lower Surface: $\bar{\varphi}(x,y,z)$ $= C_{L_2}(x)\mathrm{Re}\left\{e^{\frac{i[\Gamma/(1+\frac{\Gamma}{\pi})]}{(y+iz)^{\frac{\pi}{\pi+\Gamma}}}}\right\}$ (Velocity singular at lower-surface corner).	Rodemich solution applies (Refs. 11, 12): Local source strength ~ (Distance from Fold Line)$^{-1}$	For Subsonic "crossflow," p. 150 of Ref. 12
Intersection of Two Surfaces	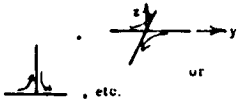	Above solution believed to apply locally. (No velocity Singularity).	Not Known to author. Rodemich method can be applied in numerical solutions.	
Gap in Wing Surface or Between Wing and Control Surface	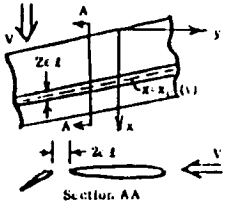	For $M=0$, $u = \ldots$ $C_4(y)\left\{1 - \frac{2}{\pi}\ln\left(\frac{\eta+1+\sqrt{\eta^2-1}}{\eta+1-\sqrt{\eta^2-1}}\right)\right\}$ $+C_5(y)\sqrt{\frac{\eta+1}{\eta-1}}$, where $\eta = \frac{x-x_c(y)+iz}{\epsilon}$ C_4 and C_5 to be found by matching and Kutta condition at front edge of gap	Not Known to Author	14 (also treats gaps parallel to the flight direction).

TABLE 6
Current Levels of Accuracy for Aeroelastic Analysis

Wing Flutter	~ 10%
Gust Response	~ 10%
Loads	5 - 10%
Control Effectiveness	25 - 50%
Control Hinge Moments	25 - 50%
Buffet Loads	20 - 30%

TABLE 7
COMPUTER RESOURCE REQUIREMENTS FOR FLUTTER BOUNDARY
(From Ref. 100)

WING/BODY/CANARD CONFIGURATION
10 MACH NUMBERS (40 CASES) PER ANALYSIS

$$\text{TIME} = (\text{GRID PTS}) \times \frac{\text{OPS}}{(\text{GRID PTS} \times \text{ITER})} \times (\text{ITER}) / \left(\frac{\text{OPS}}{\text{SEC}}\right)$$

FLOW REGION	FLOW MODEL	VPS-32 (100 MFLOPS)	NAS (250 MFLOPS)
1, MAYBE II	TSD WITH 2-D STRIP BOUNDARY LAYER	30 HOURS	12 HOURS
I, MAYBE II	POTENTIAL WITH 2-D STRIP BOUNDARY LAYER	45 HOURS	18 HOURS
I, II, MAYBE III	EULER WITH 2-D STRIP BOUNDARY LAYER	65 HOURS	26 HOURS
II, III	NAVIER-STOKES (RE = 10^8)	1611 HOURS	644 HOURS

TABLE 8
COMPUTER RESOURCE REQUIREMENTS TO DETERMINE FLUTTER POINT AT A SPECIFIED MACH NUMBER
(From Ref. 100)

(4000 TIME STEPS PER FLUTTER POINT)

CONFIGURATION	FLOW MODEL	GRID POINTS	CPU HOURS (VPS-32)
COMPLETE AIRCRAFT	TSD	0.75M	2.3*
COMPLETE AIRCRAFT	FULL NAVIER-STOKES (RE = 10 MILLION)	7.00M	77.8**

*BASED ON ACTUAL CASES

**ASSUMES COMPUTATIONAL SPEED OF 100 MFLOPS

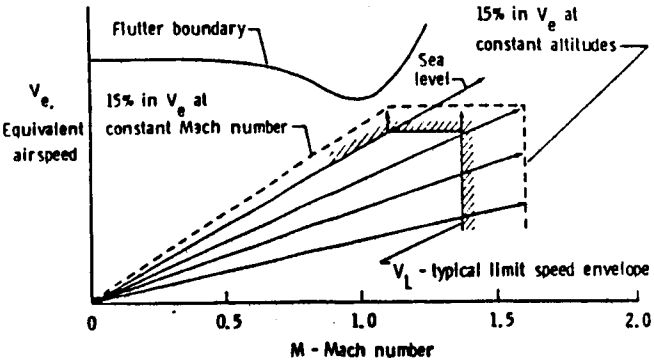

Fig. 1 Graphical representation of minimum required flutter margin, (Ref. 2).

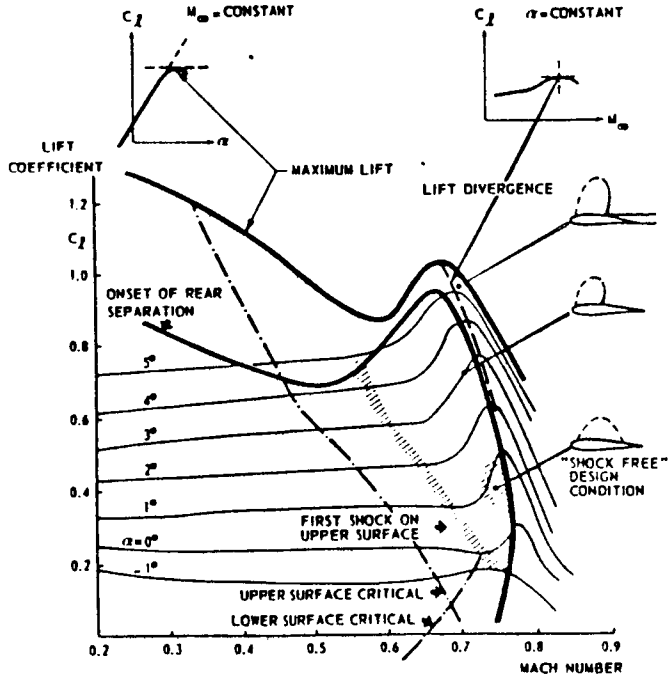

Fig. 2 Main characteristics and boundaries for the onset of separation for the NLR 7301 supercritical airfoil.
(Tijdeman, Ref. 3)

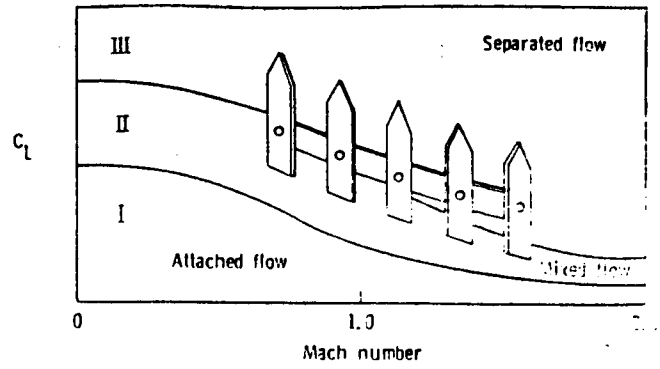

Fig. 3 Characteristics of attached and separated flow for complete aircraft. (after Bradley, Ref. 5)

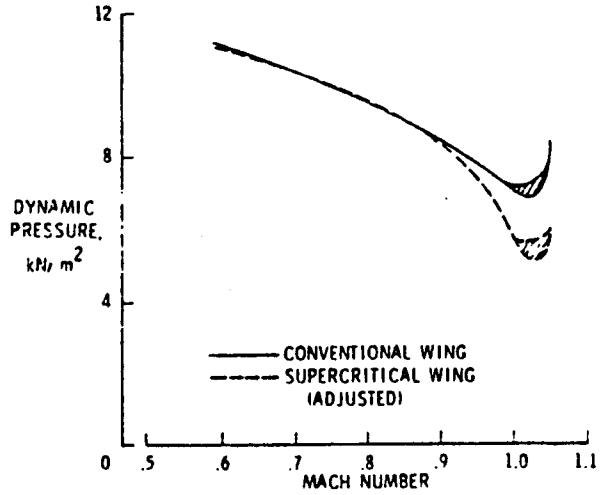

Fig. 4 Comparison of conventional wing flutter boundary with adjusted supercritical wing boundary
(Farmer et al., Ref. 6)

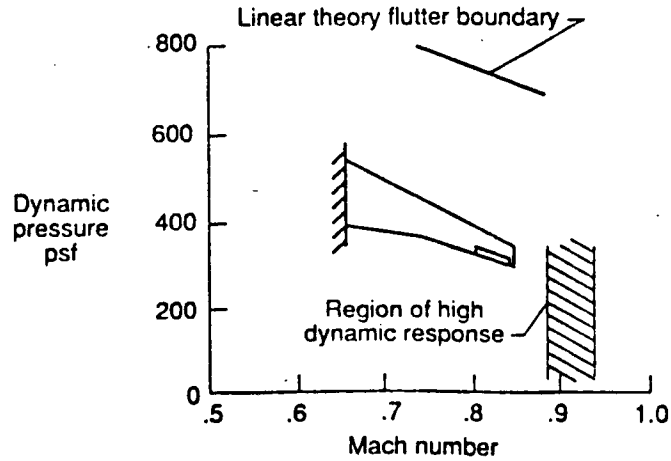

Fig. 5 DAST ARW-2 region of shock-induced high dynamic response, (Ref. 11).

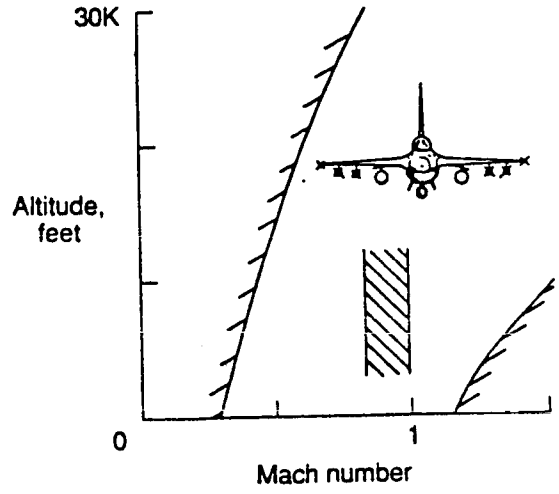

Fig. 6 High dynamic response region due to wing/store loading, (Ref. 100).

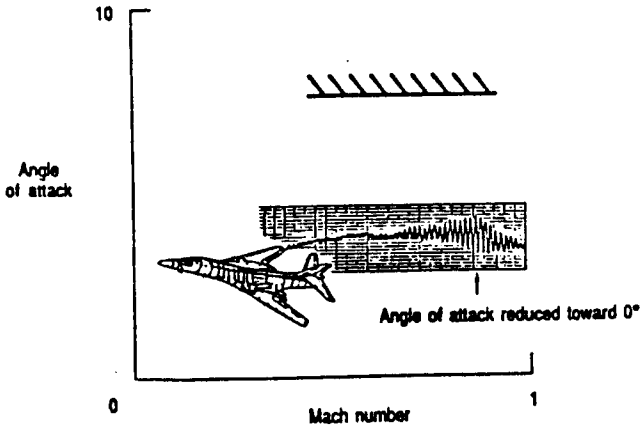

Fig. 7 High dynamic response region due to angle-of-attack, (Ref. 12).

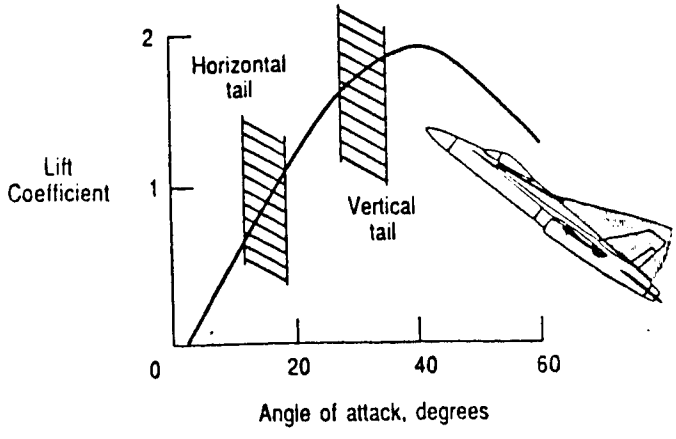

Fig. 8 Regions of vortex-induced buffet loads, (Ref. 100).

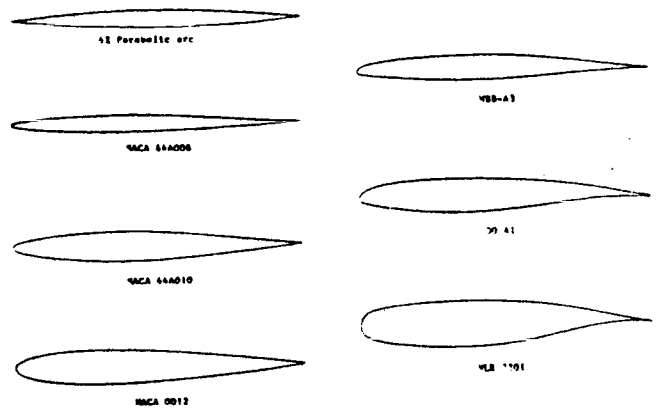

Fig. 9 AGARD Structures and Materials Panel two-dimensional standard aeroelastic configurations.
(Bland, Ref. 16).

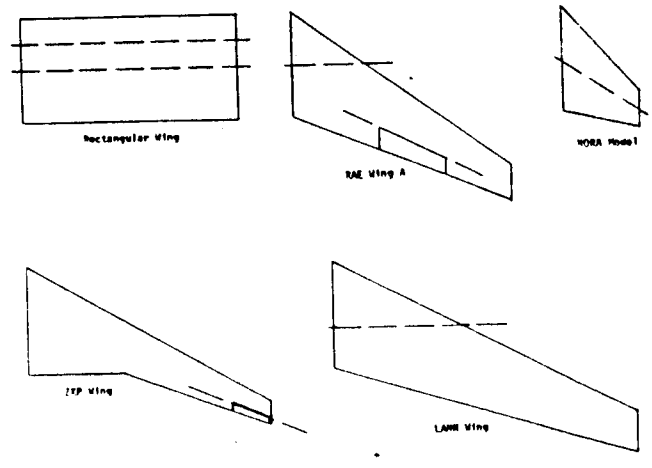

Fig. 10 AGARD Structures and Materials Panel three-dimensional standard aeroelastic configurations.
(Bland, Ref. 17).

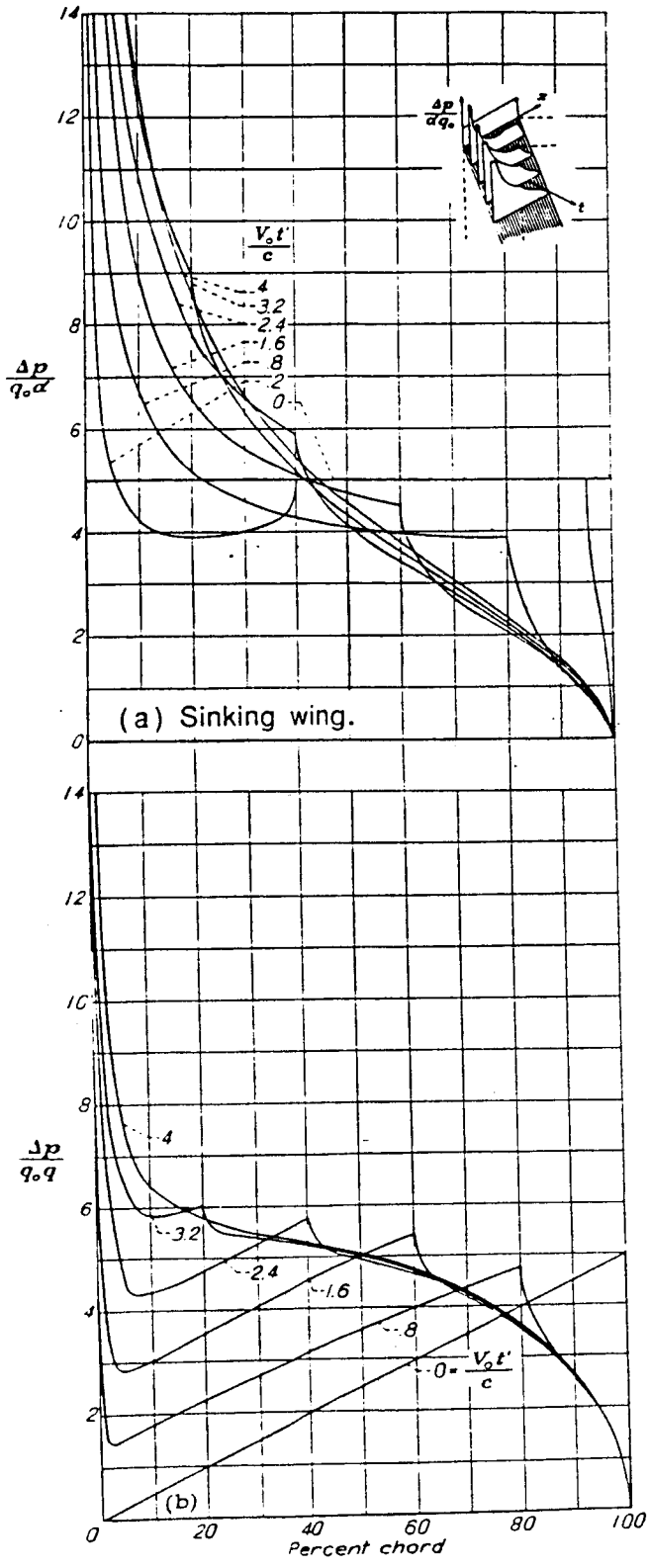

(b) Wing pitching about its leading edge.

Fig. 11 Variation of two-dimensional indicical load distribution with percent chord for a Mach number equal to 0.8. (Lomax et al., Ref. 97).

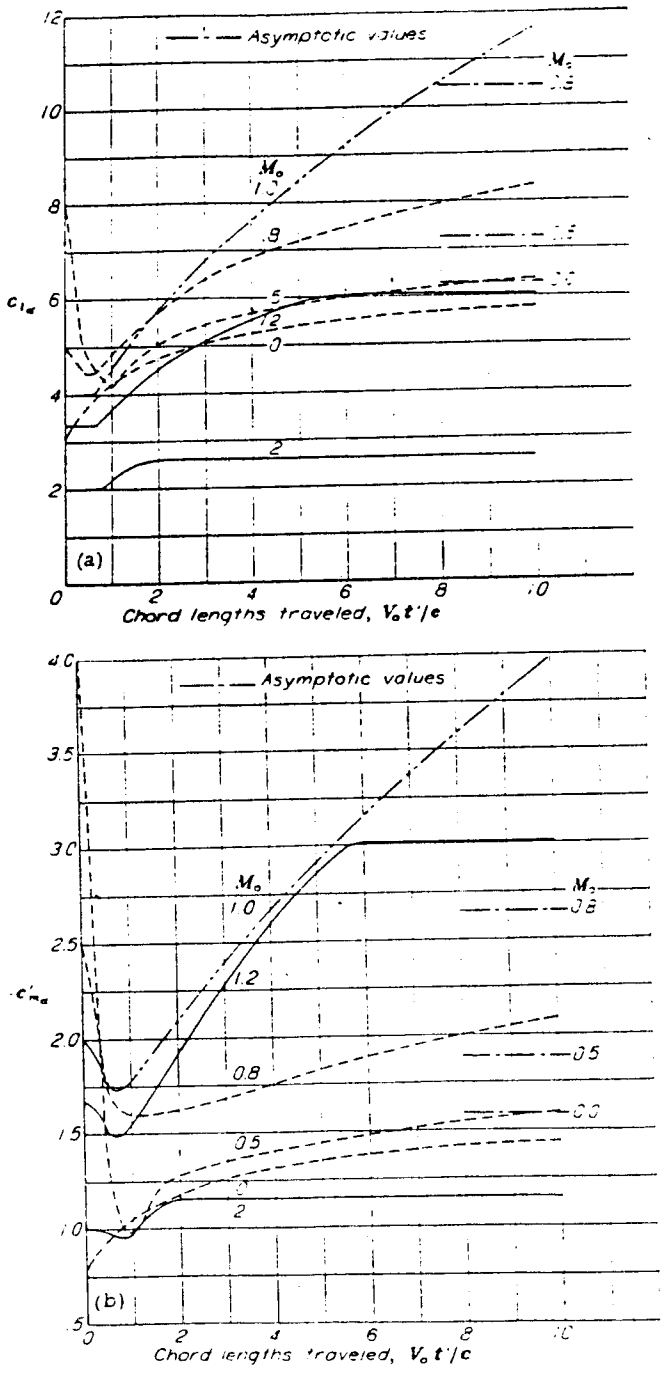

Fig. 12 Variation of two-dimensional indicial lift and pitching-moment coefficients with chord lengths traveled for several mach numbers. (sinking wing)

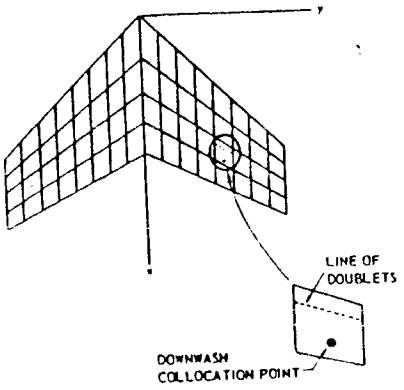

Fig 13 Surface and panel geometry for doublet-lattice method.
(Albano and Rodden, Ref. 95)

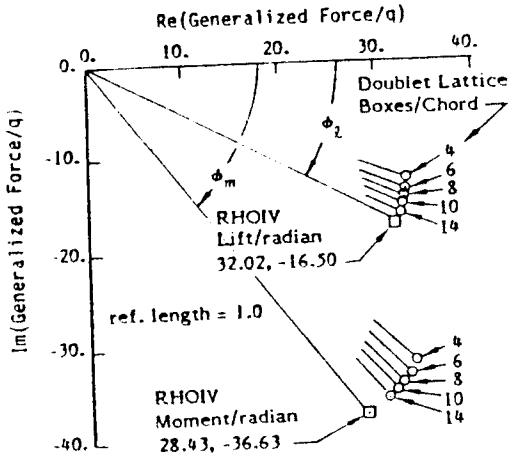

Fig. 14 Comparison of generalized force vectors predicted by RHOIV and doublet lattice on a rectangular wing of AR = 4, pitching about the trailing edge at k = 0.3, M = 0.9, wave number = 2.7.
(Rowe and Cunningham, Ref. 96)

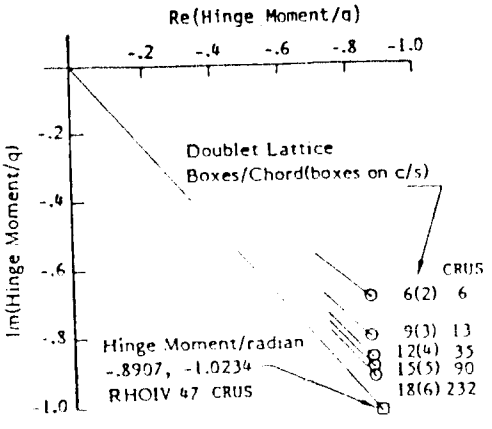

Fig. 15 Hinge moment vectors due to control surface motions for a wave number of 5.4.
(Rowe and Cunningham, Ref. 96)

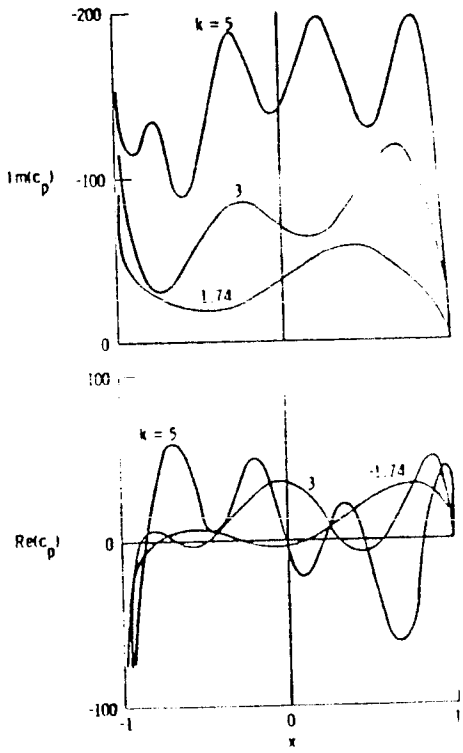

Fig. 16 Pressure coefficient distribution due to airfoil plunging as a function of x and k at Mach 0.7.
(Edwards, Ref. 98)

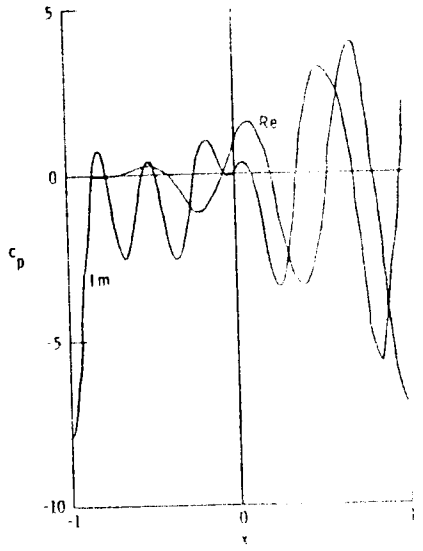

Fig. 17 Pressure coefficient distribution due to airfoil plunging as a function of x and k at Mach 1.02 and k = 0.4.
(Edwards, Ref. 98)

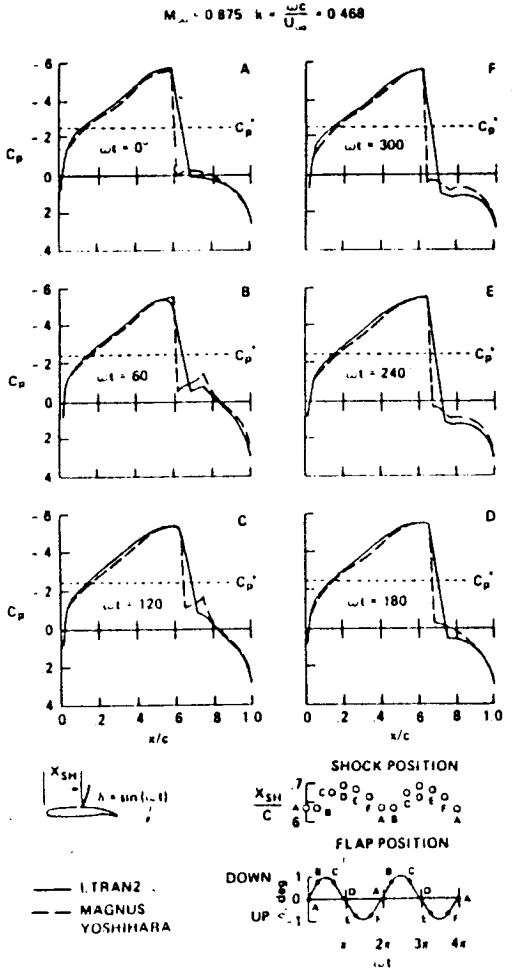

(a) Type A shock motion.

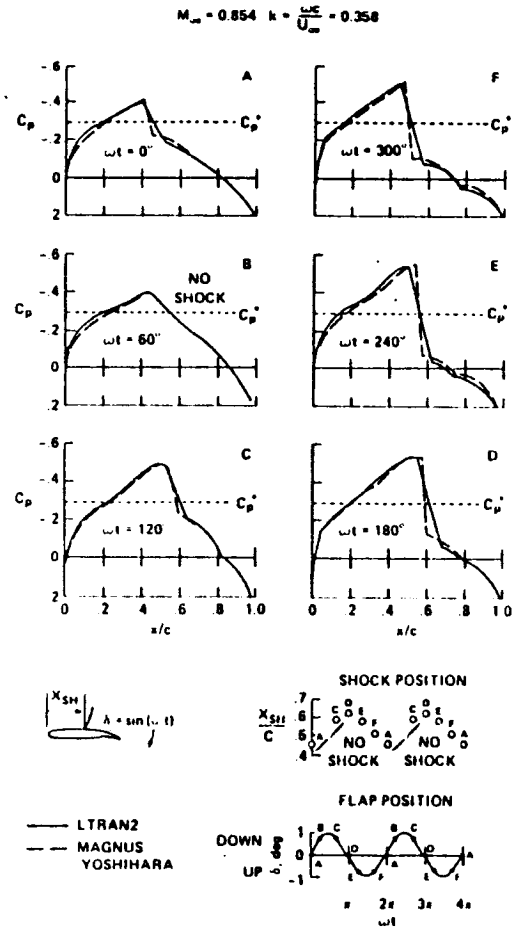

(b) Type B shock motion.

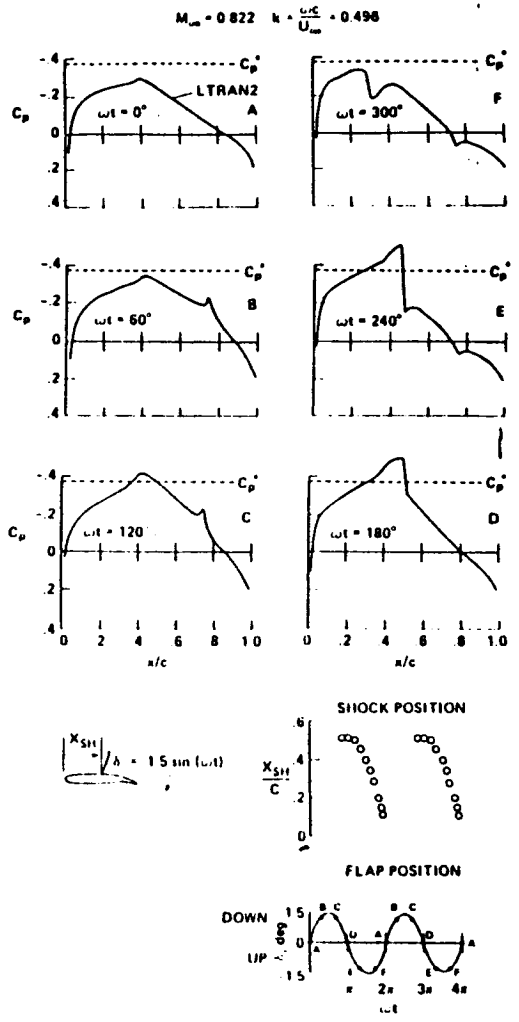

(c) Type C shock motion.

Fig. 20 Upper surface pressure coefficients of an NACA 64A006 airfoil with oscillating trailing-edge flap showing type A, B, and C shock motions.

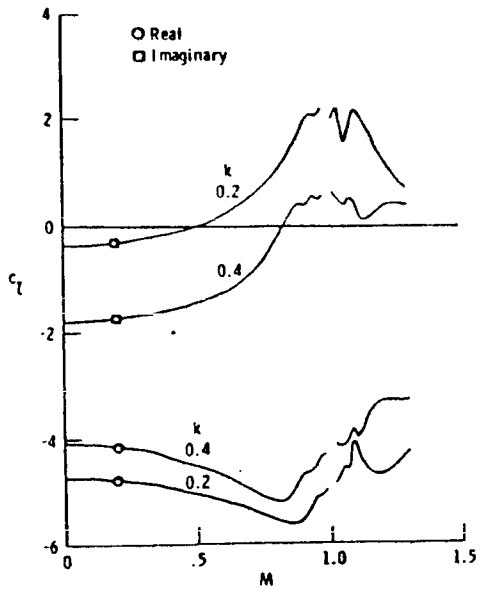

Fig. 18 Lift coefficient of a typical section due to pitching about the quarter-chord as a function of Mach number for reduced frequencies of 0.2 and 0.4. (Edwards, Ref. 98)

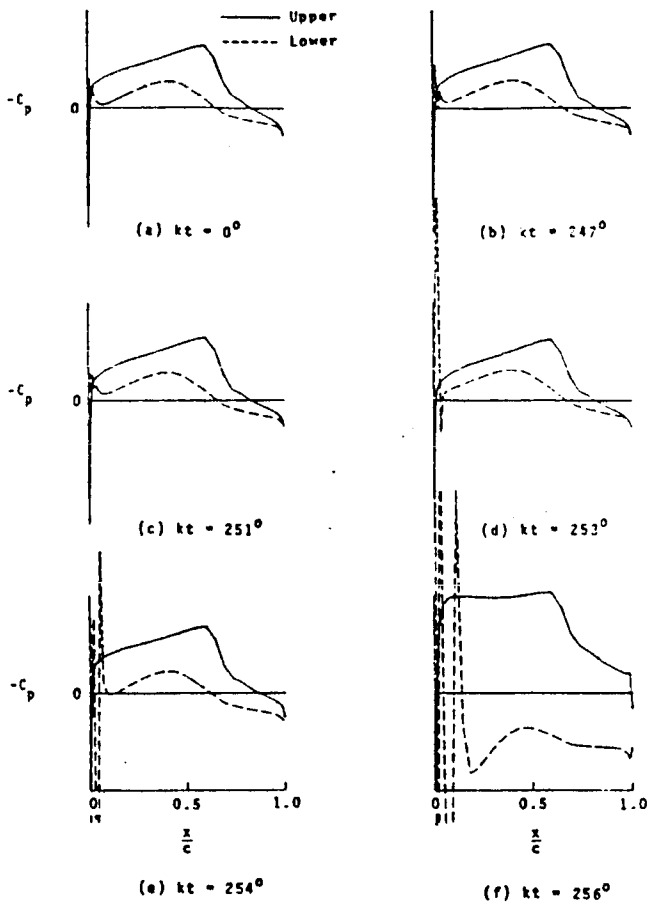

Fig. 21 Pressure distributions on a pitching MBB-A3 airfoil at M = 0.8 and k = 0.2; Murman-Cole differencing. (Whitlow, Ref. 101)

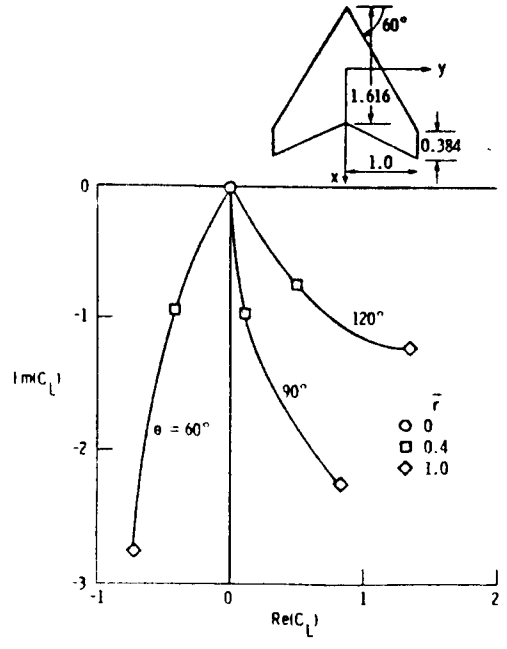

Fig. 19 Generalized lift coefficient of a wing due to rigid plunging at Mach 0.5 as a function of $\bar{r}$ and θ. (Edwards, Ref. 98)

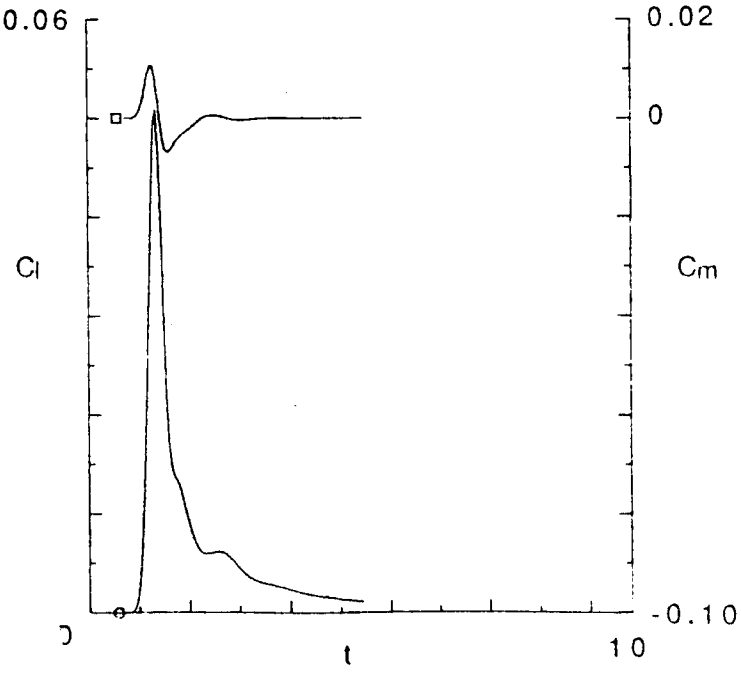

Fig. 22 Lift and moment transient response for an NACA 0012 airfoil at M = 0.78 and α = 0° due to pulsed pitching motion.

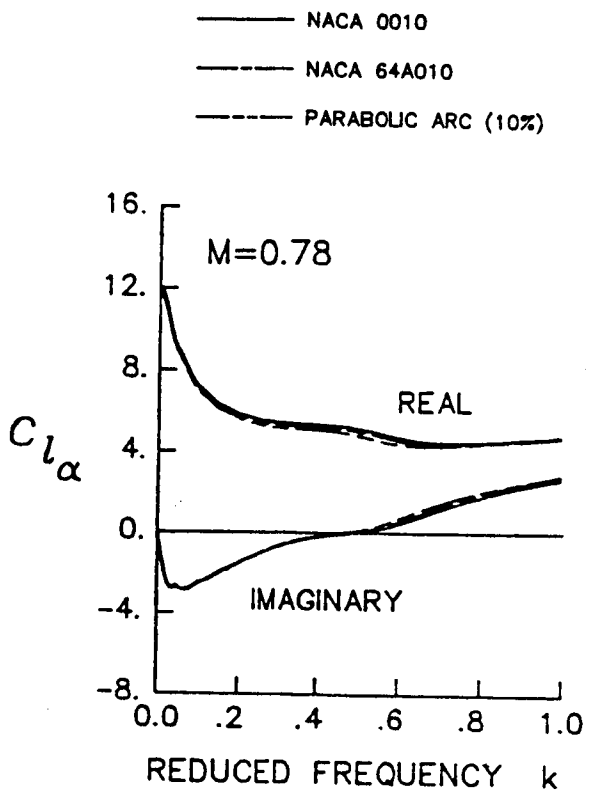

Fig. 23 Lift and moment coefficient frequency response functions from pulse transfer analysis.
(Batina, Ref. 108)

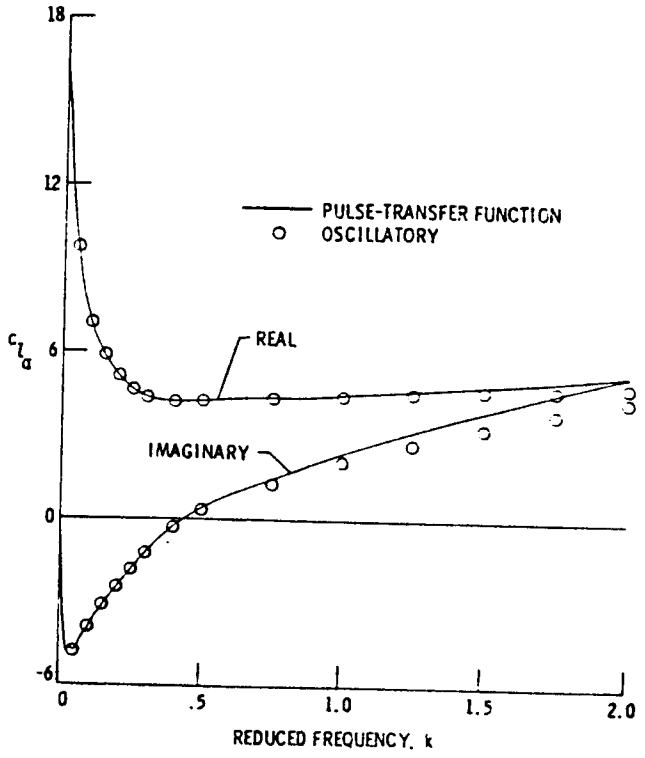

Fig.. 24 Unsteady forces for a 6% parabolic arc airfoil calculated by pulse and oscillatory analyses; XTRAN2L default grid, M = 0.85.
(Seidel et al., Ref. 107)

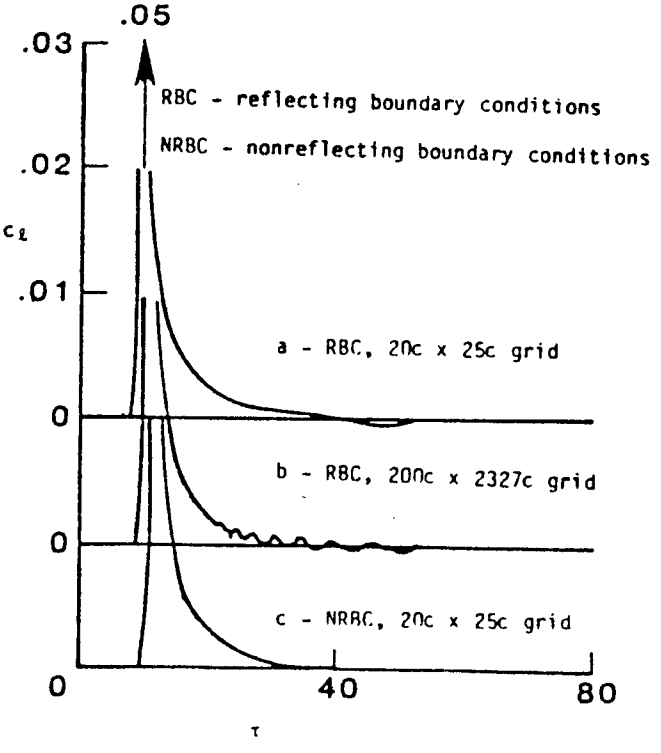

Fig. 25 Lift coefficient time histories due to pulsed pitching motion for flate plate airfoil at M = 0.85.
(Edwards, Ref. 155)

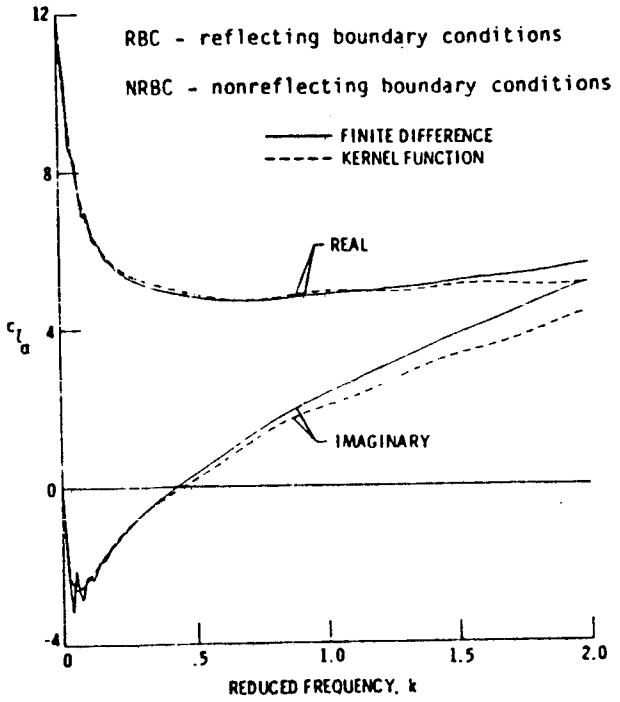

a) RBC, 20c x 25c grid

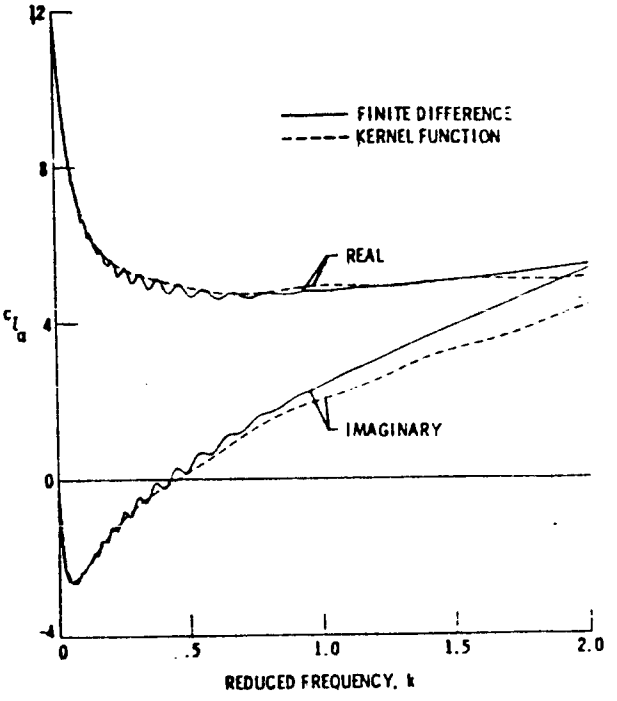

b) RBC, 200c x 2327c grid

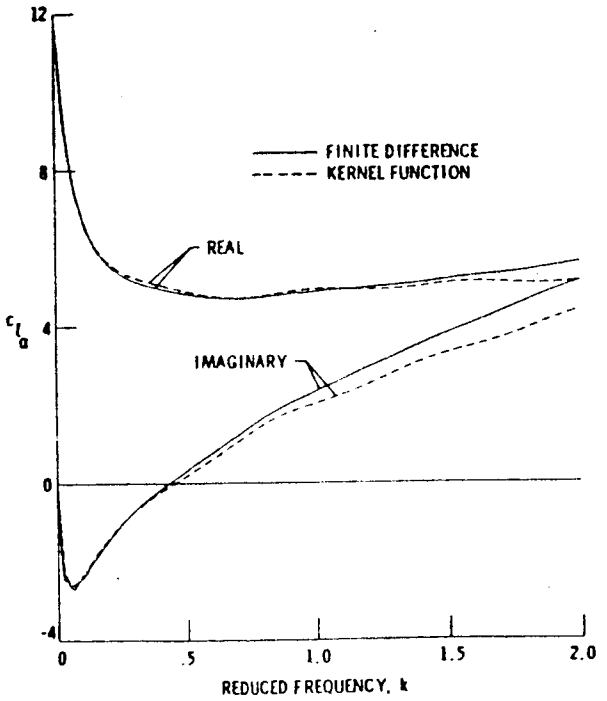

c) NRBC, 20c x 25c grid

Fig. 26 Lift coefficient frequency response functions due to pulsed pitching motion for flap plate airfoil at M = 0.85.
(Seidel et al., Ref. 107)

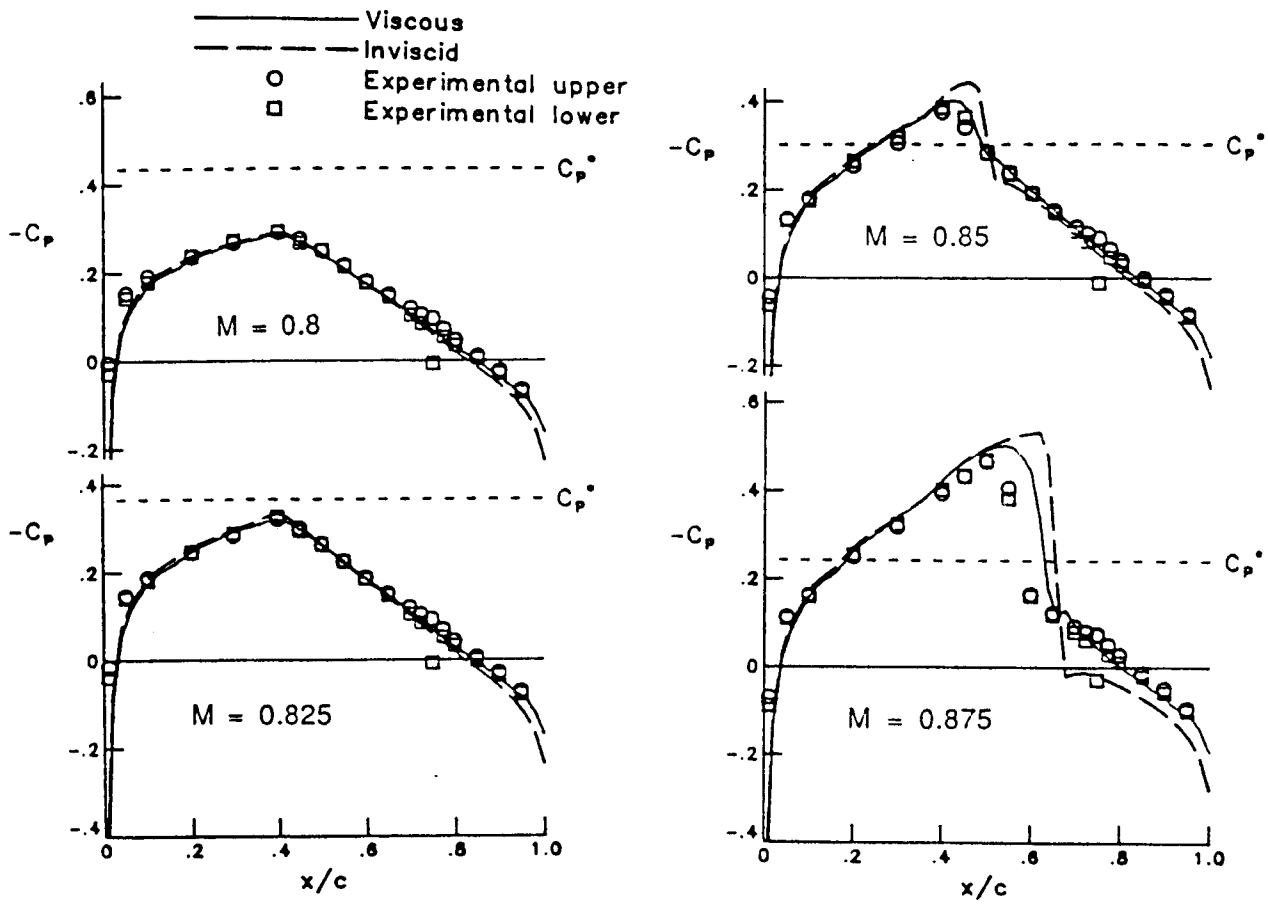

Fig. 27 Steady pressure distribuitons for the NACA 64A006 airfoil. (Howlett and Bland, Ref. 110)

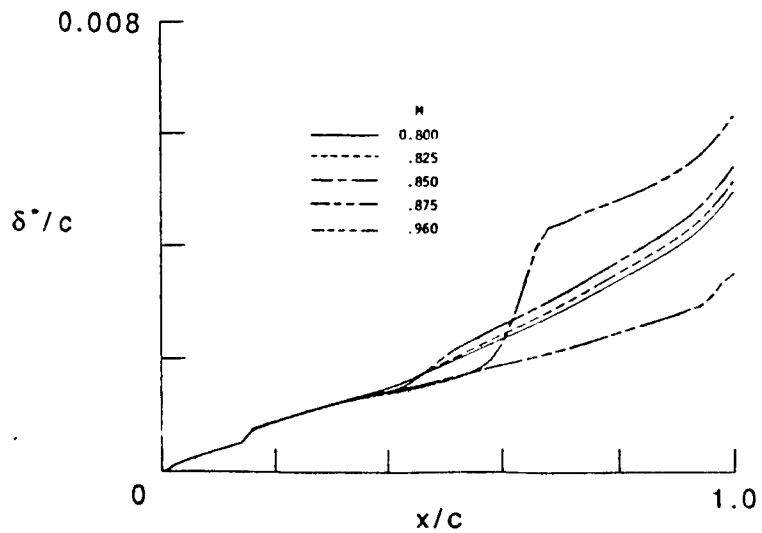

Fig. 28 Effect of Mach number on boundary-layer displacement thickness for NACA 64A006 airfoil. (Howlett and Bland, Ref. 110)

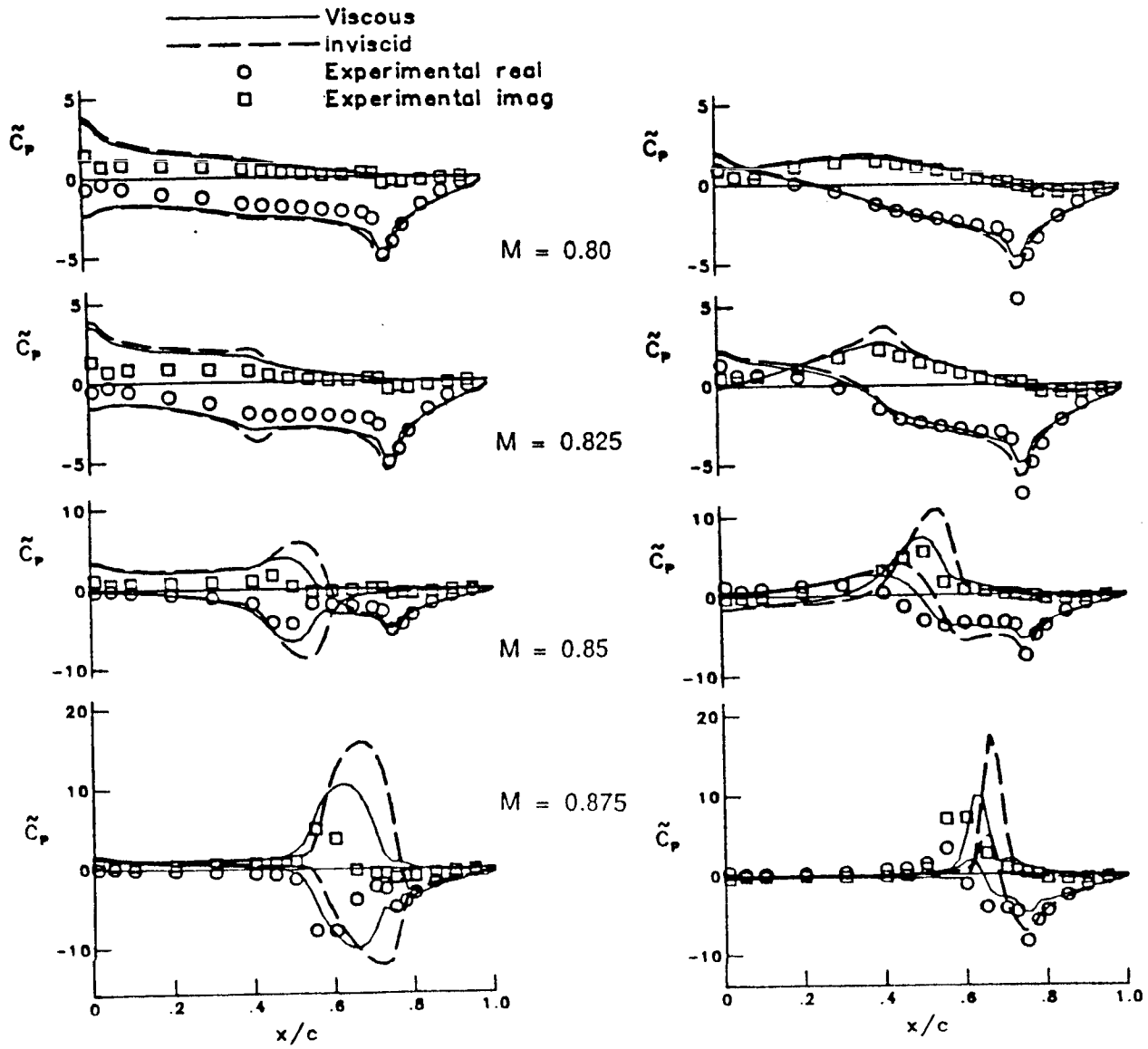

(a) k = 0.06

(b) k = 0.24

Fig. 29 Unsteady upper surface pressure distributions for the NACA 64A006 airfoil at $\delta_0 = 1°$. (Howlett and Bland, Ref. 110)

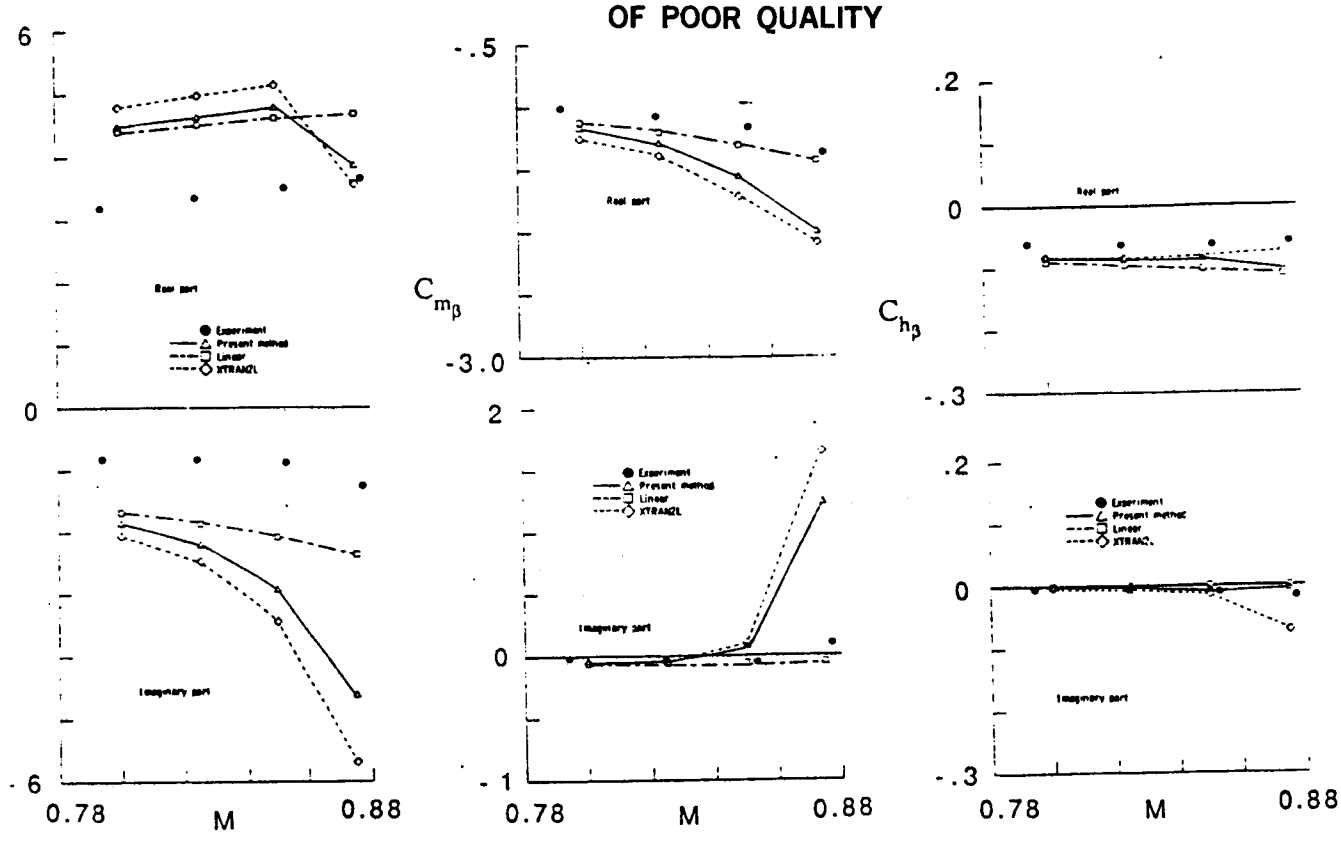

Fig. 30 Comparison of unsteady forces for the NACA 64A006 airfoil at δ_o = 1° and k = 0.06. (Howlett and Bland, Ref. 110)

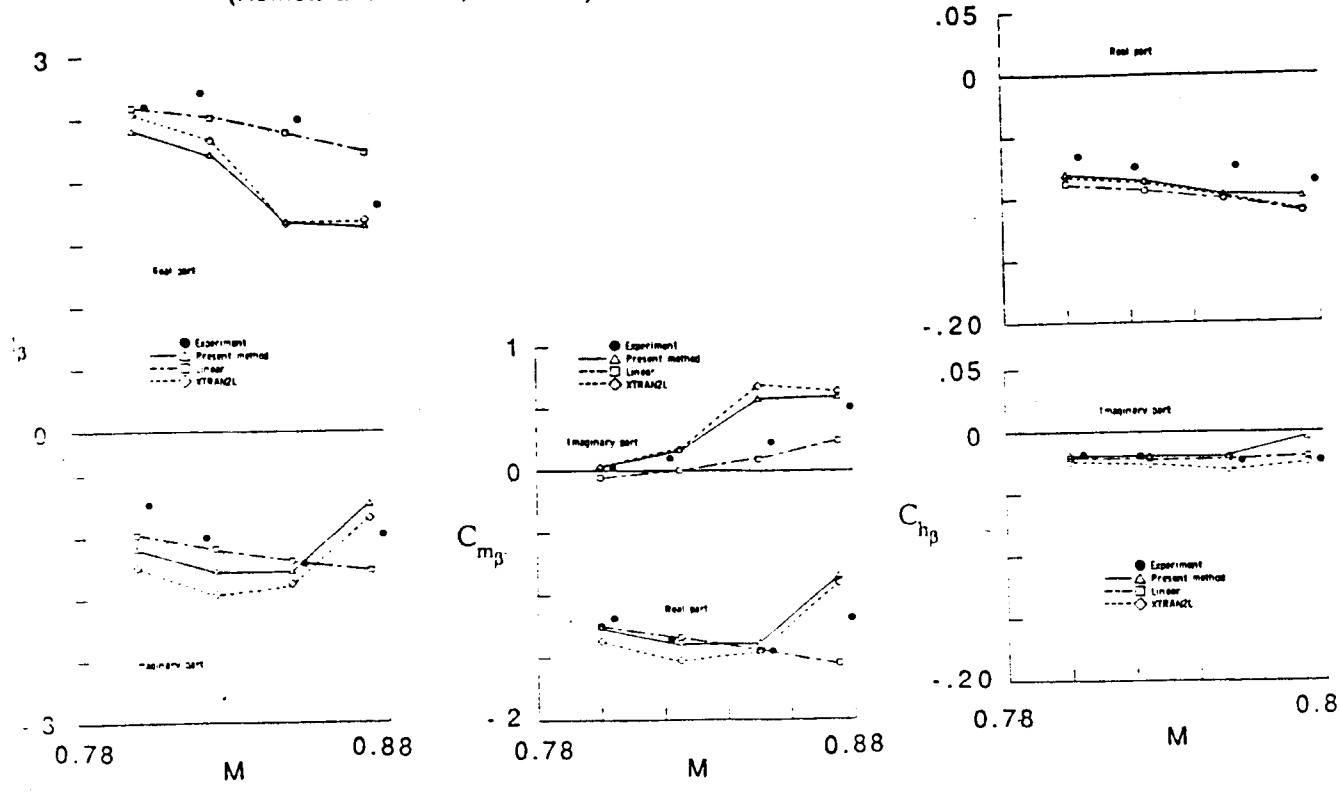

Fig. 31 Comparison of unsteady forces for the NACA 64A006 airfoil at δ_o = 1° and k = 0.24. (Howlett and Bland, Ref. 110).

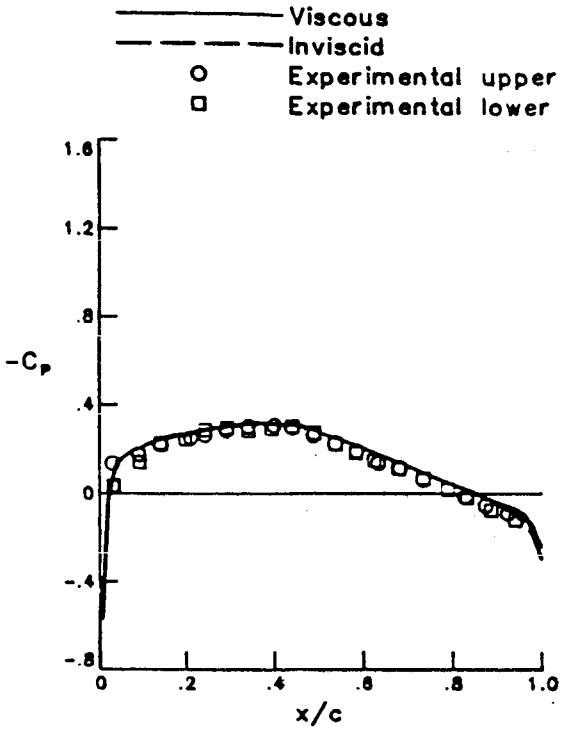

(a) M = 0.502, Re = 10.0 x 10^6.

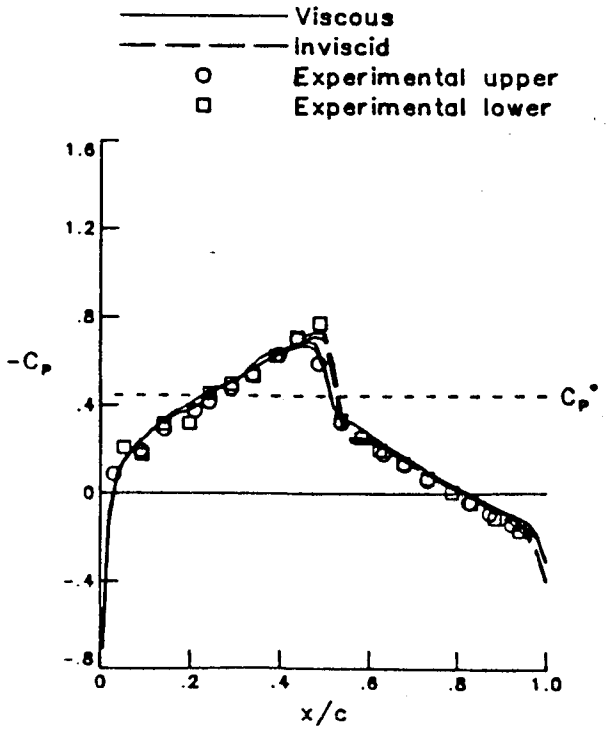

(b) M = 0.796, Re = 12.5 x 10^6.

Fig. 32 Steady pressure distribution for the NACA 64A010A airfoil, $\alpha_m = 0°$. (Howlett and Bland, Ref. 110).

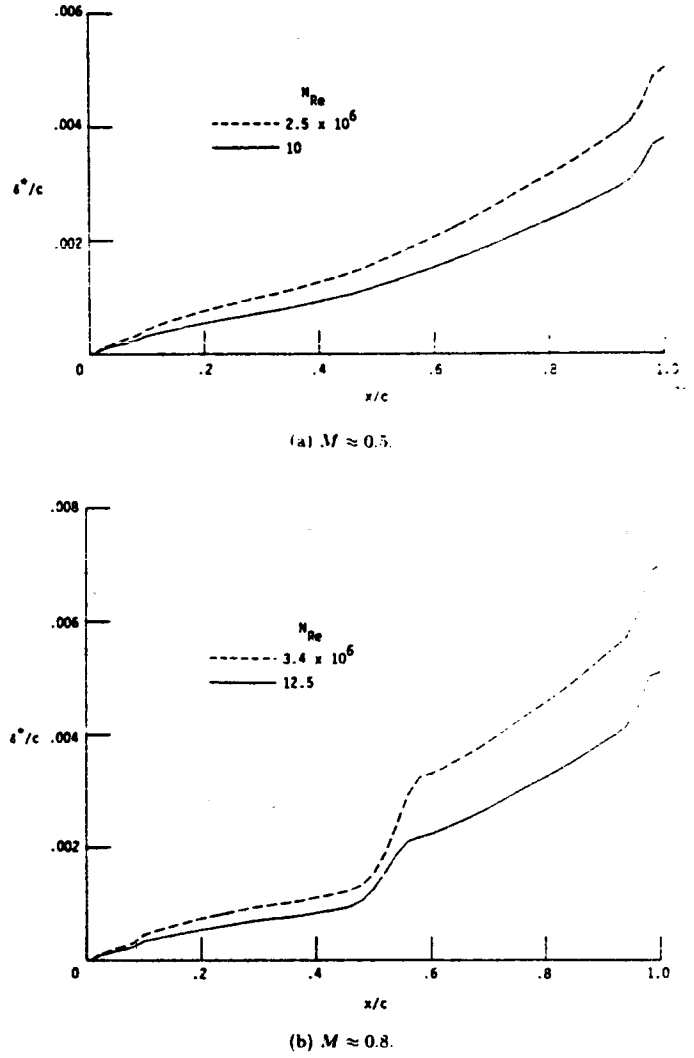

Fig. 33 Effect of Reynolds number on boundary-layer displacement thickness for NACA 64A010A airfoil in steady flow. (Howlett and Bland, Ref. 110).

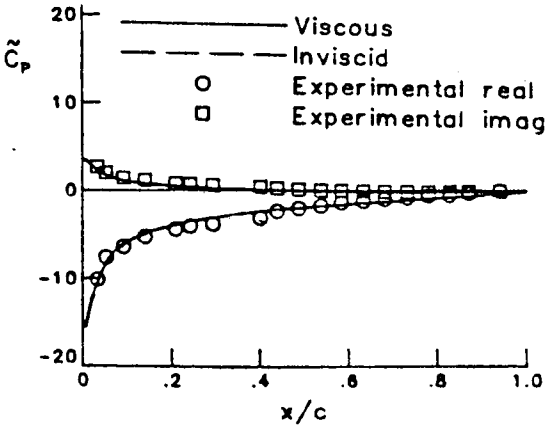

Fig. 34 Unsteady upper surface distribution for the NACA 64A010A airfoil at M = 0.5, $\alpha_0 = 1°$. (Howlett and Bland, Ref. 110)

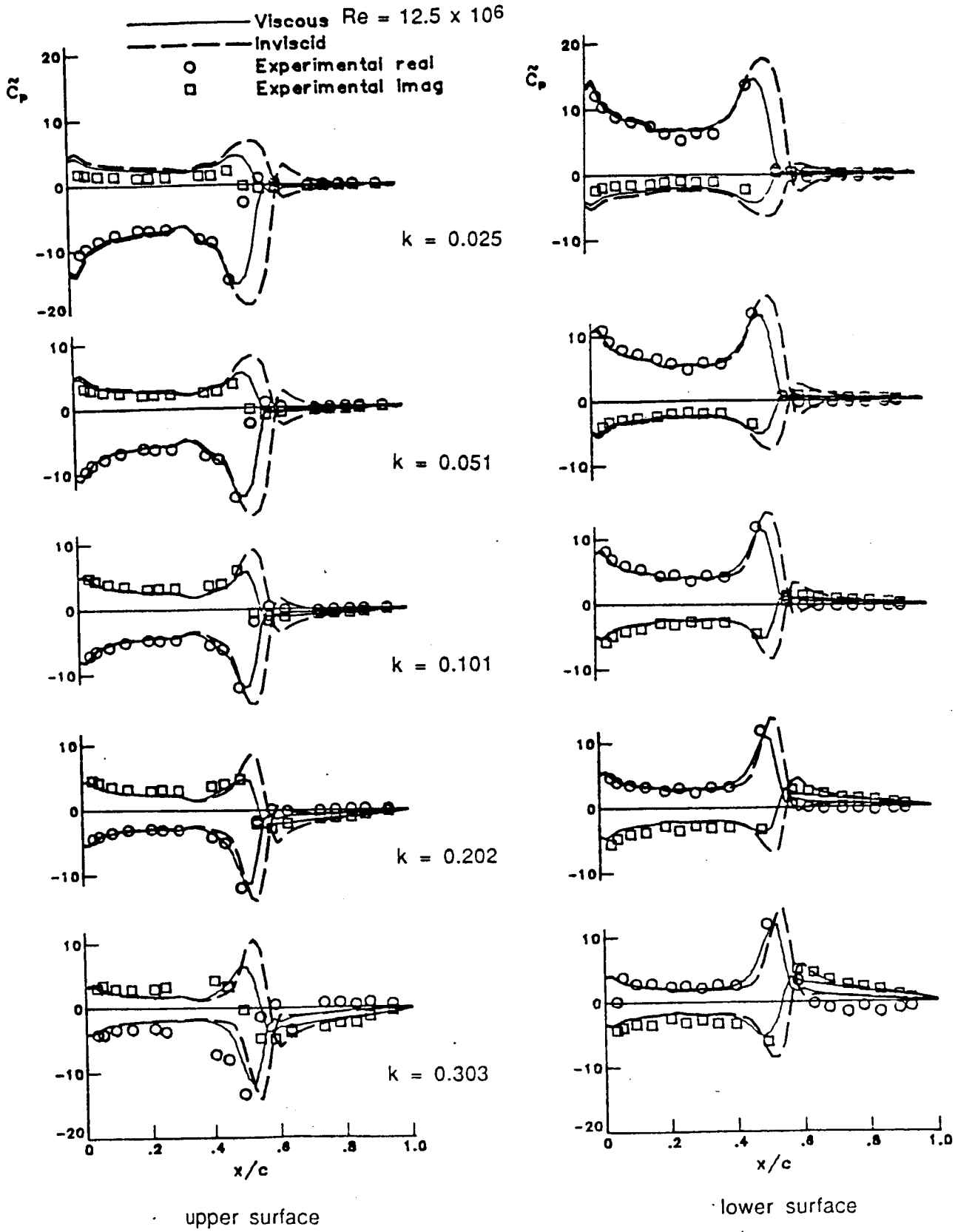

Fig. 35 - Unsteady pressure distributions for the NACA 64A010A airfoil at M = 0.796, $\alpha_o = 1°$.
(Howlett and Bland, Ref. 110)

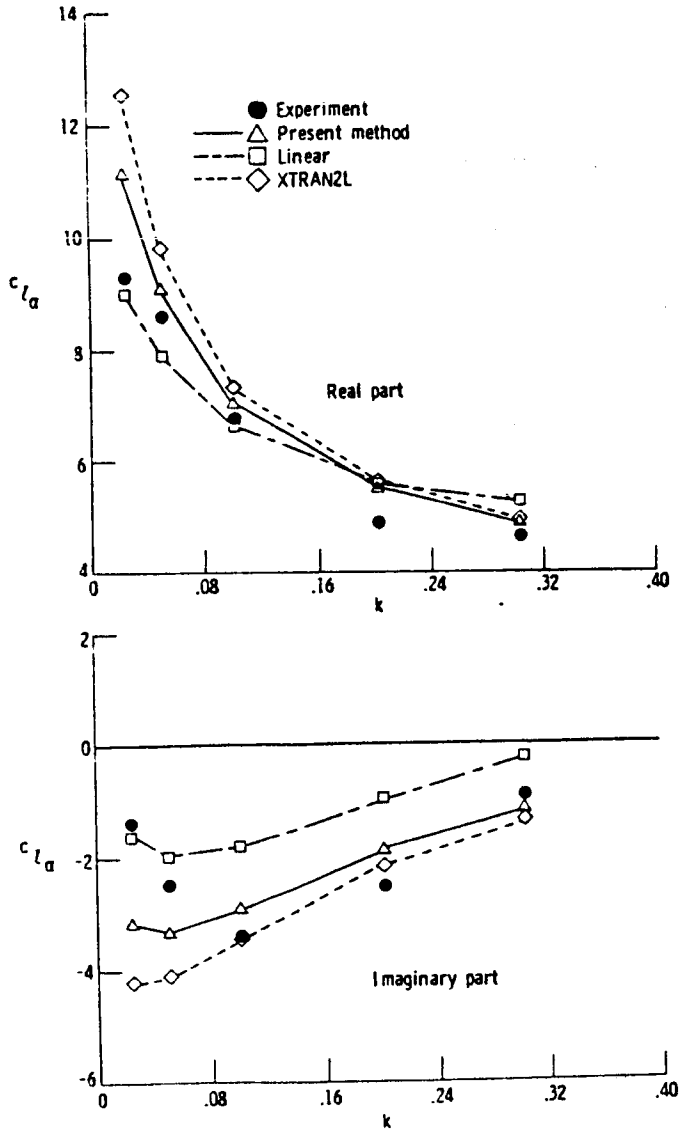

(a) Unsteady lift.

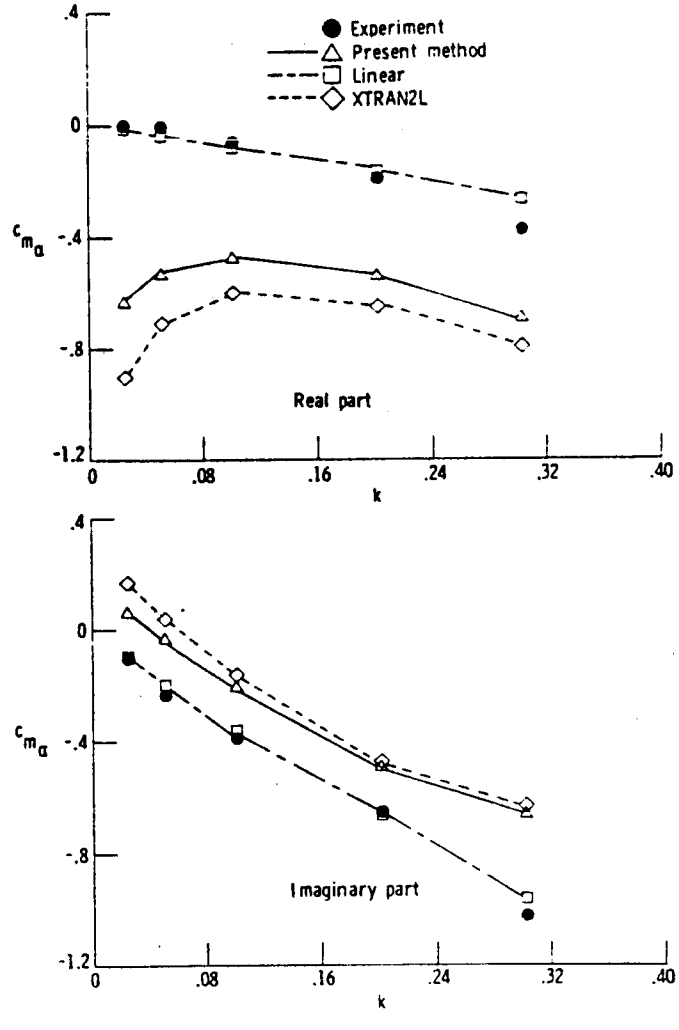

(b) Unsteady pitching moment.

Fig. 36 Comparison of unsteady forces for NACA 64A010A airfoil, M = 0.796; α_1 = 1°.

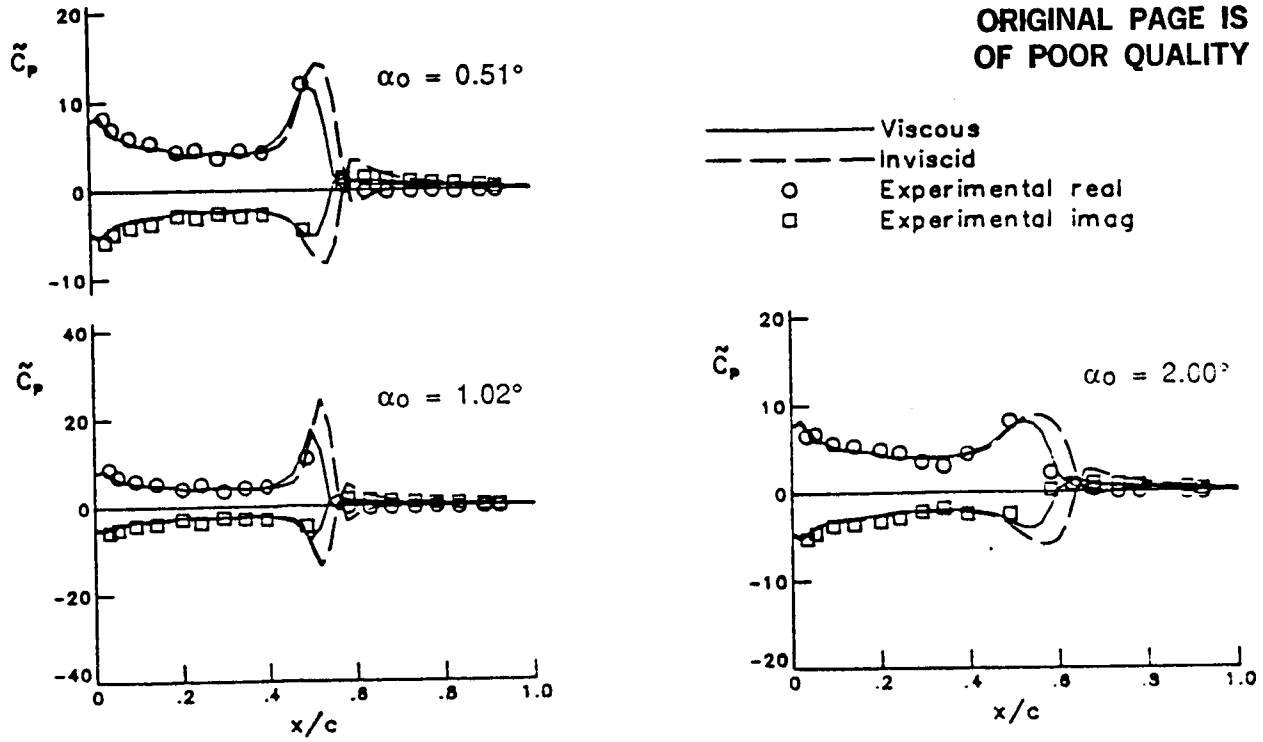

Fig. 37 Unsteady lower surface pressure distributions for the NACA 64A010A airfoil at M = 0.796 and k = 0.1.
(Howlett and Bland, Ref. 110).

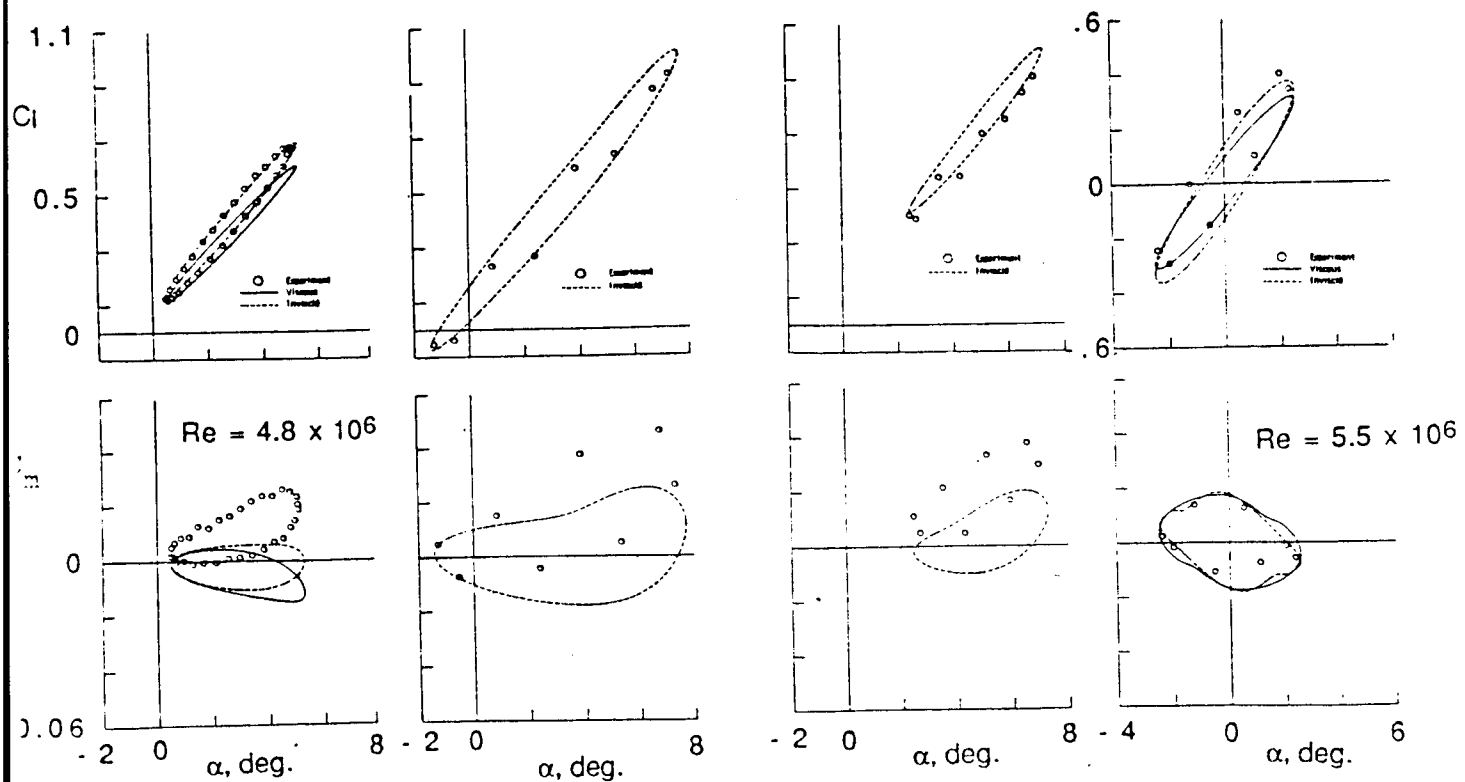

(a) Case 1. M = 0.601; (b) Case 2. M = 0.599; (c) Case 3. M = 0.599; (d) Case 5. M = 0.755;
α_m = 2.89°; α_o = 2.41° α_m = 3.16°; α_o = 4.59° α_m = 4.86°; α_o = 2.44° α_m = 0.02°; α_o = 2.51°

Fig. 38 Comparison of unsteady forces versus angle of attack for cases 1, 2, 3, and 5 for the NACA 0012 airfoil at k = 0.081 and Re = 4.8 x 10⁶. (Howlett and Bland, Ref. 110)

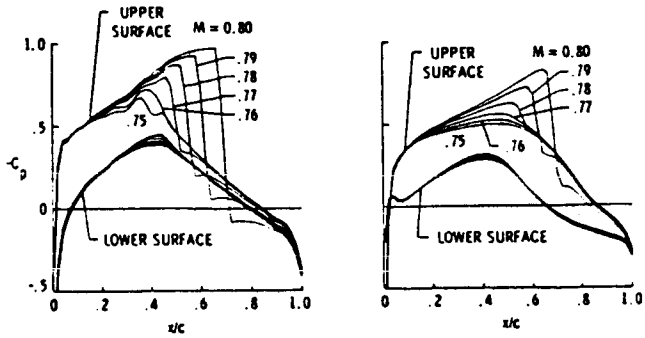

(a) NACA 64A010A $\alpha m = 1°$. (b) MBB-A3 $\alpha m = -0.5°$.

Fig. 39 Steady pressure distributions.
(Bland and Edwards, Ref. 114)

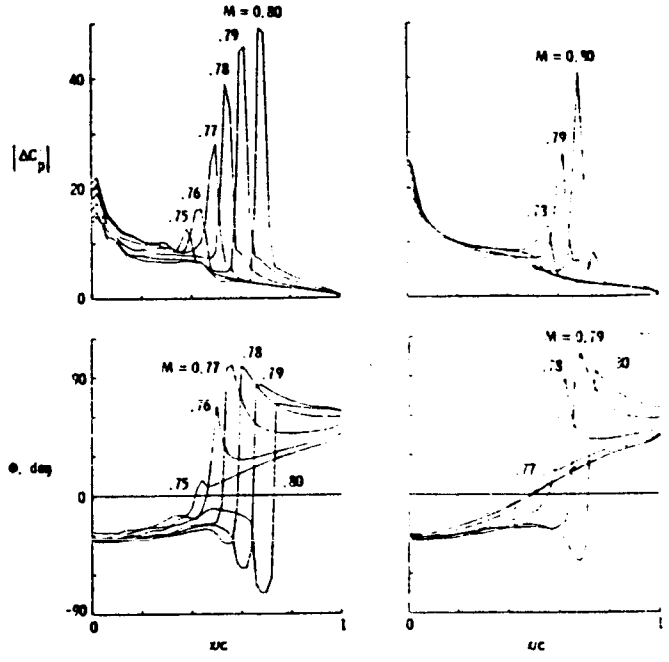

(a) NACA 64A010A (b) MBB-A3

Fig. 40 Lifting pressure due to pitch about quarter chord at k = 0.15.
(Bland and Edwards, Ref. 114)

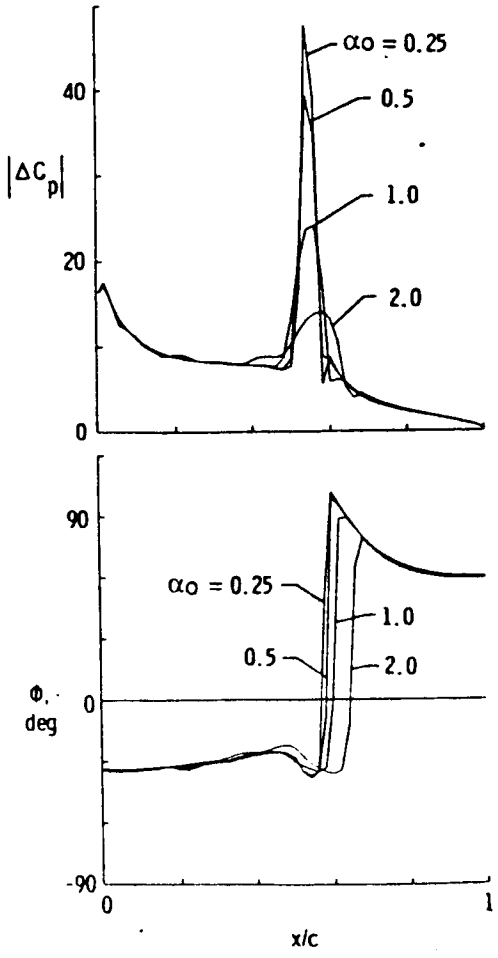

Fig. 42 Pitch amplitude effect for NACA 64A010A airfoil at M = 0.78, k = 0.15.
(Bland and Edwards, Ref. 114)

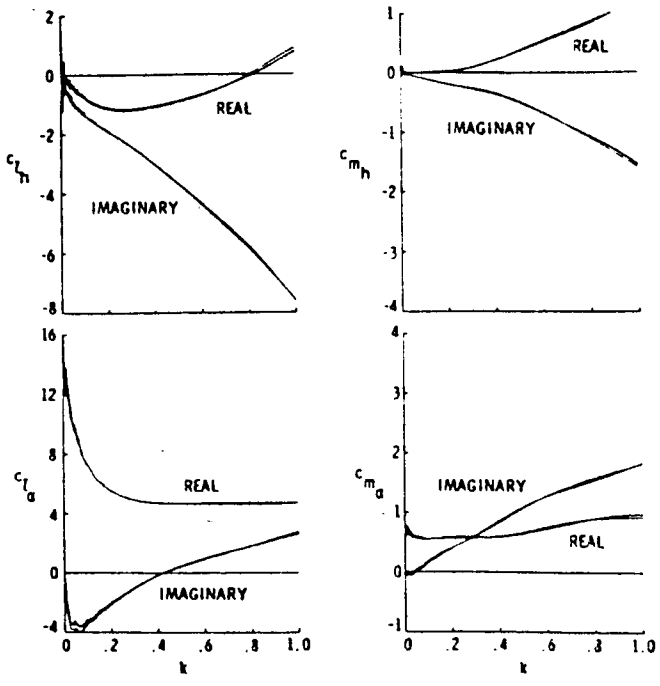

(a) Force coefficients. (b) Moment coefficien

Fig. 41 Comparison of unsteady aerodynamic forces for NACA 64A010A airfoil at M = 0.78 and MBB-A3 airfoil at M = 0.79.
(Bland and Edwards, Ref. 114)

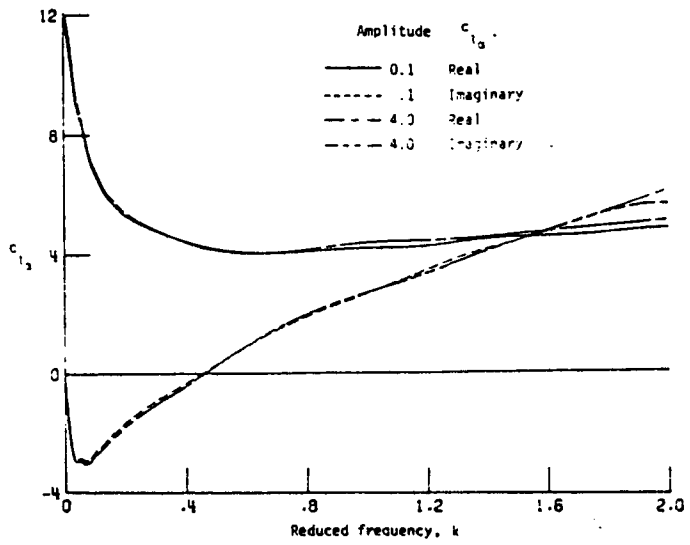

Fig. 43 Effect of pulse amplitude on lift coefficient for NACA 64A010A airfoil. M = 0.796; α_m = -0.21°.
(Howlett and Bland, Ref. 110)

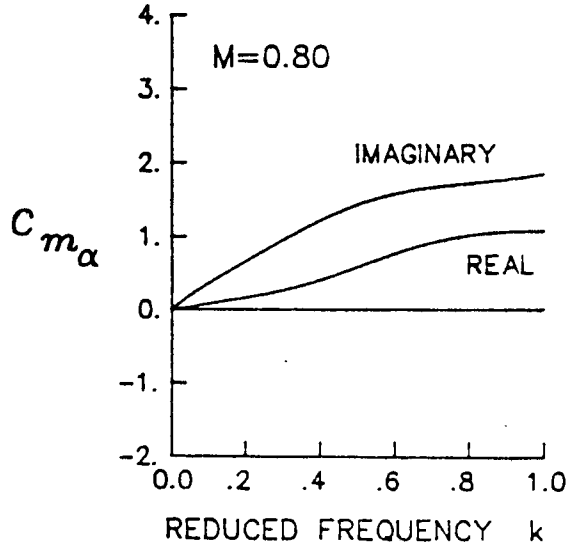

Fig. 44 Pitching-moment coefficient due to pitch computed using subsonic linear theory at M = 0.80.
(Batina, Ref. 108).

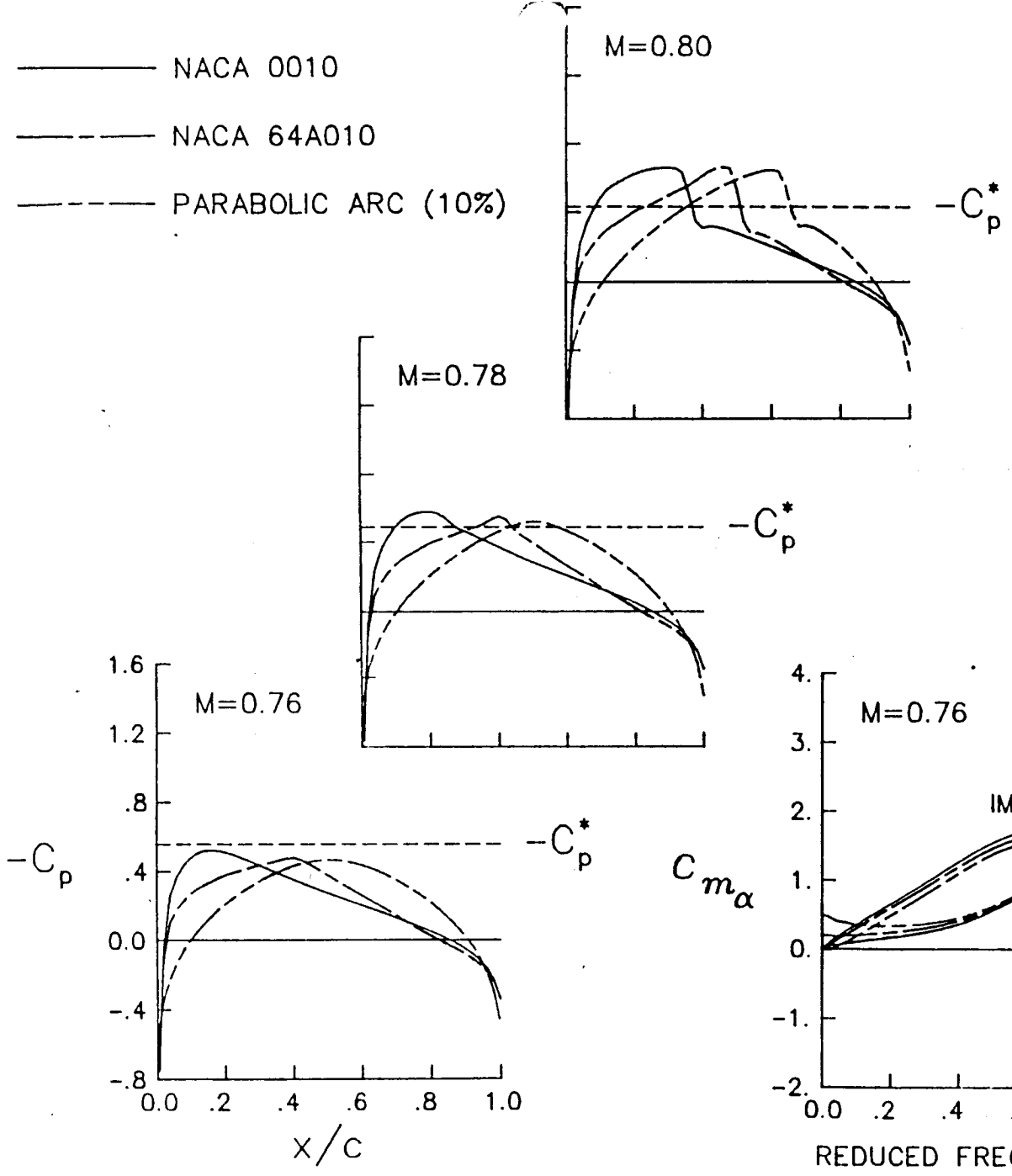

Fig. 45 Steady pressure distributions for three airfoil shapes at $\alpha_m = 0°$.
(Batina, Ref. 108)

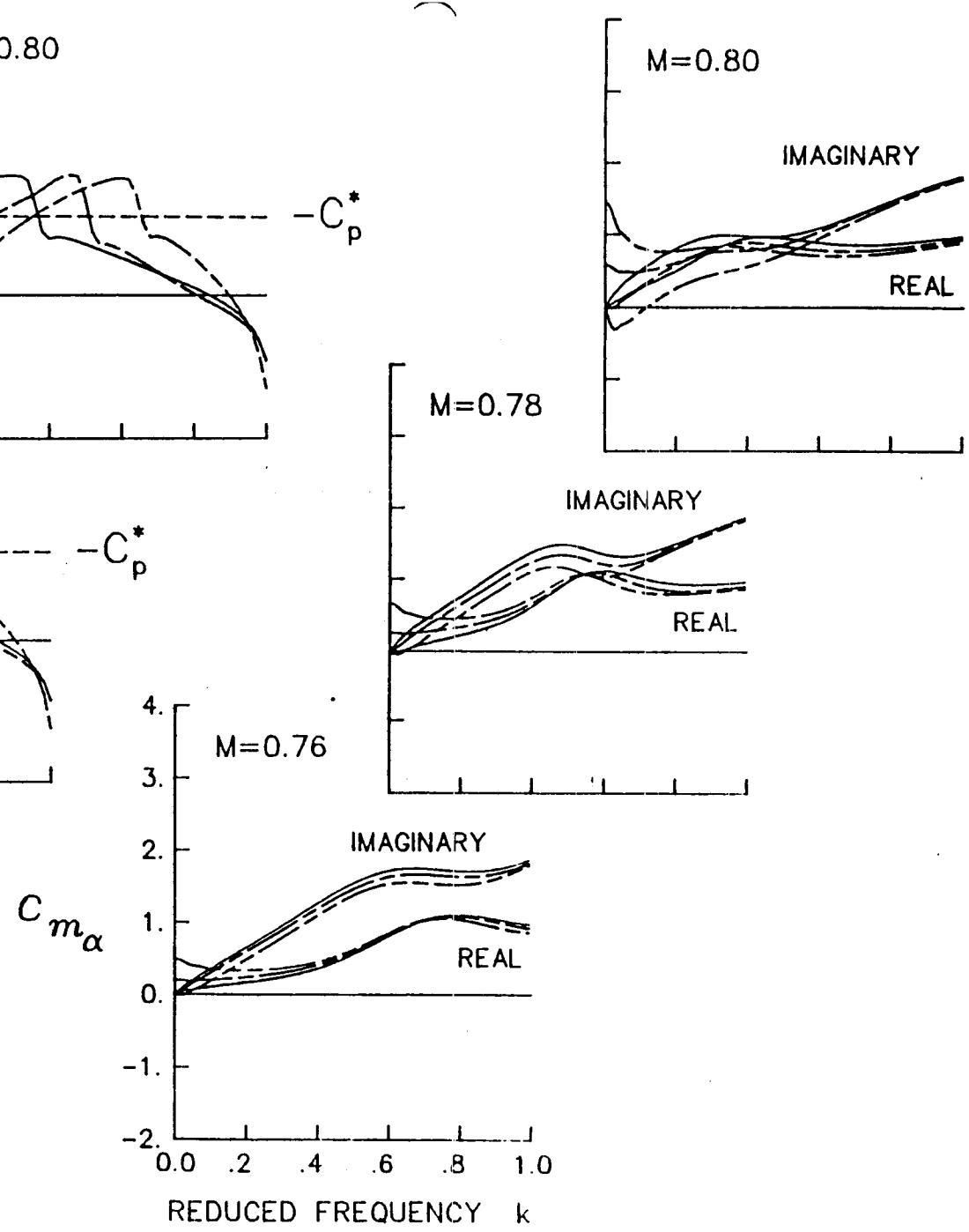

Fig. 46 Unsteady frequency response functions for three airfoils at $\alpha_m = 0°$.
(Batina, Ref. 108)

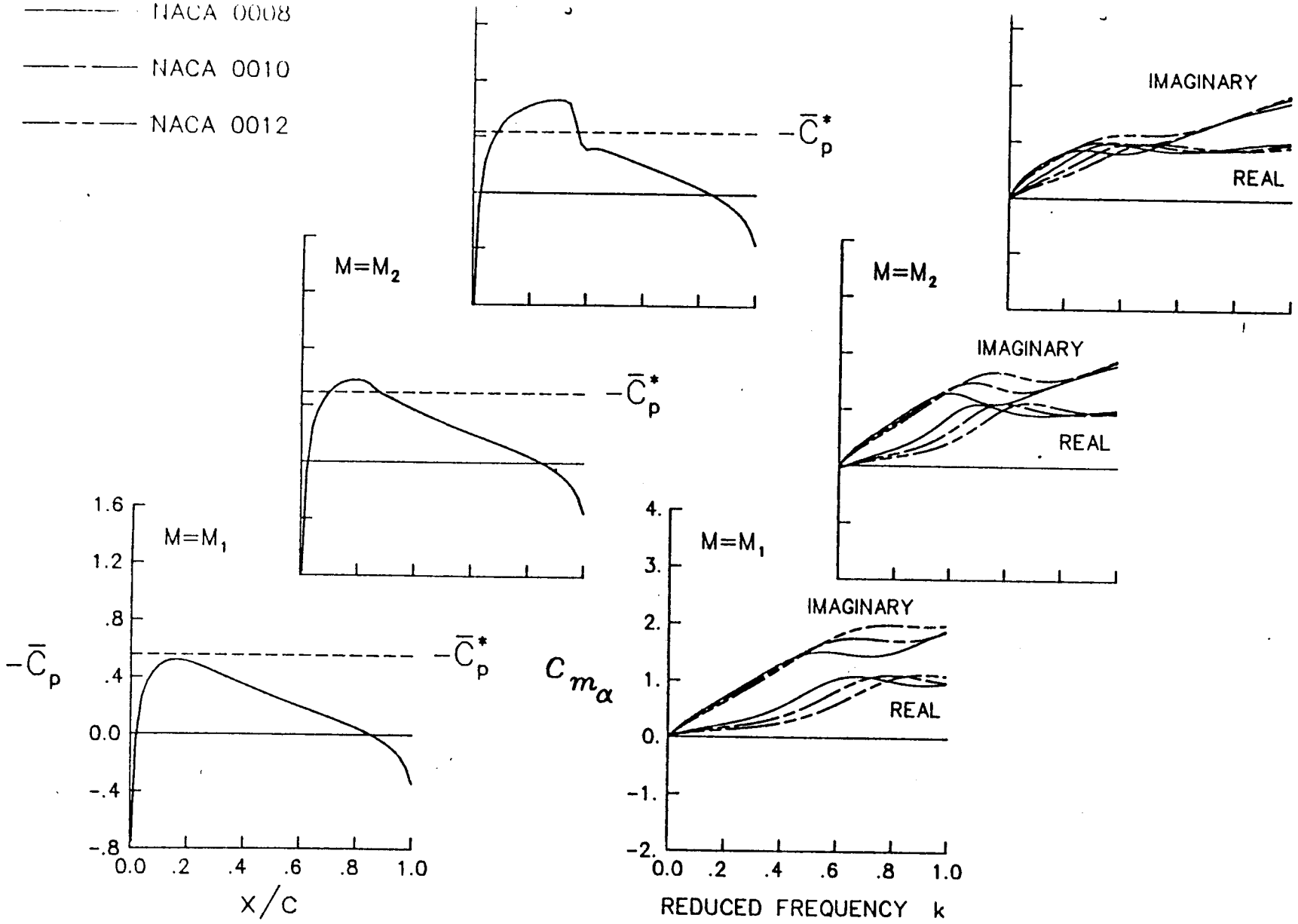

Fig. 47 Steady pressure distributions for three airfoil thicknesses at three transonically scaled Mach numbers at $\alpha_m = 0°$.
(Batina, Ref. 108)

Fig. 48 Thickness effect on unsteady frequency response functions for three transonically scaled Mach numbers.
(Batina, Ref. 108)

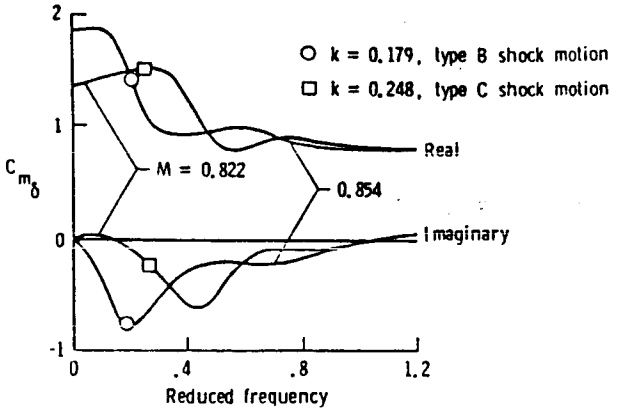

Fig. 49 Pitching moment coefficient due to flap motion for the NACA 64A006 airfoil. (Edwards and Thomas, Ref. 1)

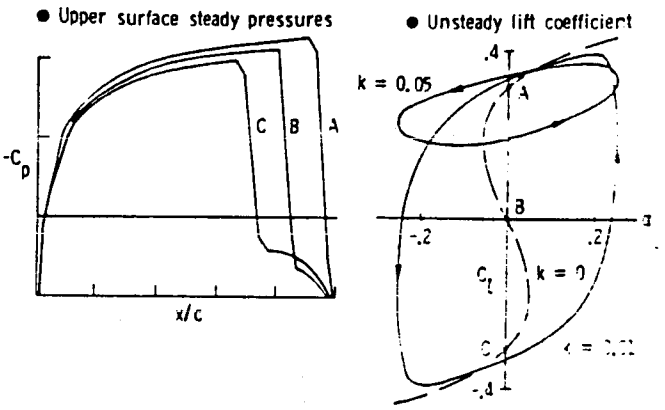

(a) Steady. (b) Unsteady.

Fig. 51 Anomalous behavior of potential flow solutions for NACA 0012 airfoil at M = 0.85, α_m = 0°. (Williams et al., Ref. 118)

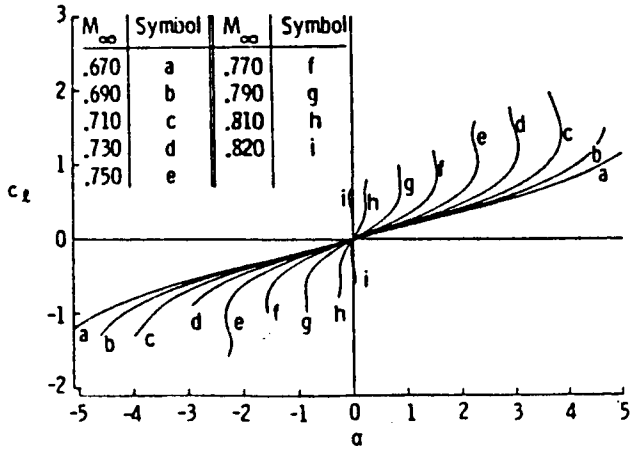

Fig. 50 Lift-curve for NACA 0012 airfoil computed with FLO36 code versus angle-of-attack as a function of Mach number. (Salas and Gumbert, Ref. 116)

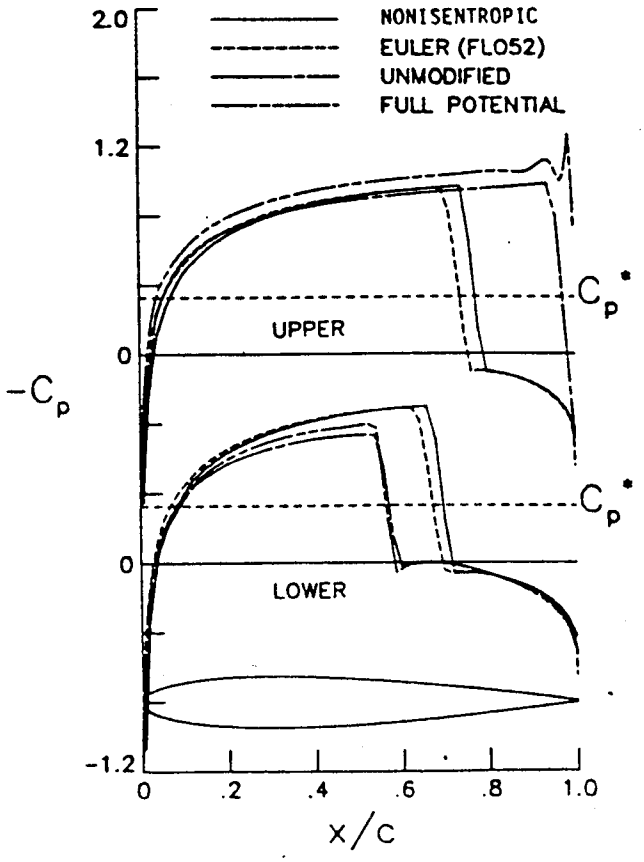

Fig. 52 Steady pressure distribution for NACA 0012 airfoil at M = 0.84, α_m = 0.25°. (Fuglsang and Williams, Ref. 119)

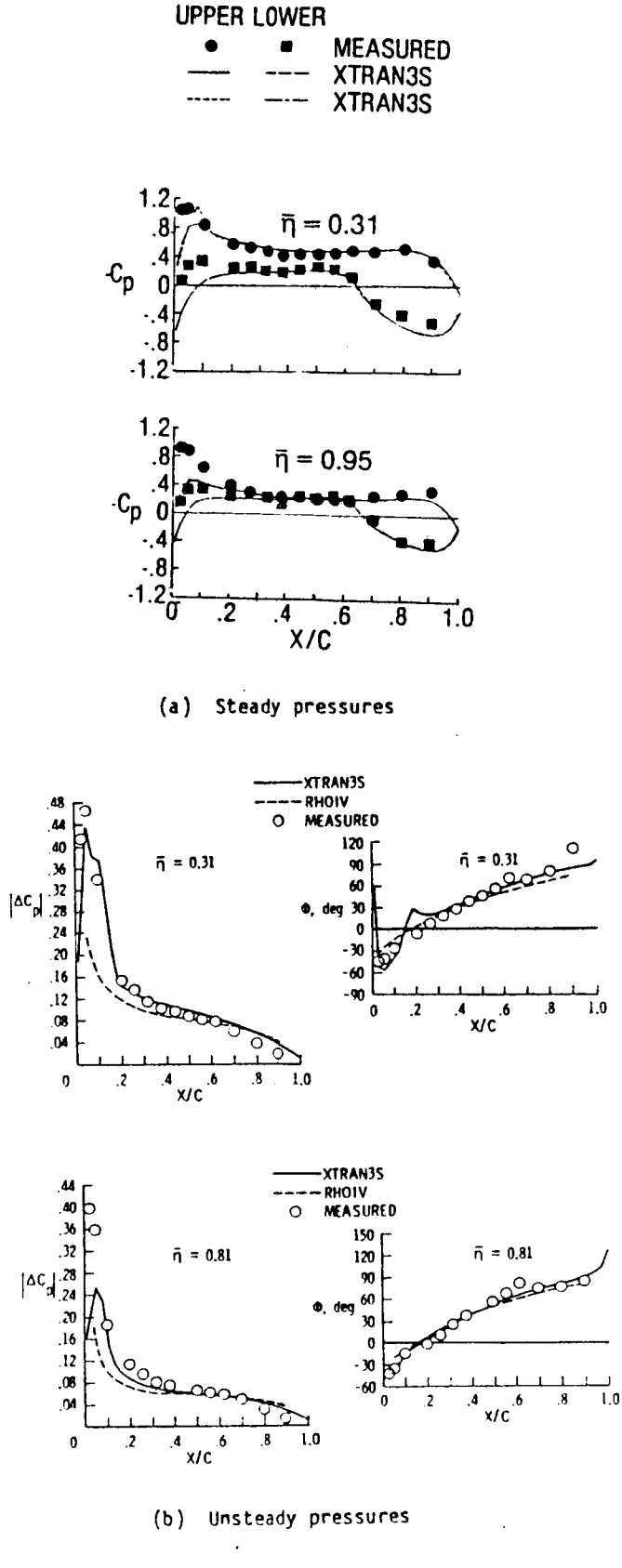

Fig. 53 Comparison of measured and calculated steady and unsteady pressures for the NASA rectangular supercritical wing. (Seidel et al., Ref. 109)

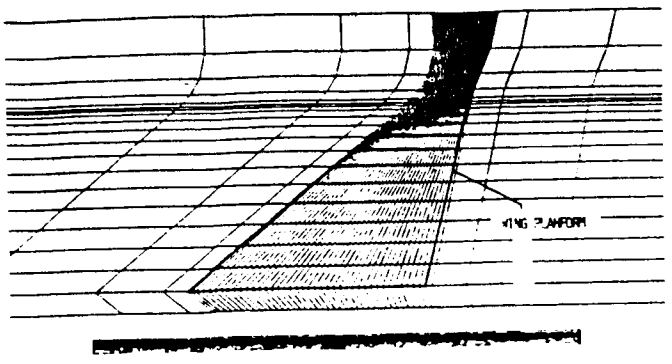

Fig. 54 Finite-difference grid in the plane of the wing and near- and far-field views. (Bennett et al., Ref. 120)

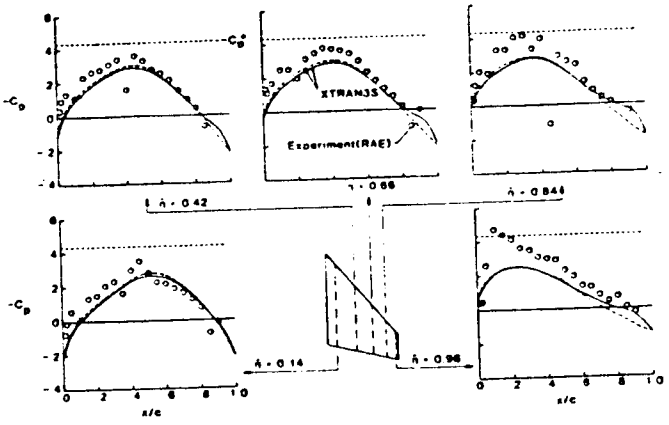

Fig. 55 Measured and calculated steady pressures for RAE tailplane model at M = 0.80. (Bennett et al. Ref. 120)

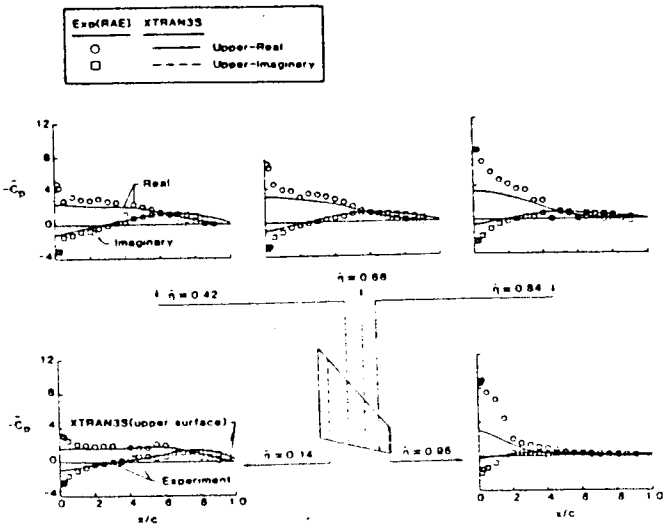

Fig. 56 Measured and calculated unsteady pressure distributions for RAE tailplane model oscillating at approximately 70 Hz, M = 0.80, k = 0.490. (Bennett et al., Ref. 120).

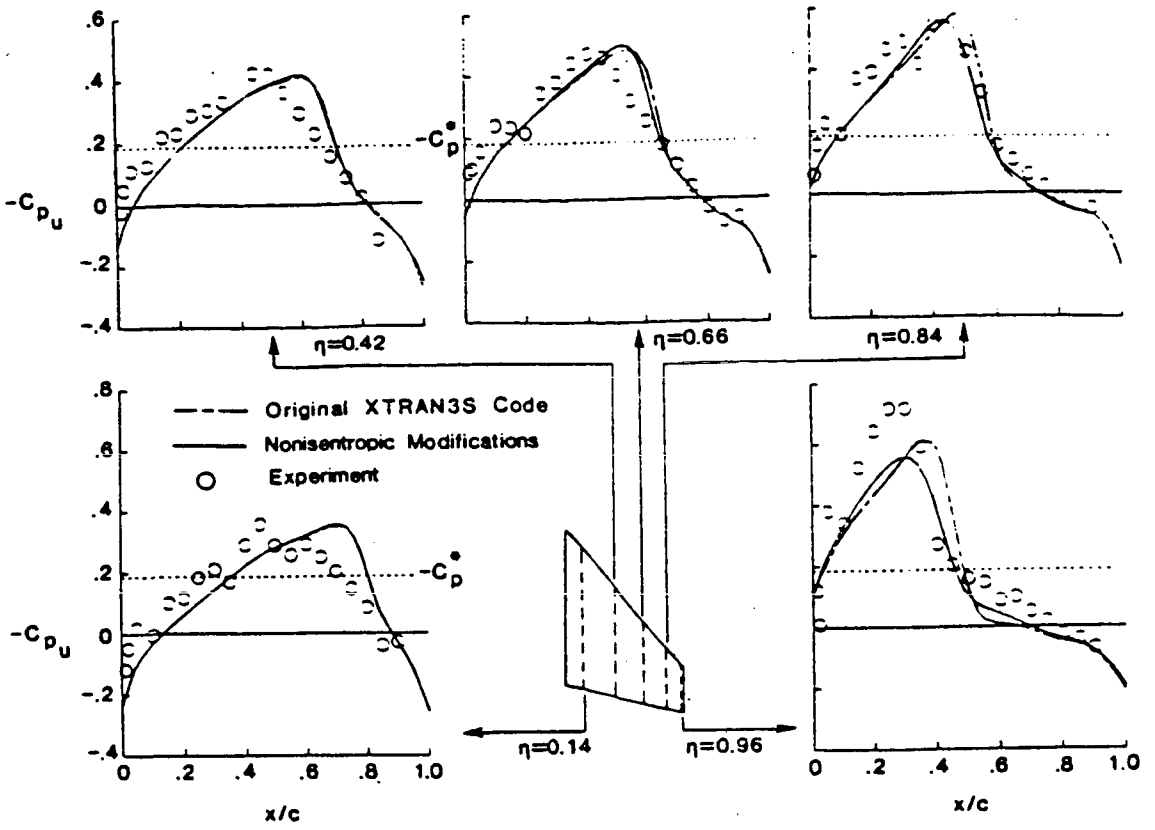

Fig. 58 Steady pressure distribution for the RAE tailplane model at M = 0.90, αm = -0.3°. (Gibbons et al., Ref. 122)

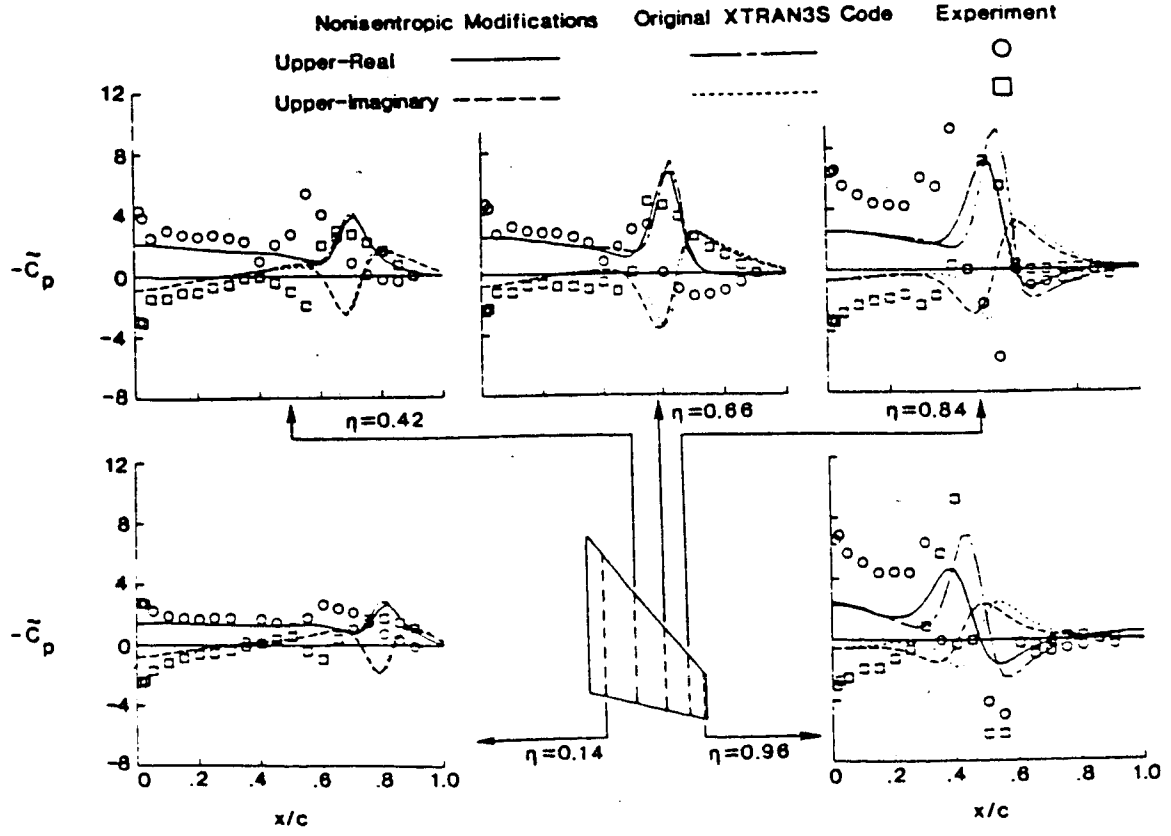

Fig. 59 Unsteady pressure distribution for the RAE tailplane model at M = 0.90, αm = -0.3°. (Gibbons et al., Ref. 122)

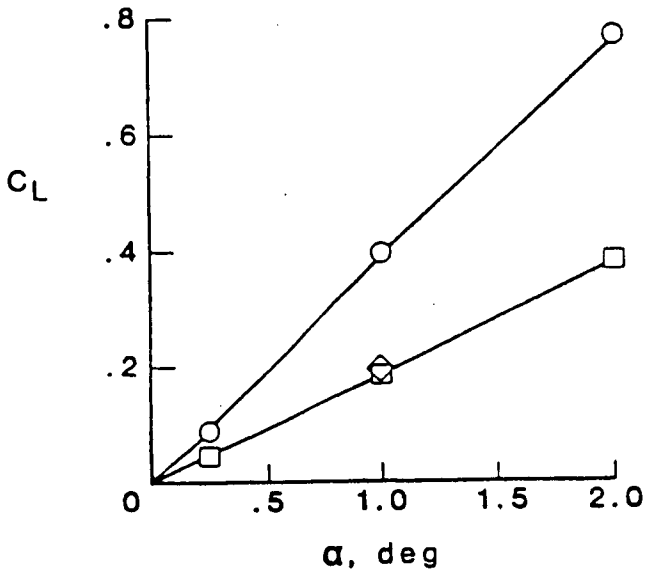

Fig. 57 Total lift coefficient for NACA 0012 wing with AR = 12 at M = 0.82. (Gibbons et al., Ref. 122).

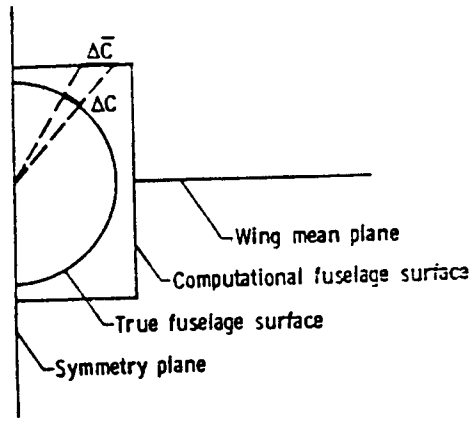

Fig. 61 Wing-fuselage modeling for TSD potential equation. (Batina, ref. 124)

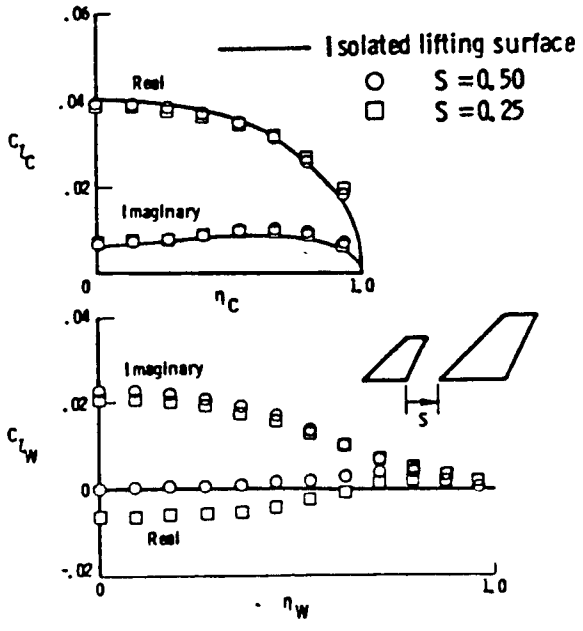

Fig. 60 Unsteady sectional lift coefficient on canard/wing configurations at M = 0.9, α_m = 2 deg and k = 0.3. (Batina, ref. 123)

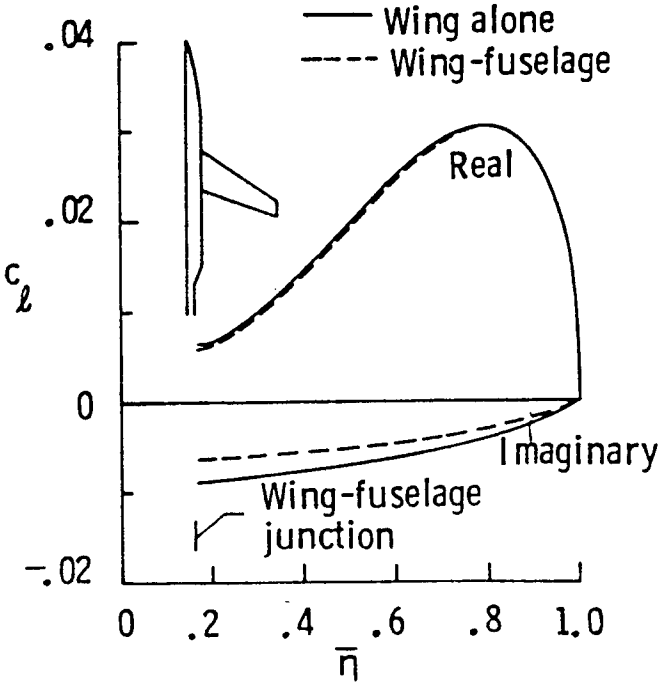

Fig. 63 Unsteady sectional coefficients due to wing first bending for the RAE wing-fuselage at M = 0.91, and $\alpha_w = \alpha_f = 1°$.

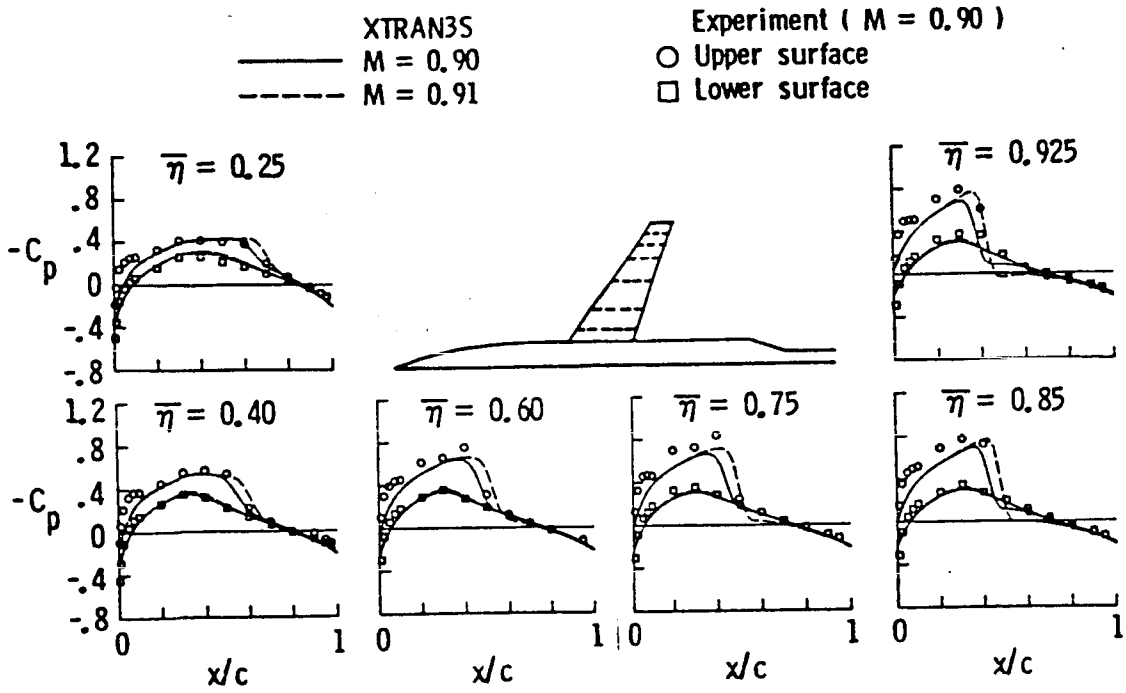

Fig. 62 Comparison between XTRAN3S and experimental wing steady pressure distributions on the RAE wing-fuselage at M = 0.90, 0.91, and $\alpha w = \alpha f = 1°$. (Batina, ref. 124)

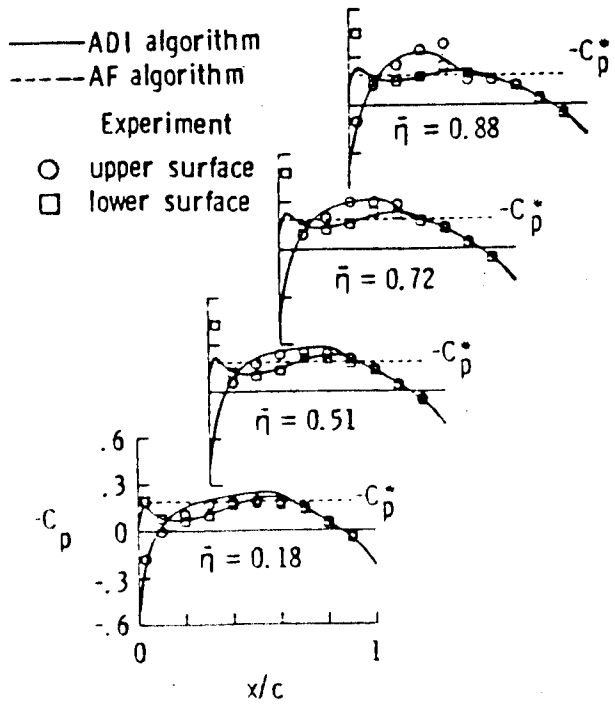

Fig. 64 Comparison of F-5 wing steady pressure distributions at M = 0.9 and $\alpha m = 0°$.

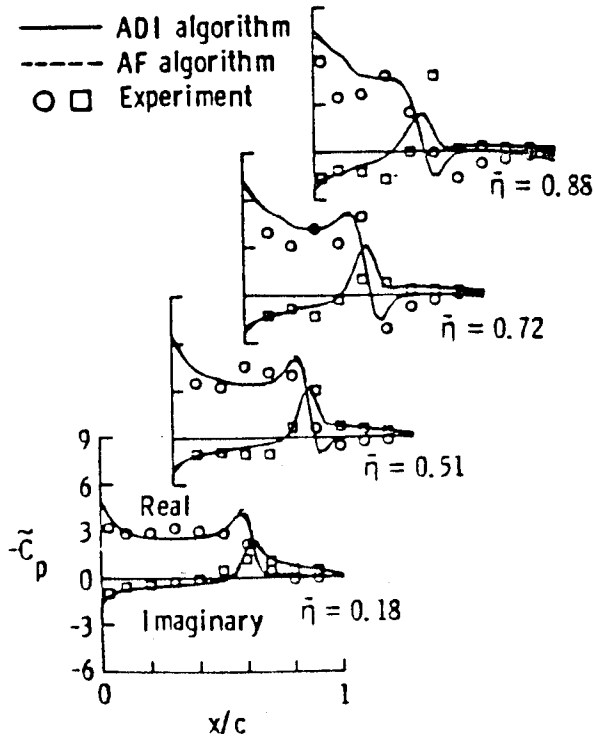

Fig. 65 Comparison of F-5 wing upper surface unsteady pressure distributions due to wing pitching at M = 0 $\alpha m = 0°$, $\alpha o = 0.109°$, and k = 0.137.

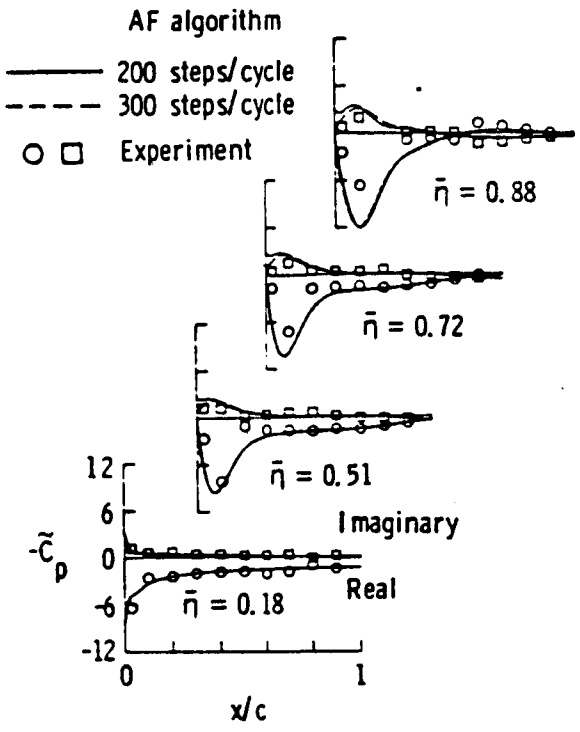

ig. 66 Comparison of F-5 wing lower surface unsteady pressure distributions due to wing pitching at M = 1.1, α_m = 0°, α_o = 0.267°, and k = 0.116.

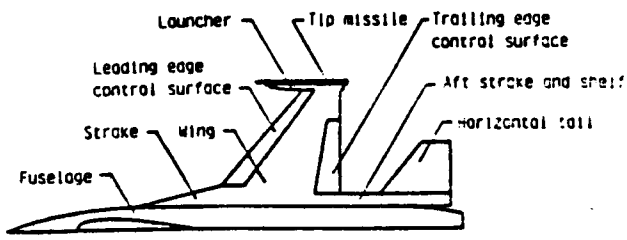

Fig. 67 CAP-TSD modeling of the General Dynamics one-ninth scale F-16C aircraft model. (Batina, et al., ref. 85)

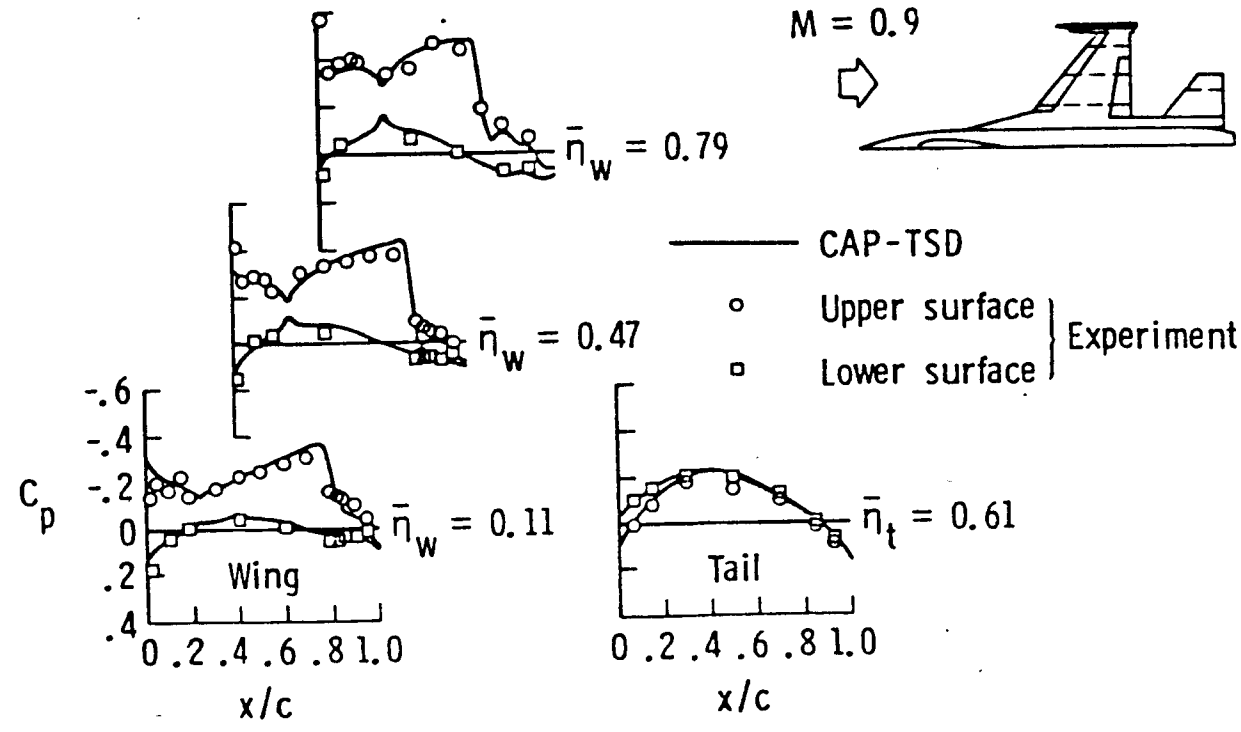

Fig. 68 Comparison between CAP-TSD and experimental steady pressure distributions on the wing and tail of the F-16C aircraft model at M = 0.9 and α_m = 2.38°. (Batina, et al., ref. 85)

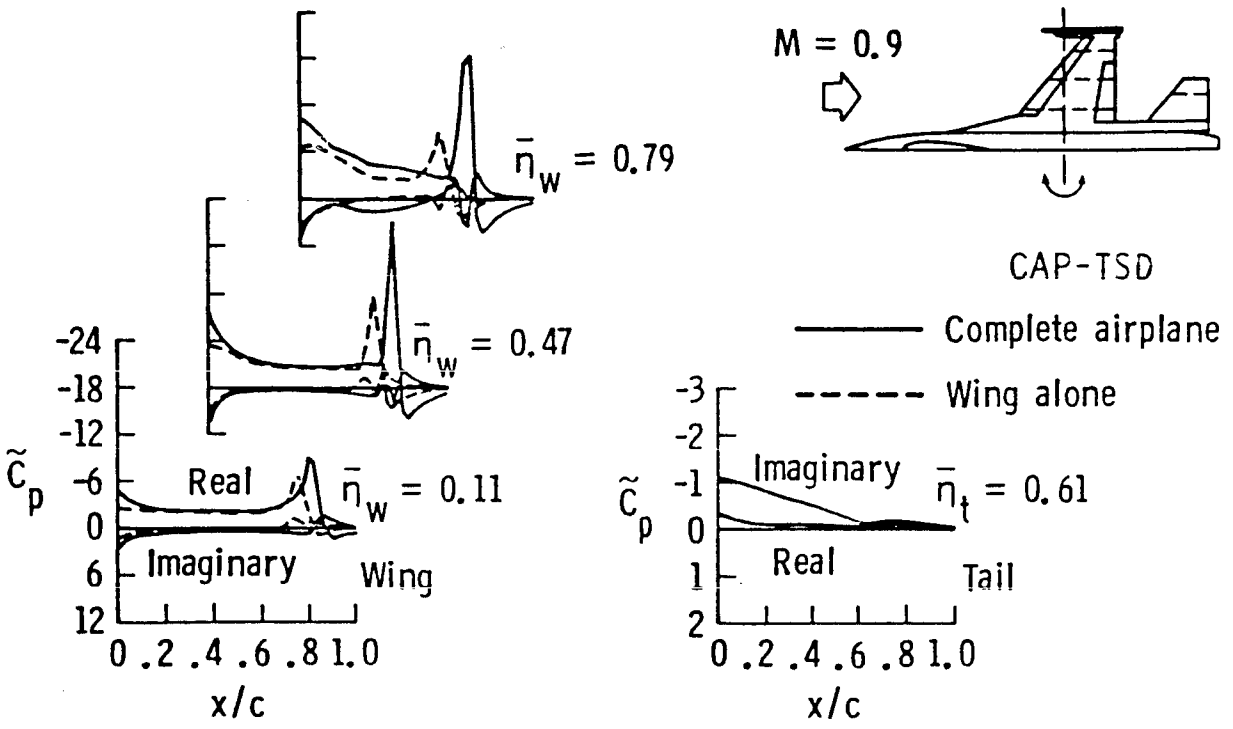

Fig. 69 CAP-TSD unsteady pressure distributions on the upper surfaces of the wing and tail of the F-16C aircraft model due to complete airplane rigid pitching at M = 0.9, α_m = 2.38°, α_o = 0.5°, and k = 0.1.
(Batina, et al., ref. 85)

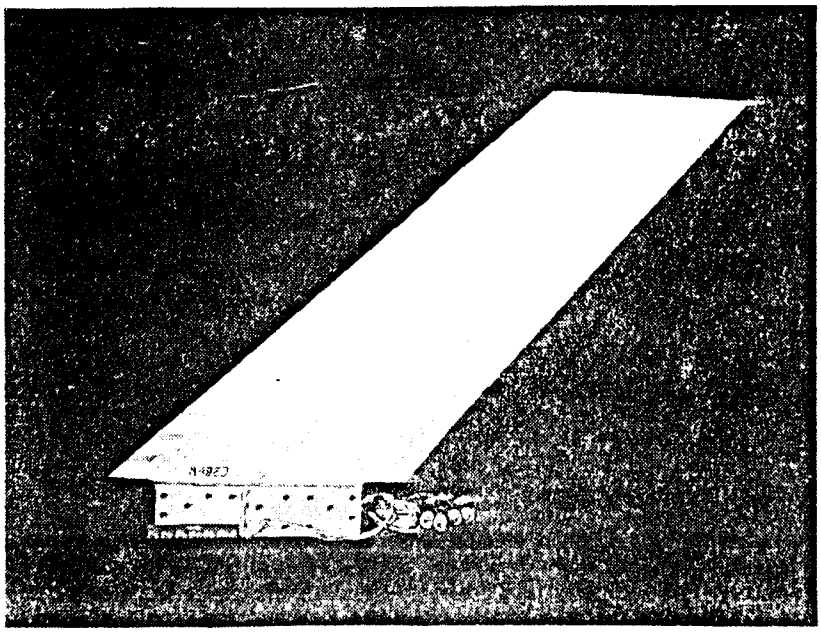

Fig. 70 Planview of 45° sweptback flutter model wing.
(Cunningham et al., ref. 127)

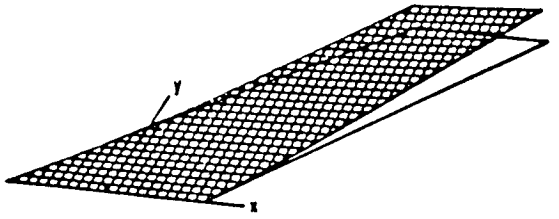

(a) Mode 1, f_1 = 9.60 Hz

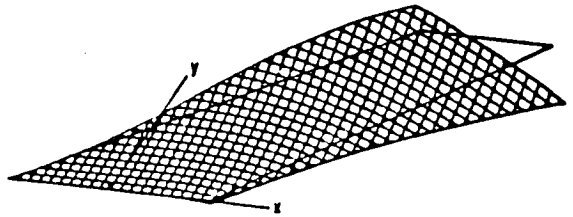

(b) Mode 2, f_2 = 38.17 Hz

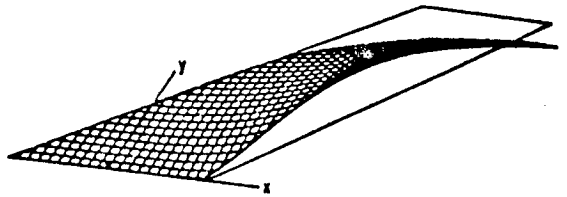

(c) Mode 3, f_3 = 48.35 Hz

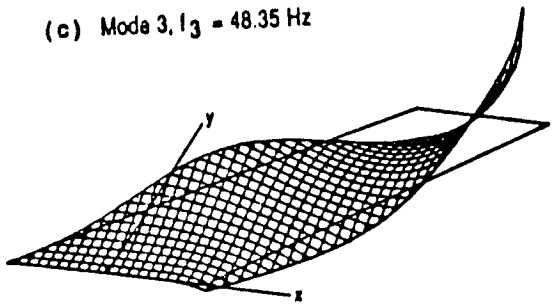

(d) Mode 4, f_4 = 91.54 Hz

Fig. 71 Oblique projections of natural vibration modes of 45° sweptback wing.
(Cunningham, et al., ref. 127)

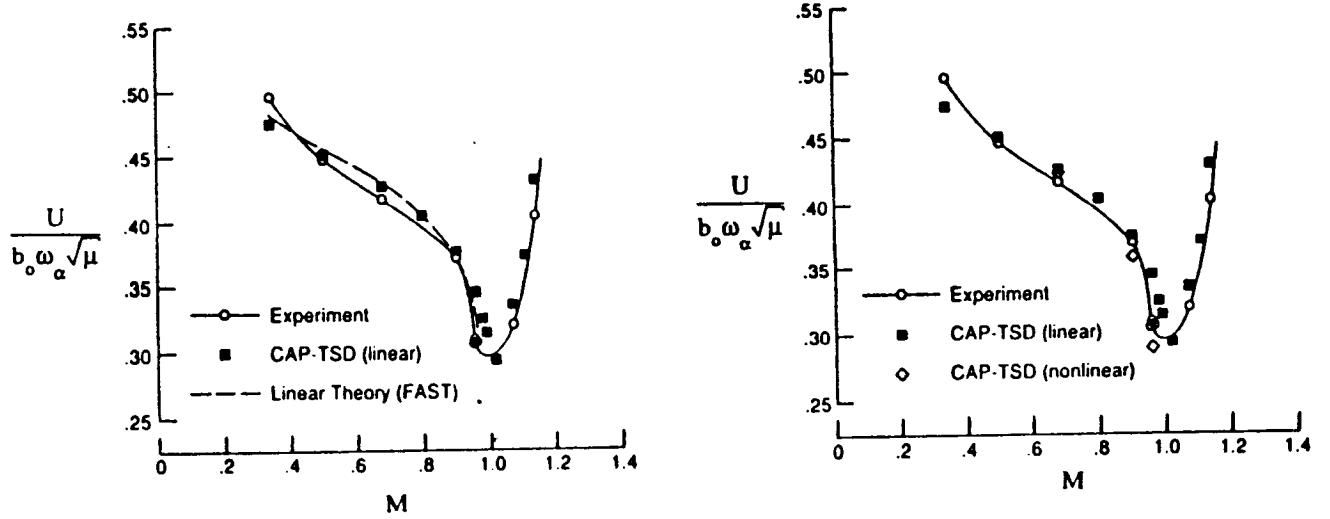

(a) flutter speed index versus Mach number.

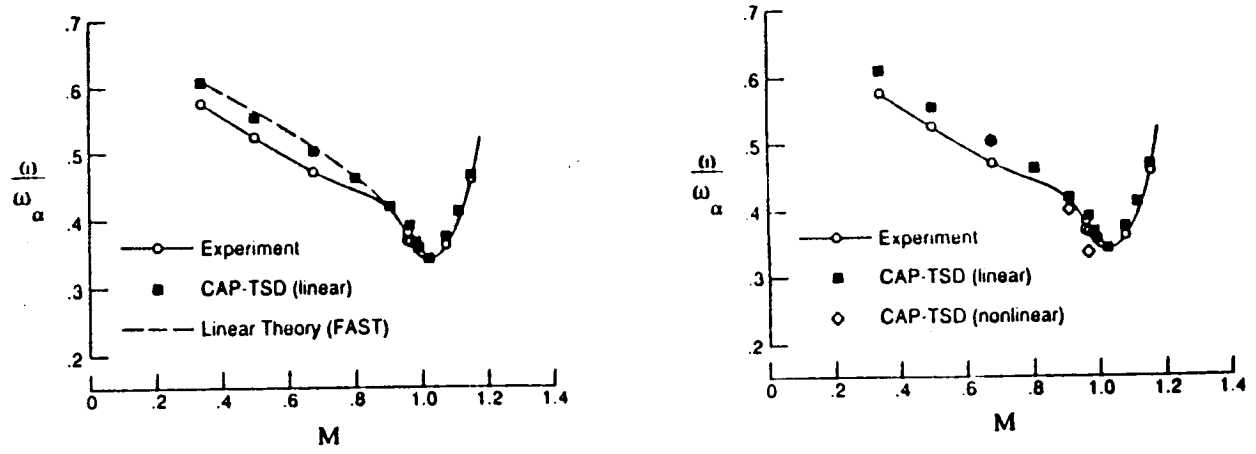

(b) nondimensional flutter frequency versus Mach number.

Fig. 72 Comparisons of linear and nonlinear CAP-TSD flutter predictions with experimental data for the 45° sweptback wing.
(Cunningham, et al., ref. 127)

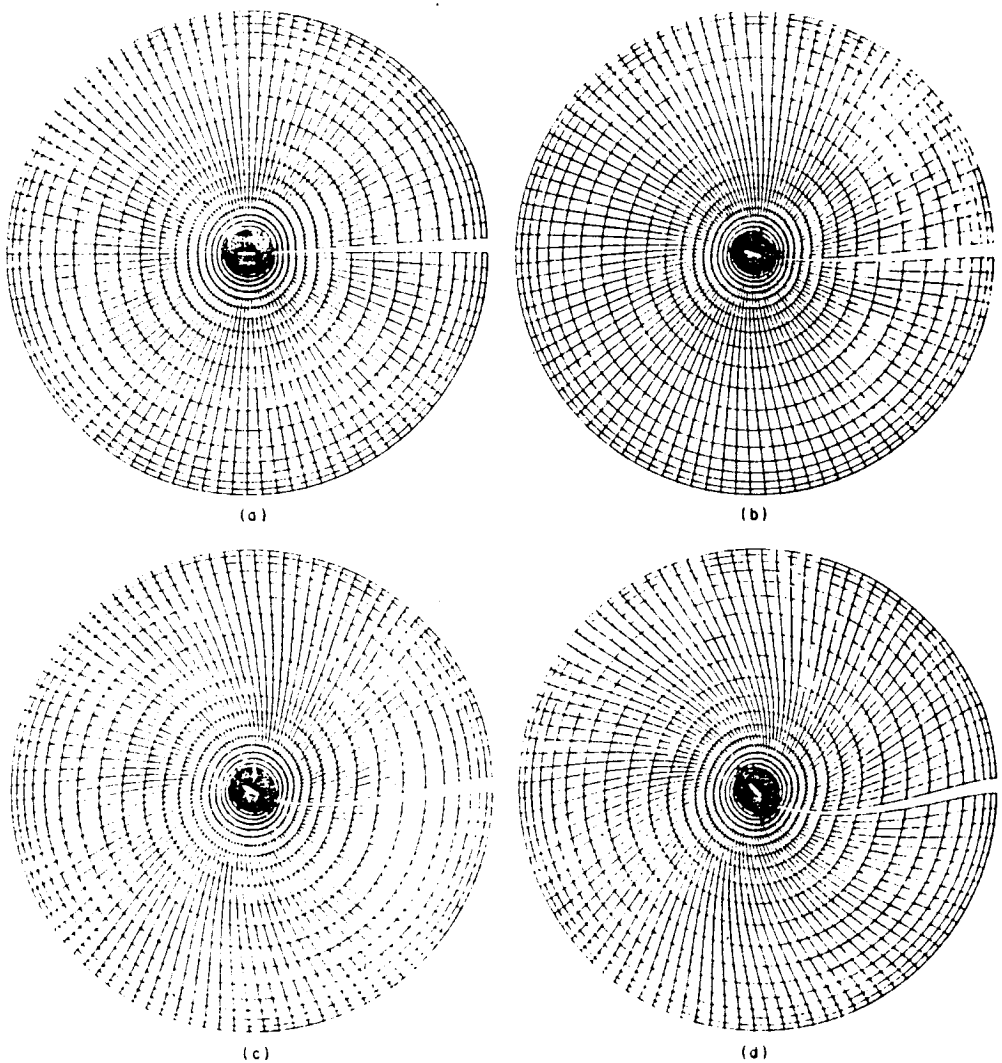

Fig. 73 Example of grid interpolation. (a) Calculated grid, $\alpha = 0°$. (b) Interpolated grid, $\alpha = 15°$. Interpolated grid, $\alpha = 30°$, (d) Calculated grid, $\alpha = 45°$. (Whitlow, et al., ref. 82)

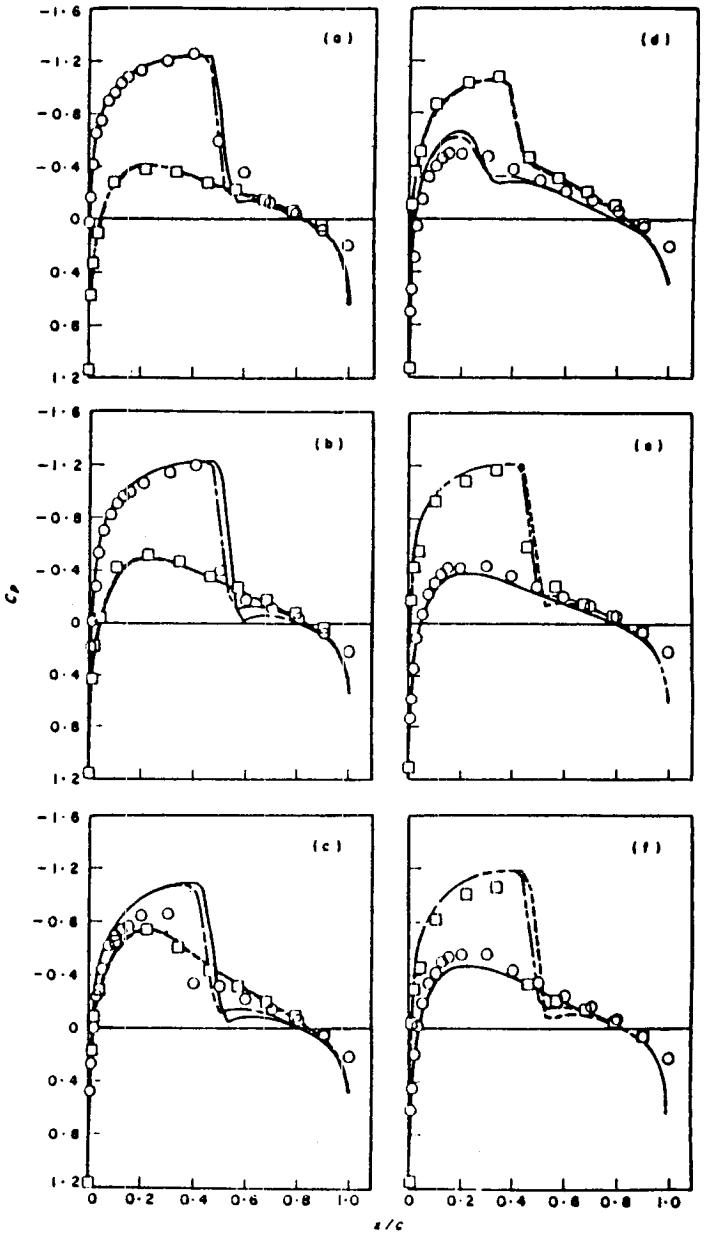

Fig. 74 Isentropic and nonisentropic unsteady pressures versus experiment for a NACA 0012 airfoil oscillating in pitch, $M_\infty = 0.755$, $\alpha(t) = 0.016° + 2.51 \sin(kt)$. (a) $\alpha(t) = 2.01°$, $kt = 127°$; (b) $\alpha(t) = 0.52°$, $kt = 168°$; (c) $\alpha(t) = -1.25°$, $kt = 210°$; (d) $\alpha(t) = -2.41°$, $kt = 255°$; (e) $\alpha(t) = -2.00°$, $kt = 307°$; (f) $\alpha(t) = -0.54°$, $kt = 347°$. ○: experiment upper; □: experiment lower; ——: isentropic upper; - - -: isentropic lower; ——: nonisentropic upper; - - -: nonisentropic lower.

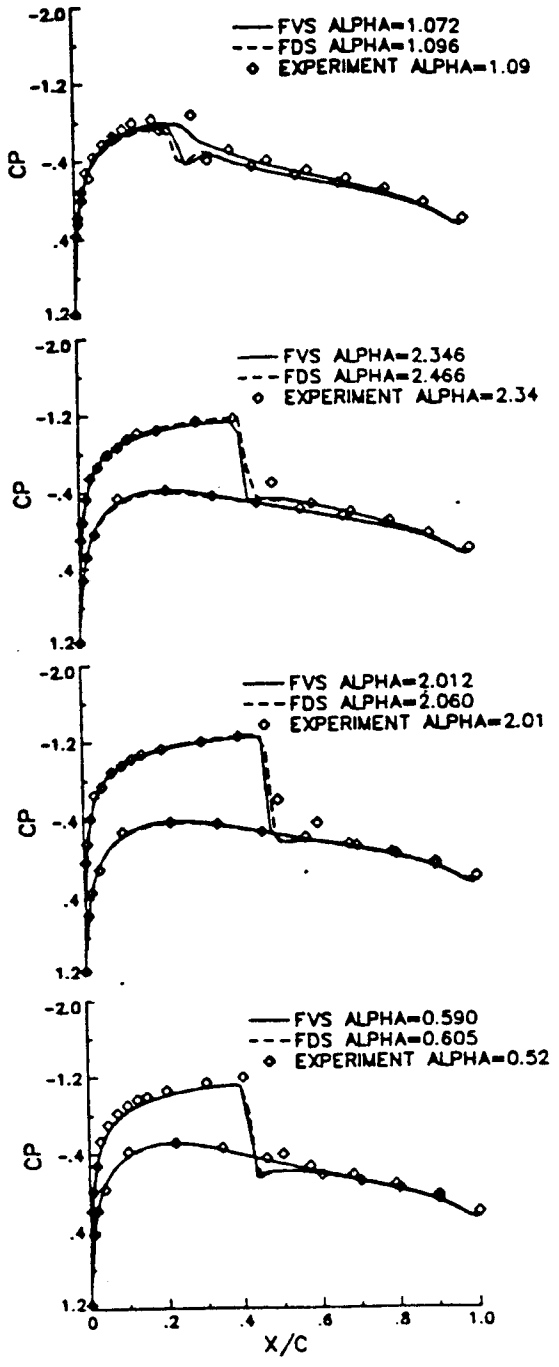

Fig. 75 Pressure distribution vs. esperiment for positive angles of pitching cycle; NACA 0012, $M = 0.755$, $k = 0.0814$, $\alpha_m = 0.016°$, $\alpha_0 = 2.51°$.
(Anderson et al., Ref. 81)

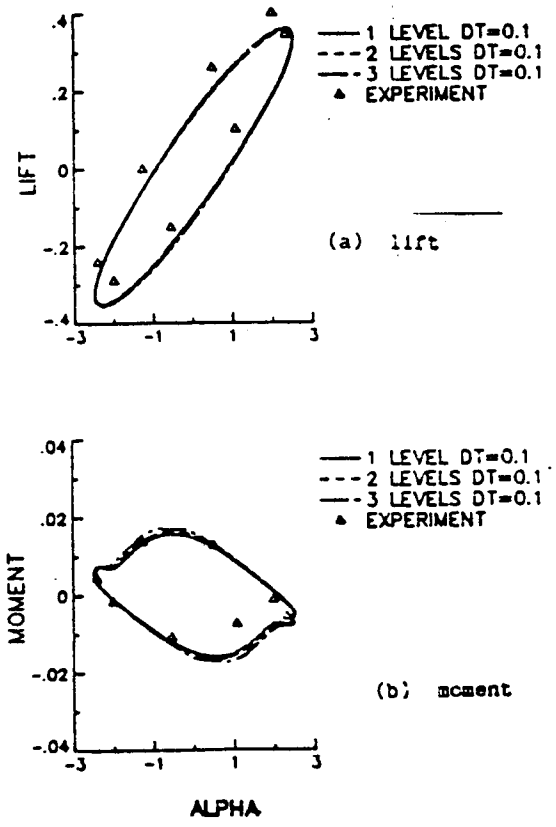

Fig. 76 Unsteady forces and moments; NACA 0012, $M_\infty = 0.755$, $k = 0.0814$, $\alpha_m = 0.016°$, $\alpha_1 = 2.51°$.
(Anderson et al., Ref. 81)

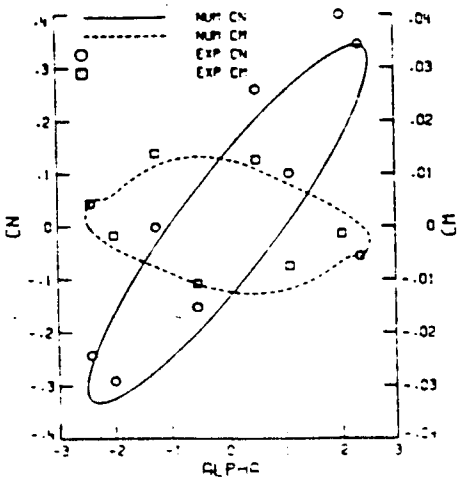

Fig. 77 Lift and pitch-moment coefficients. NACA 0012, $M_\infty = 0.755$, $\alpha_0 = 2.51°$, $k = 0.0814$, $\Delta t = 0.005$.
(Kandil and Chuang, ref. 146)

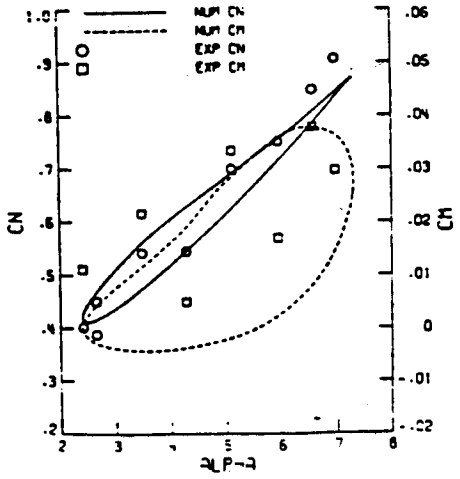

Fig. 78 Lift and pitching-moment coefficients, NACA 0012, $M_\infty = 0.6$, $\alpha_m = 4.86°$, $\alpha_o = 2.44°$, $k = 0.081$, $\Delta t = 0.01$. (Kandil and Chuang, ref. 146)

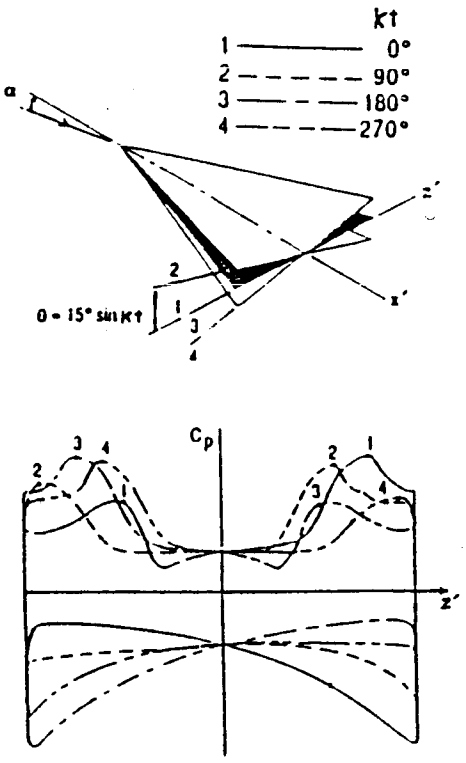

Fig. 79 Summary of surface pressure on a rolling delta wing during one cycle of periodic response for $M_\infty = 2$, $\alpha = 10°$, $\omega = 0.35$, $k = 1.337$, $\theta max = 15$ (Kandil and Chuang, ref. 146)

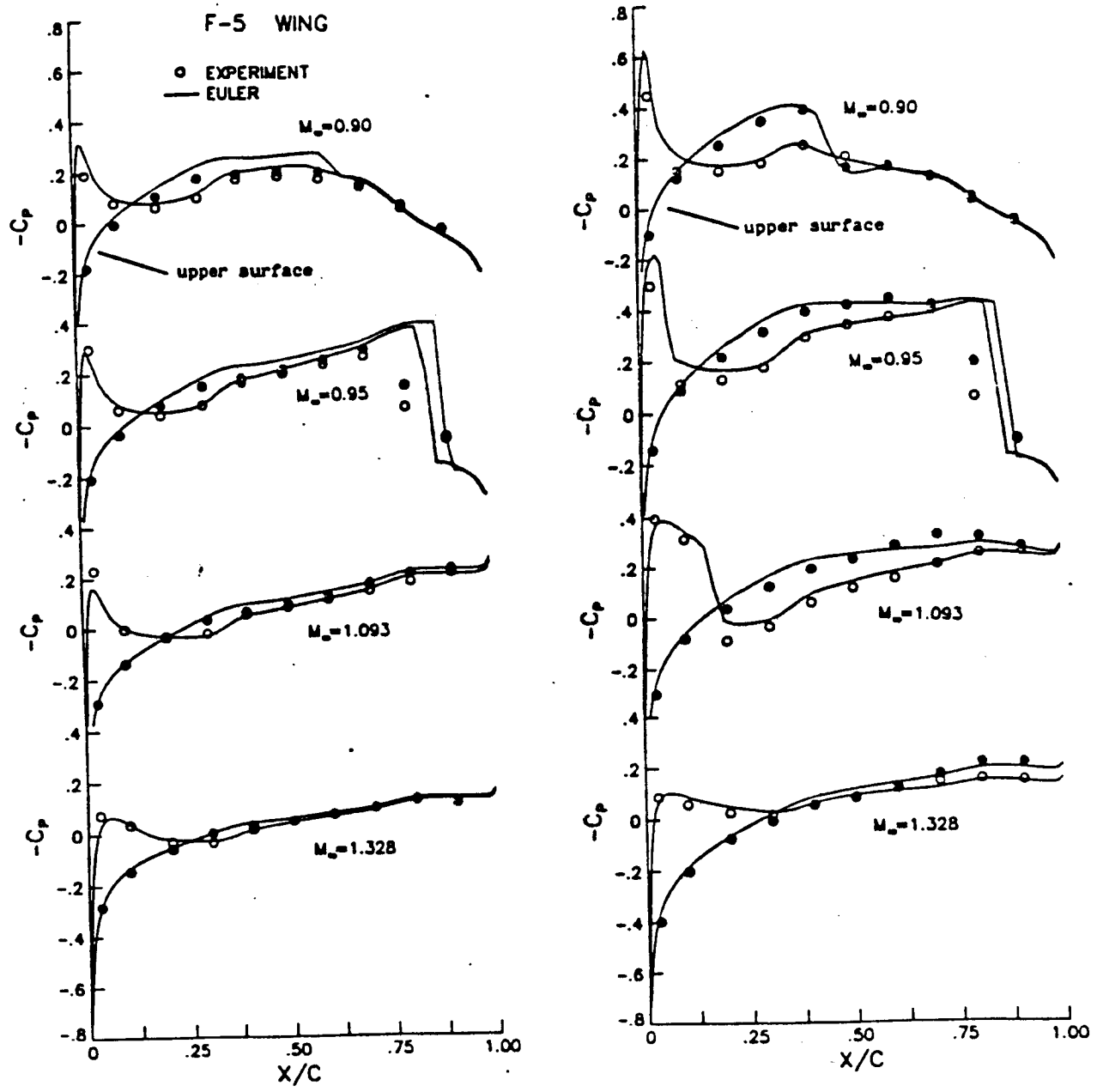

(a) y/s = 0.174

(b) y/s = 0.8412

Fig. 80 F-5 steady pressure distributions at two spanwise positions for four freestream Mach numbers and zero degrees angle of attack.
(Anderson, et al., ref. 81)

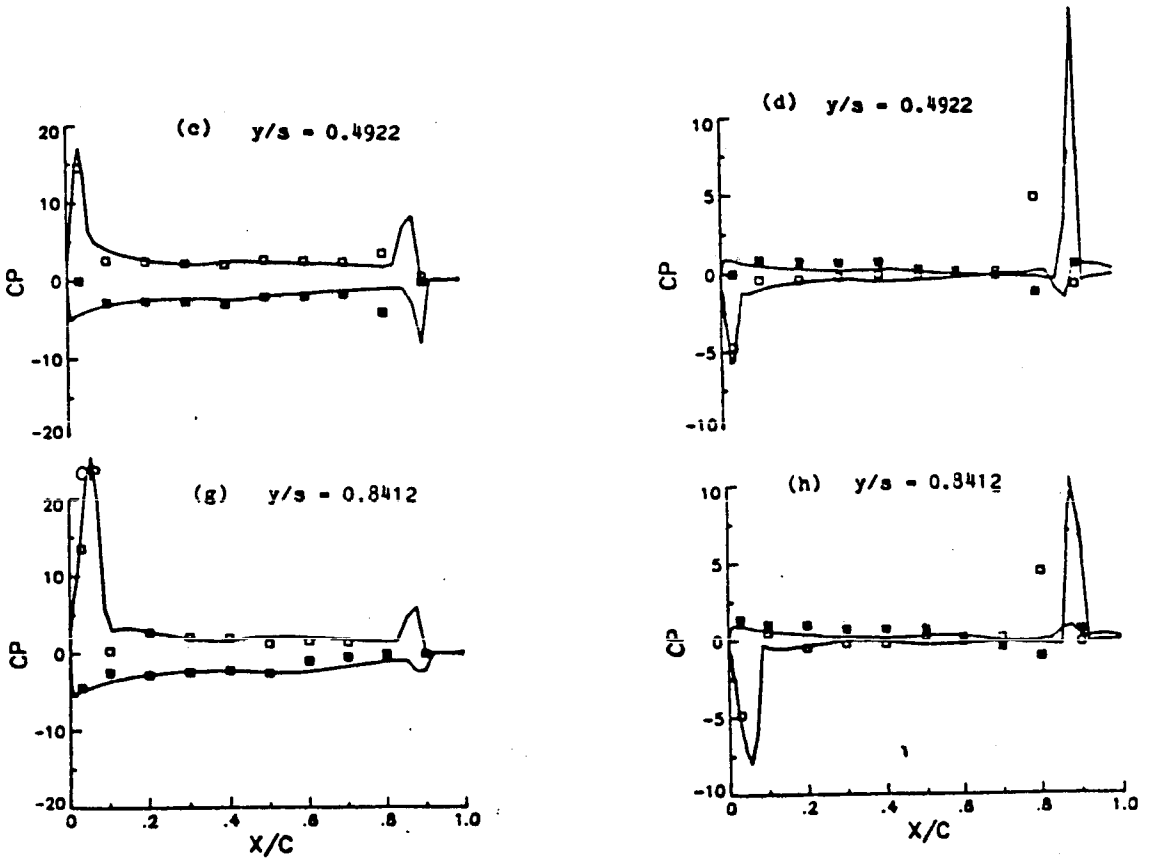

(a) M = 0.95, k = 0.264, αm = 0°, α0 = 0.532°

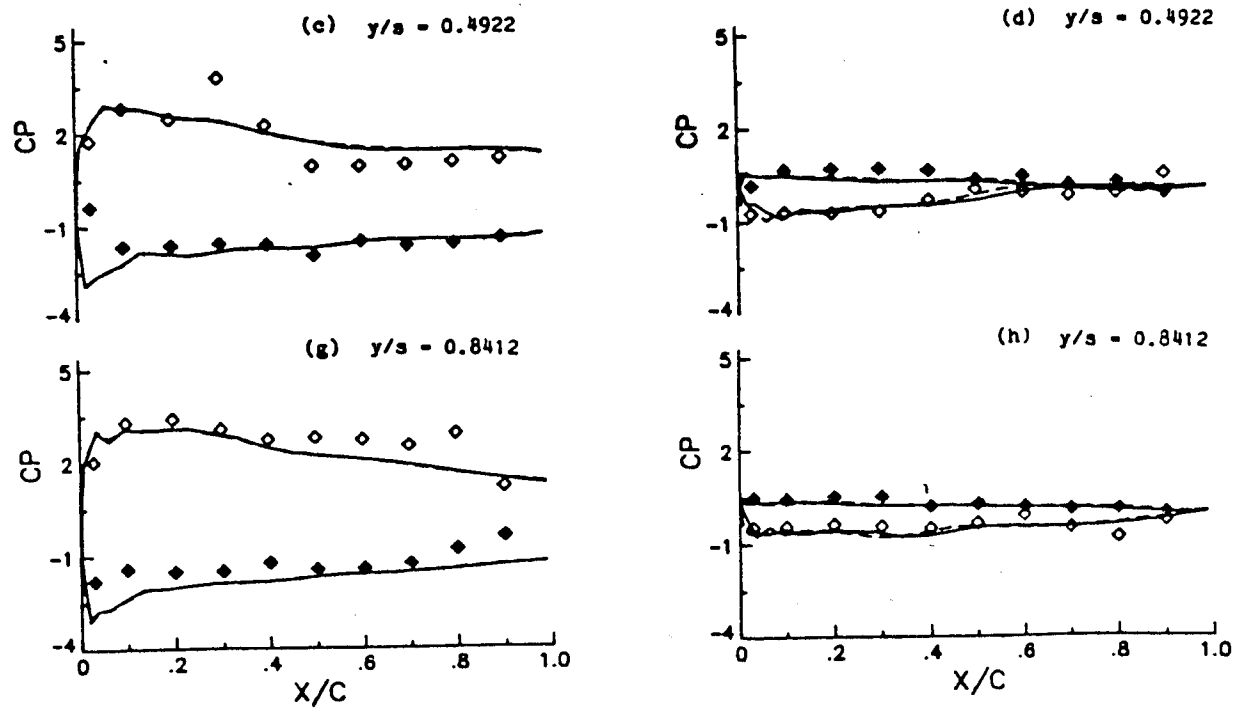

(b) M = 1.32, k = 0.396, αm = 0°, α0 = 0.222°

Fig. 81 Comparison of measured and calculated unsteady pressures on F-5 wing model. (Anderson, et al., ref. 81)

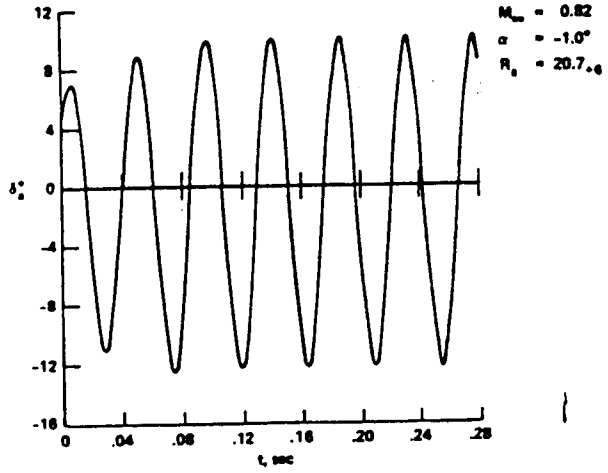

ɟ. 82 Computed variation of aileron angle with time showing buzz condition.
(Steger and Bailey, ref. 25)

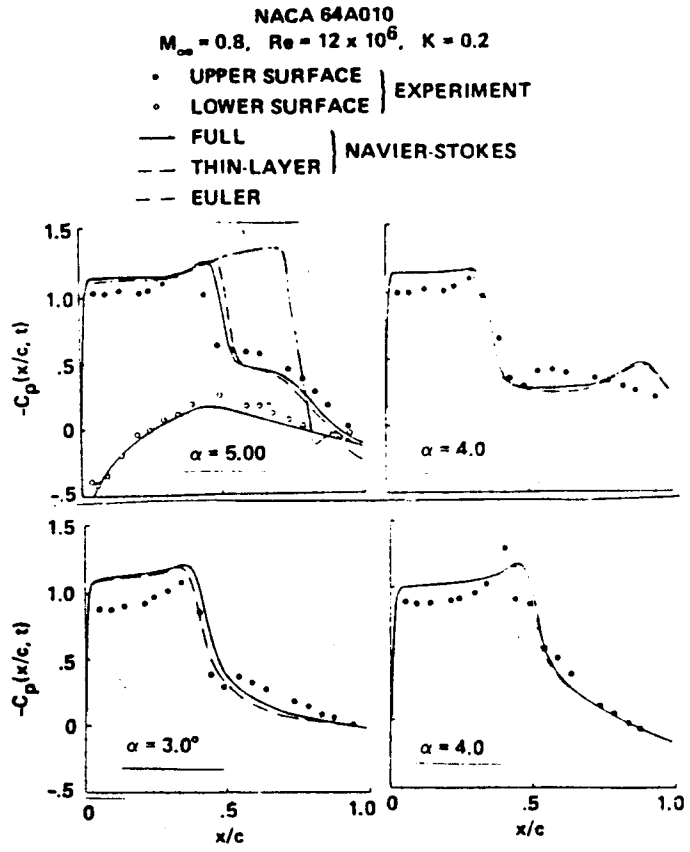

Fig. 84 Comparison of calculated and measured pressure coefficients for NACA 64A010A airfoil at shock-induced separation condition, $\alpha = 4° + 1° \cos \omega t$.
(Chyu and Davis, ref. 27)

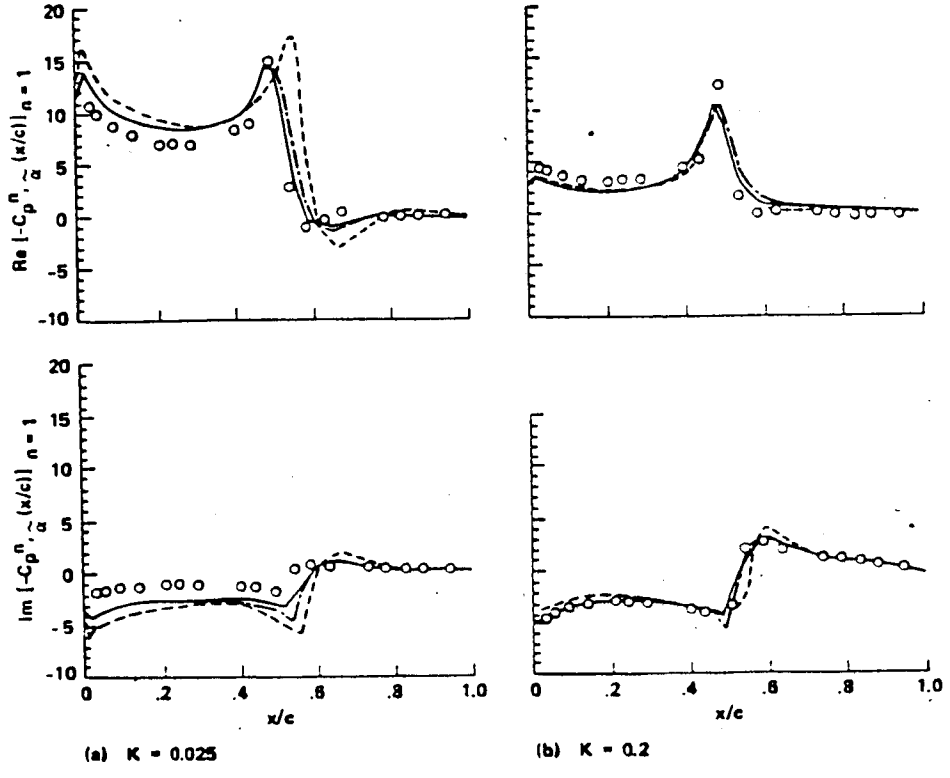

Fig. 83 Mean and first harmonic complex components of pressure coefficients: $\alpha = 0° + 1° \cos \omega t$. (Chyu and Davis, ref. 27)

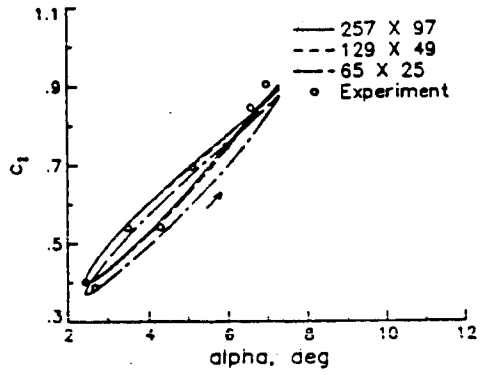

a) lift coefficients

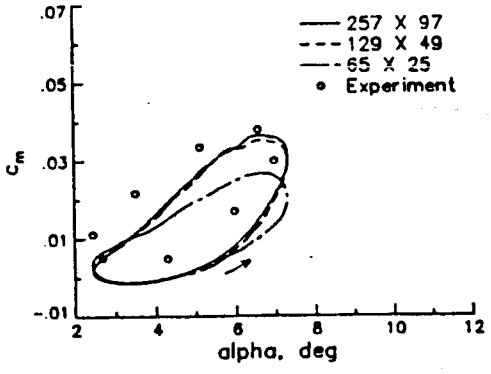

b) moment coefficient

Fig. 85 Comparison of unsteady forces versus angle of attack for the NACA 0012 airfoil at $M = 0.599$, $\alpha_m = 4.86°$, $\alpha_o = 2.44°$, $Re = 4.8 \times 10^6$. (Rumsey and Anderson, ref. 78)

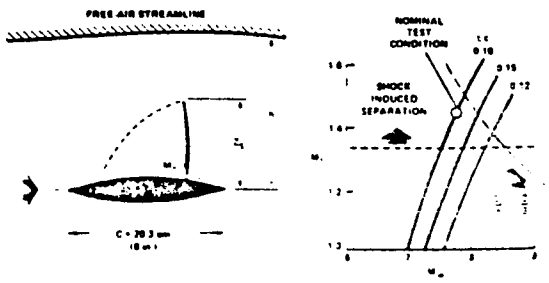

Fig. 86 Eighteen percent thick circular arc airfoil experimental conditions. (McDevitt, ref. 44)

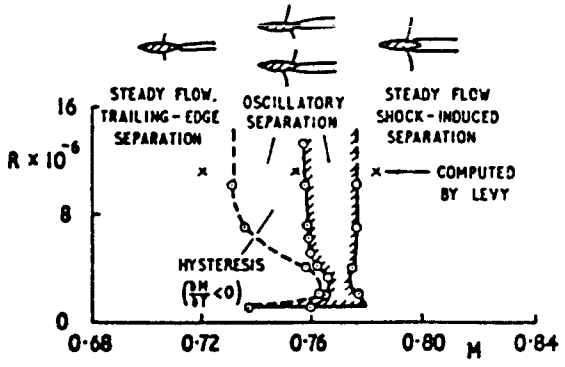

Fig. 87 Steady and oscillatory flow domains for an 18 percent thick circular arc airfoil (Levy, ref. 45)

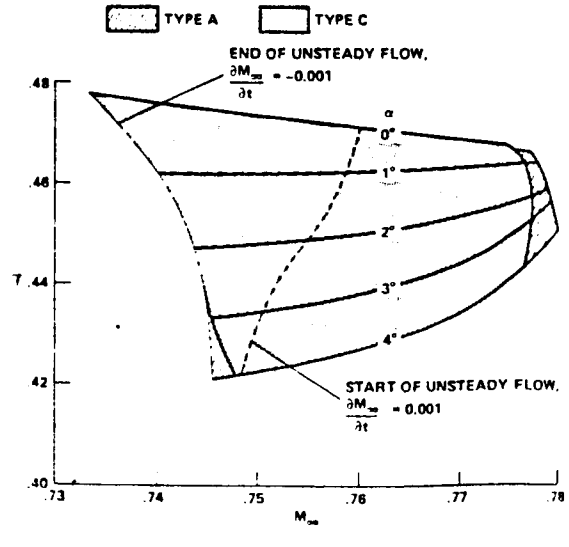

Fig. 88 Reduced frequency of periodic oscillations on an 18 percent thick circular arc airfoil for varying angle of attack. (McDevitt, ref. 44)

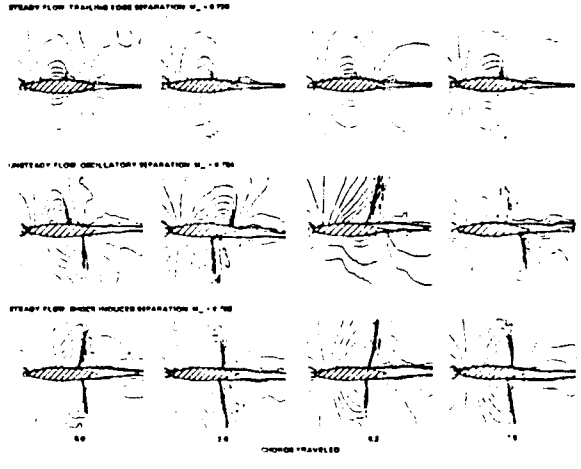

Fig. 89 Computed Mach contours for 18 percent circular arc airfoil, $M = 0.72$, 0.75, and 0.78, $Re_c = 11 \times 10^6$. (Levy, ref. 45)

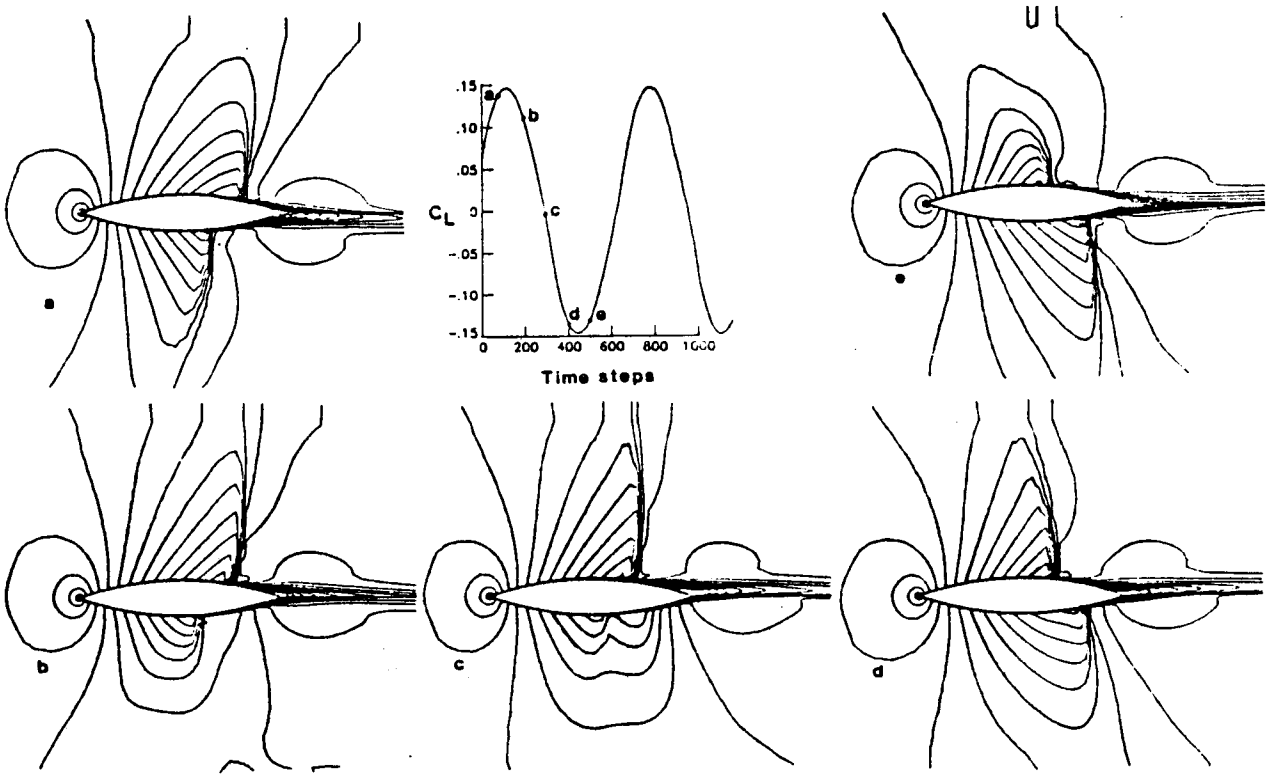

Fig. 90 Calculated periodic oscillation for 18% biconvex airfoil with implicit thin-layer Navier-Stokes code, M = 0.78, Re = 11 x 10^6, k = 0.406.
(Edwards and Thomas, ref. 1)

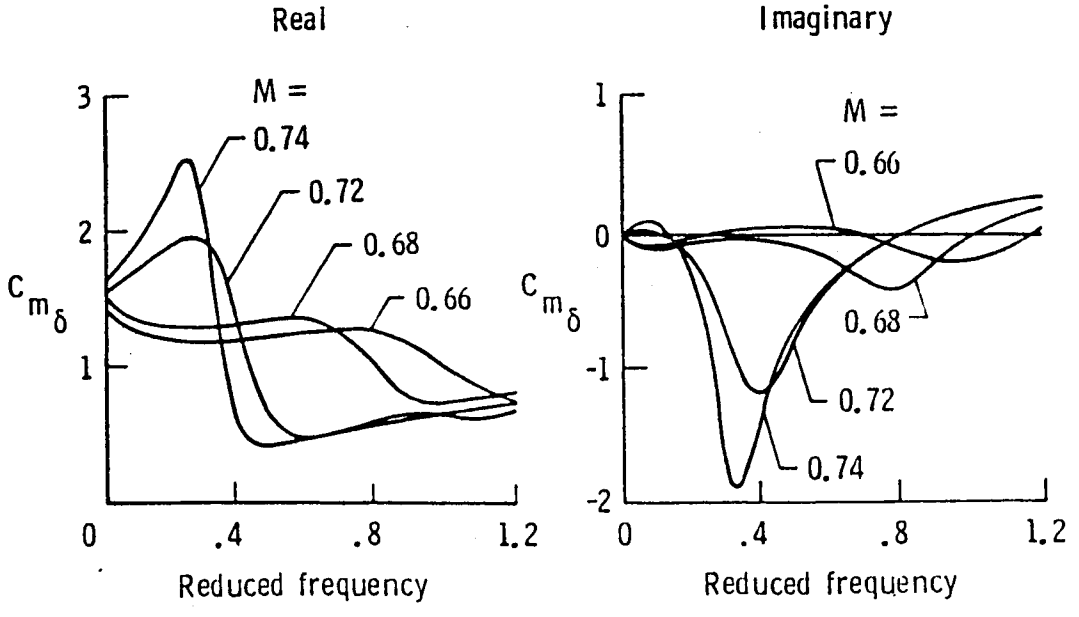

Fig. 91 Calculated pitching moment coefficient for 18% biconvex airfoil with non-isentropic TSD code.
(Edwards and Thomas, ref. 1)